Identification of thermal and mechanical parameters for Fe-15Mn-10Cr-8Ni-4Si (wt. %) ferrous based shape memory alloy

Dissertation
zur Erlangung des akademischen Grades
Doktoringenieur
(Dr.-Ing.)

von M.Sc. **Rana Atta ur Rahman**
geb. am 01 Jan. 1980 in Jhang, Punjab, Pakistan
genehmigt durch die Fakultät für Maschinenbau
der Otto-von-Guericke-Universität Magdeburg

Gutachter:
Prof. Dr.-Ing. Daniel Juhre
Prof. Dr.-Ing. habil Thorsten Halle

Einreichung der Doktorarbeit am: January 05, 2021
Promotionskolloquium am: November 09, 2022

Abstract

The materials comprising of more than one phases have very special applications where other materials cannot work. Well-known shape memory alloys (SMAs) might be replaced by ferrous based shape memory alloys (Fe-SMAs) since the research has unfolded their outstanding features like low cost, high cold workability, and good weldability. The Fe-15Mn-10Cr-8Ni-4Si (wt. %) Fe-SMA has been used in this thesis and found to be effective because Fe-SMAs have great potential to be the counterpart of Nitinol. Numerous researches have been performed on Fe-SMAs during last decade. Several studies have been made on the mechanical properties of Fe-SMAs. There are several researches available showing different mechanical applications which exist currently. Interest in Fe-SMAs is still acute, due to continuing research on their applications in different fields. They can efficiently be used for several other applications too because their applications and features are not fully discovered, therefore, further research must be done to unfold its advantages and usage. For the future applications, not only mechanical behavior of Fe-SMAs but also the comprehensive view of thermomechanical behavior is important because the phase transformation (austenite ↔ martensite) is also attributed to changes in temperature. It is also required for future thermomechanical modeling of Fe-SMAs.

To the author's knowledge, such a thermomechanical behavior of the valuable Fe-15Mn-10Cr-8Ni-4Si SMA has not been investigated so far to explore its thermomechanical applications, therefore, it has been done in this thesis through experimentation. Besides, a number of significant mechanical investigations are also performed which have not been explored so far.

Zusammenfassung

Materialien, die aus mehr als einer Phase bestehen, haben spezielle Anwendungsfelder, in denen andere Materialien versagen. Heutzutage können altbekannte Formgedächtnislegierungen (FGL, englisch SMAs) durch eisenbasierte Formgedächtnislegierungen (Fe-SMAs) ersetzt werden, da die Forschung deren herausragende Eigenschaften wie niedrige Kosten, hohe Kaltumformbarkeit und gute Schweißbarkeit aufgezeigt hat. Die Fe-SMA mit der Bezeichnung Fe-15Mn-10Cr-8Ni-4Si (Gew. %) wurde für diese Thesis ausgewählt, da die eisenbasierten Formgedächtnislegierungen großes Potenzial haben, das Gegenstück zu Nitinol zu bilden. Auch wenn bzgl. der mechanischen Eigenschaften und möglichen Anwendungsgebiete der Fe-SMAs im vergangenen Jahrzehnt bereits ein hohes Maß an Forschung betrieben wurde, ist das wissenschaftliche Interesse weiterhin aktuell, da stets die Anwendbarkeit in verschiedenen Bereichen untersucht wird. Es muss weiter geforscht werden, da die möglichen Anwendungen und Eigenschaften noch nicht vollständig aufgedeckt wurden. Für die Zukunft geht das Interesse über das mechanische Verhalten der Fe-SMAs hinaus und bezieht das thermomechanische Verhalten ein. Dieses ist wichtig. da die Phasentransformation (Austenit ↔ Martensit) schließlich mit Temperaturänderung in Verbindung gebracht wird. Ebenfalls hat es Relevanz für die thermomechanische Modellierung der Fe-SMAs.

Nach dem besten Wissen des Authors wurde das thermomechanische Verhalten von Fe-15Mn-10Cr-8Ni-4Si noch nicht weit genug für die thermomechanischen Anwendungen untersucht, weshalb dies in der vorliegenden Arbeit unter der Nutzung von Experimenten umgesetzt wird. Darüber hinaus werden signifikante mechanische Untersuchungen durchgeführt, die bisher in dieser Form nicht getätigt wurden.

Declaration of honor

I hereby declare that I produced this thesis without prohibited external assistance and that none other than the listed references and tools have been used. I did not make use of any commercial consultant concerning graduation. A third party did not receive any nonmonetary perquisites neither directly nor indirectly for activities which relate to the contents of the presented thesis.

All sources of information are clearly marked, including my own publications.

Particularly, I have not consciously:

- Fabricated data or rejected undesired results
- Misused statistical methods with the aim of drawing other conclusions than those warranted by the available data
- Plagiarized data or publications
- Presented the results of other researchers in a distorted way

I know that violations of copyright may lead to injunction and damage claims of the author and also to prosecution by the law enforcement authorities. I hereby agree that the thesis may need to be reviewed with an electronic data processing for plagiarism.

This work has not yet been submitted as a doctoral thesis in the same or a similar form in Germany or in any other country. It has not yet been published as a whole.

Magdeburg, 09 Nov. 2022

…………………………………
Rana Atta ur Rahman

Table of symbols

Abbreviations

σ	Stress
γ	Austenite phase
ε	Martensitic phase
λ	Thermal conductivity
λ (T)	Dependence of thermal conductivity on temperature
ΔH	Enthalpy of transition
α	Thermal diffusivity
α (T)	Dependence of thermal diffusivity on temperature
ρ	Density
ρ (T)	Dependence of density on temperature
ε_{rec}	Recovery strain
η	Shape recovery ratio
λ	Wavelength
θ	Diffraction angle
ε_{tr}	Transformation strain
A_s	Austenite start temperature
A_f	Austenite finish temperature
ASTM	American society for testing and materials
BL	Baseline
BCC	Body centered cubic
Cu-SMAs	Copper based shape memory alloys
LCF	Low cycle fatigue
Cr	Chromium
Cu	Copper
CBN	Cubic boron nitride

CFRP	Carbon fiber reinforced polymer
C_P	Specific heat capacity
C_P (T)	Dependence of specific heat on temperature
CTE	Coefficient of thermal expansion
DSC	Differential scanning calorimetry
DIN	Deutsches Institut für Normung
d	Density
d_{hkl}	Inter-planar spacing of the hkl planes in the crystal lattice
d	Distance of lattice planes
EB	Electron beam welding
ESEM	Environmental scanning electron microscope
EDS	Energy dispersive spectroscopy
Fe	Ferrous
Fe-SMAs	Ferrous based shape memory alloys
FeMnSi-SMAs	Ferrous-manganese-silicon based shape memory alloys
FSMAs	Ferromagnetic shape memory alloys
FMSM	Ferromagnetic shape memory
FCC	Face-centered cubic
FRP	Fibre-reinforced polymer
HCP	Hexagonal closed pack
HTSMAs	High temperature shape memory alloys
Iron-SMAs	Iron-based shape memory alloys
ISO	International organization for standardization
LFA	Laser flash analysis
LB	Laser beam welding
M_s	Martensite start temperature
M_f	Martensite finish temperature
Mn	Manganese
MFIS	Magnetic field induced strain
MP	Melting point
m	Mass
Ni	Nickel
NiTi	Nickel Titanium
Ni-SMAs	Nickel-based shape memory alloys
SMA-NRBs	Shape memory alloy based natural rubber bearings

NSM	Near surface mounted
N_f	Number of cycles to fatigue failure
NIST	National institute of standards
n	Order of diffraction
OWSMA	One-way shape memory alloys
PCMs	Phase changing materials
PE	Pseudoelastic effect
Pt	Platinum
R-phase	Rhombohedral phase
RT	Room temperature
RC	Reinforced concrete
Rh	Rhodium
SMA	Shape memory alloy
SME	Shape memory effect
SMMs	Shape memory materials
Si	Silicon
SEM	Scanning electron microscopy
SMAs	Shape memory alloys
SEM-EDS	Scanning electron microscopy-energy dispersive spectroscopy
OWSME	One-way shape memory effect
TWSME	Two-way shape memory effect
T	Temperature
TIG	Tungsten inert gas
TM	Temperature modulated
v	Volume
XRD	X-rays diffraction
Zr	Zirconium

Contents

Chapter 1

Introduction

1.1 Motivation

Shape memory alloys (SMAs) have made the material engineering science technologically advanced, they exist mainly as Nitinol (Nickel Titanium, NiTi), ferrous based shape memory alloys (Fe-SMAs or Iron-SMAs) and copper based shape memory alloys (Cu-SMAs). SMAs have revolutionized the material engineering science as they exhibit exclusive features like shape memory effect and superelasticity (pseudoelasticity), which are based on the so-called martensitic phase transformation. There are several applications of both effects of SMAs as described in chapter 2. SMAs are used to generate forces (due to shape memory effect) or to store energy (due to pseudoelasticity). SMAs belong to a class of shape memory materials (SMMs), which have ability to memorize their previous form when subject to any stimulus e.g. magnetic, mechanical, or thermal variations. In most of the engineering applications, structures and components experience such type of variations. SMAs have two main phases, (i) the high temperature phase called as austenite, and (ii) the low temperature phase called as martensite. The phase transformation occurs either mechanically or thermally. SMAs have also the advantages like high strength, and wear resistance. The main reason for the extraordinary behavior of SMA is the martensitic phase transformation. The SMAs are also classified as smart materials.

Nitinol is the most eminent amongst all. Nitinol has always been the most commercial alloy due to its biocompatibility, resistance to corrosion, good cyclic stabilisation, and the capacity to recover large deformations. Nitinol has also some disadvantages like sensitivity of material properties in fabrication and it is expensive as well. The high cost of Nitinol is a main limiting factor for its wider use in industry.

Copper based shape memory alloys (Cu-SMAs) have shown the potential to be used as SMAs due to their good shape recovery, excellent conductivity of heat and electricity, and ease of fabrication. However, the applications of Cu-SMAs are still limited due to shortcomings of thermal stability, brittleness, and mechanical strength which are closely related to microstructural characteristic of Cu-SMAs like high elastic anisotropies, coarse grain sizes, and congregation of secondary phases or impurities along the grain boundaries. The researchers are doing the efforts to overcome these drawbacks by, (i) proper ternary additions, (ii) adopting alternative routes, and (iii) optimizing the heat treatment cycles.

This thesis is related to Fe-SMAs or more specifically FeMnSiX-SMAs (X shows other elements) because Fe-SMAs are not as expensive as Nitinol. Fe-SMAs are easy to be produced as compared to Nitinol. Fe-SMAs are also found to be effective due to their high cold workability, and good weldability as compared to that of Nitinol which has low cold workability and high processing cost. Czaderski et al. and Huang et al. [1][2] showed that FeMnSi-SMAs have a great potential for civil engineering structures because of its unique properties e.g. one-way shape memory effect (OWSME), two-way shape memory effect (TWSME) because they remember both high and low-temperature shapes, superelasticity, high elastic stiffness and a wider transformation hysteresis compared to that of Nitinol [1][2]. Fe-SMAs also overcome the drawbacks of Cu-SMAs like brittleness and low mechanical strength. The capability of Fe-SMAs to allow the development of smart structures with active control of strength, stiffness, ability of self-healing, and self-repairing opens the door for exciting opportunities, making them the construction material of the future. The other reasons of selecting Fe-SMA in this thesis are mentioned below as well as in section 3.1.

The importance of Fe-SMAs in terms of their drastically increasing rate of research in different fields during the last decades has been described as shown in Fig. 1.1. The researchers are mainly interested in FeMnSi-SMAs amongst several other types of Fe-SMAs [3].

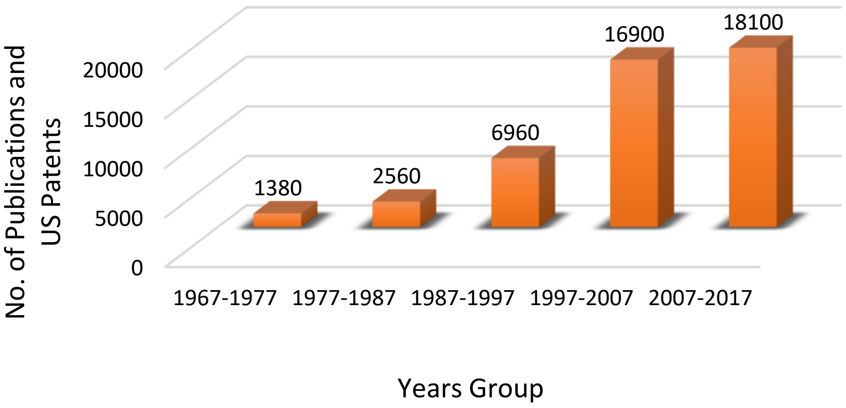

Fig. 1.1: Increasing rate of research on Fe-SMAs [3]

Furthermore, it has been perceived by Sawaguchi et al. that the unique property of remarkable fatigue life makes FeMnSi-SMAs suitable for seismic damping applications for construction buildings. FeMnSi-SMA when used as a damper can also absorb the vibrations due to stable damping capacity associated with reversible martensitic transformations under cyclic push-pull loading [4]. Contrary to other elastic-plastic materials, SMAs have the ability to put up applied stresses via material phase change [5]. Due to increased earthquakes in Japan nowadays, seismic vibration control buildings and structures have been built in order to minimize the catastrophic effects of the earthquake. For that purpose, Fe-SMA has been used in the structures for damping of the vibrations. Fe-15Mn-10Cr-8Ni-4Si damping alloy invented in 2015 with superior low cycle fatigue (LCF) life of 8000 cycles at a total strain range of 2.0% (total strain amplitude of $1x10^{-2}$); has been successfully installed in a 40-storey skyscraper [4][6]. This seismic damper of Fe-15Mn-10Cr-8Ni-4Si (wt. %) Fe-SMA is shown in Fig. 1.2a. The plate of this alloy used in seismic dampers is shown in Fig. 1.2b [7]. The most important thermal and mechanical parameters of Fe-15Mn-10Cr-8Ni-4Si (wt. %) Fe-SMA have been investigated in this thesis; as described in chapter 3.

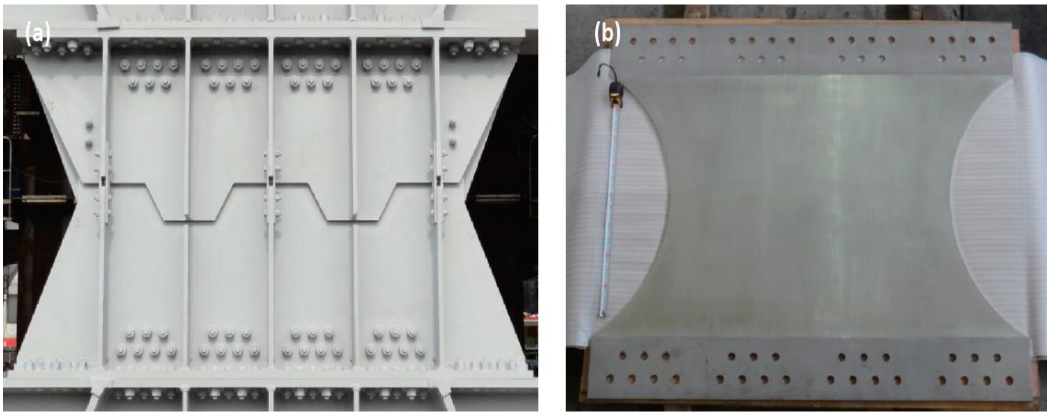

Fig. 1.2: (a) The front view of shear panel type seismic damper comprising of the springs and dampers inside, and (b) the Fe-15Mn-10Cr-8Ni-4Si SMA plate used in seismic dampers, therefore, they can bear 4,000 kN load and buckling can be avoided [7]

The amount of different components in the alloy have been attuned in order to meet the required characteristics. To enable the production of large-scale products using an electric furnace, the concentration of Manganese (Mn) has been reduced to 15 wt. % [8]. To stabilize the austenite against α-ferrite and to restrict the progress of α′-martensite upon loading, the amount of Nickel (Ni) has been increased to 8 wt. % [9]. It has been observed that adding the considerable amount of Cr to FeMnSi-SMA generates its ability to corrosion resistance but there is a restriction associated with Cr that if it is added more than 7% (i.e. 10%) then corrosion resistance is affected which can be restored by alternatively adding Ni as discussed earlier [10]–[13]. Poor corrosion resistance is the main limiting factor for the use of FeMnSi-SMAs in engineering applications, therefore, much attention has been given to improve corrosion resistance through suitable alloy addition. It has been observed that more than 2 wt.% Si (Si > 2 wt.%) has a beneficial effect of decreasing the corrosion rate [14]–[16]. It is noteworthy that the highest N_f (number of cycles to fatigue failure) is generally obtained at 4 wt.% concentration of Si, which is coupled to an optimal degree of reversibility of the dislocation motion [9].

Fig. 1.3 shows the development in applications of Fe-SMAs during last three decades. The considerable percentage increase in their applications has been clearly observed by a detailed review of all the existing applications of Fe-SMAs [17].

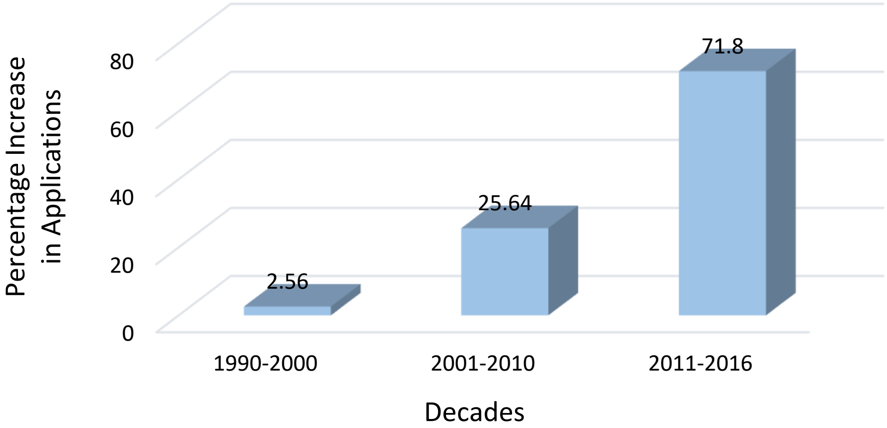

Fig. 1.3: Percentage increase in applications of Fe-SMA [17]

It has been observed by the detailed literature review that many applications of Fe-SMAs have been discovered so far in different fields of research. Interest in Fe-SMAs is still important because many applications and inventions are yet to be explored more in different fields due to their remarkable properties. For the applications in future, a detailed view of thermomechanical behavior is also important along with other properties of Fe-SMAs. It has been observed that some very significant thermal parameters for thermomechanical applications as well as some crucial mechanical parameters through uniaxial compression and biaxial compression (detail discussion in chapter 3) for Fe-15Mn-10Cr-8Ni-4Si SMA have not been explored so far.

The chapter 1 focuses on a brief and general description of SMAs. After a short overview of the advantages and disadvantages of general SMAs, Nitinol, Cu-SMAs, and Fe-SMAs; chapter 1 also elaborates the importance, motivation and priority of the research required on Fe-SMA. The chapter 1 closes with a structural overview of the following chapters. The chapter 2 comprises of the existing types and applications of Fe-SMAs as well as the literature required to perform the successful experimentations. The aim and focus of the present thesis have been described in chapter 3. The experimental procedures have been explained in chapter 4 whereas the obtained results and discussions have been performed in chapter 5. In general, the discussions point out the most critical aspects in terms of the interpretation of the presented experiments. The comparative study of the obtained results has been performed only with Nitinol (typically composed of approximately 55 wt. % Nickel and 45 wt. % Titanium), stainless steel, 60-Nitinol (typically composed of approximately 60 wt. % Nickel and 40 wt. % Titanium) and two different copper-based shape memory alloys (Cu-SMAs) due to unavailability of the literature related to that of Fe-SMAs. The comparison with previous work has been done by earlier researchers where required and it is shown that the present findings are in good agreement with the respective literature. Using experimental results to reproduce the experimental curves by means of numerical computations is a part of future work because the results are also useful for future mechanical as well as thermomechanical modeling of Fe-SMAs. Finally, the most important conclusions and some interesting prospects for future work are summarized in chapter 6. The research has been performed at Otto von Guericke University (OvGU) Magdeburg, Germany.

Chapter 2

Literature Review

In this chapter, an extensive literature review of the research on Fe-SMAs has been performed. The pre-existing applications of Fe-SMAs have been discussed in detail. A part of the literature study has also been stated in the respective chapters.

2.1 Types of Fe-SMAs

It has been observed that there are many types of Fe-SMAs which have been categorized as; (1) FeMnSi based shape memory alloys, (2) ferromagnetic shape memory alloys, and (3) FeMnAl based shape memory alloys. FeMnSi-SMAs is the most renowned type because the researchers are typically interested in this type due to their better properties as shown in Fig. 2.1 [3]. Unlike FeMnSi-SMAs, ferromagnetic shape memory alloys especially FeNiCo shape memory alloys are magnetic shape memory (MSM) materials which are operated in martensite phase when microstructure is twinned, and deformation takes place by twin boundary motion. The twin structure can be associated with magnetic domain structure because MSM materials are ferromagnetic if the material has high magneto-crystalline anisotropy. That's why, the applied magnetic field can influence the twin structure and cause deformation by twin boundary motion [18]. Therefore, the research is being done to develop the knowledge to raise the martensite temperature of the FeNiCo system in order to achieve the shape memory at room temperature [19]. Contrary to FeMnSi-SMAs, the shape memory effect of FeMnAl-SMAs is only reported by Ishida et al. [20][21] in his patent. Vollmer et al. recently observed that rapid quenching of polycrystalline FeMnAl based alloy in cold water results in crack formation mainly at grain boundaries of α phase, furthermore, cooling rate is slowed down when crack formation is suppressed by means of solution treatment [21][22].

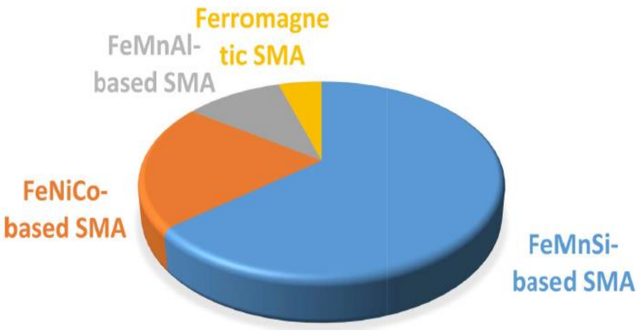

Fig. 2.1: Different types of Fe-SMAs [3]

2.2 Applications of ferrous based shape memory alloys

Nitinol has wide-ranging applications in many fields [23], however, the applications of Fe-SMAs are drastically increasing at present times [24][25]. The detailed review of pre-existing applications of Fe-SMAs has been performed and it has been clearly observed that there is a considerable percentage increase in the applications of Fe-SMAs during the preceding years. The following pre-existing applications of Fe-SMAs have been found from literature study.

Fe-SMAs are the most promising candidates for fast development in the construction industry as well as for repairing civil structures when using these SMAs as pre-stressing tendons. Until now their applications are not completely discovered [10][11]. They are being utilized for the strengthening of concrete beams using near surface mounted (NSM) method. Wearing and tearing of concrete bridges can be avoided using Fe-SMAs strips. Fe-SMAs are suitable as strips because they are very ductile prior to failure [26][27]. The possibility of using Fe-SMA strips is discussed instead of using; (i) fibre-reinforced polymer (FRP) strips because Fe-SMA strips result in the recovery stress ranging from 250 to 300MPa, and (ii) carbon fiber reinforced polymer (CFRP) strips because their bond shear stress with epoxy came out to be 14MPa while it is observed to be 4MPa in case of ribbed Fe-SMA with mortar. Mortar is a paste used to bind bricks, stones and building blocks [1][28]. Recently developed Fe-SMA with the composition of Fe-17Mn-5Si-10Cr-4Ni-1VC (mass %) shows encouraging properties with respect to potential for shotcrete layer to strengthen reinforced concrete (RC) structure [29]. This technique of shotcrete is used to construct and repair the structures [10], swimming pools [30], mine support [31], building columns, building beams [32], retaining walls, foundations [33][34], refractory [35], artificial rock [36]. The behavior of the properties of two different smart elastomeric bearings composed of SMA wire have been illuminated as shown in Fig. 2.2. Based on different parameters such as variety of SMA, shear strain amplitude, base isolator aspect ratio, SMA wire thickness and the quantity of pre-strain existence in wires for shape memory alloy based natural rubber bearings (SMA-NRBs) performance; have been examined. Fe-Ni-Cu-Al-Ta-B SMA with 13.5% superelastic strain and a very low austenite finish temperature (-62^{o}C) has been proposed as the best material to be used in SMA-NRBs, exposed to high shear strain amplitudes. One of the well-known seismic control methods being used in bridges, buildings, and other civil structures is seismic base isolation. Different types of base isolators such as lead rubber bearings, high-damping rubber bearings, friction pendulum bearings, and steel plate dampers etc. are being used all around the world depending upon their practice and needs. The main reason for the use of base isolators is their high flexibility, which results in the change of natural period to a safer value far away from the critical period range of an earthquake. It has been indicated that the seismic response of bridges to an earthquake can be considerably controlled using elastomers isolators wrapped in SMA wires. An isolator composed of eight SMA coil springs has been recommended. It has been assumed that these SMA coil springs can be used with rubber bearings or friction pendulum systems permitted to control the vertical and horizontal impacts on civil structures [37]–[39].

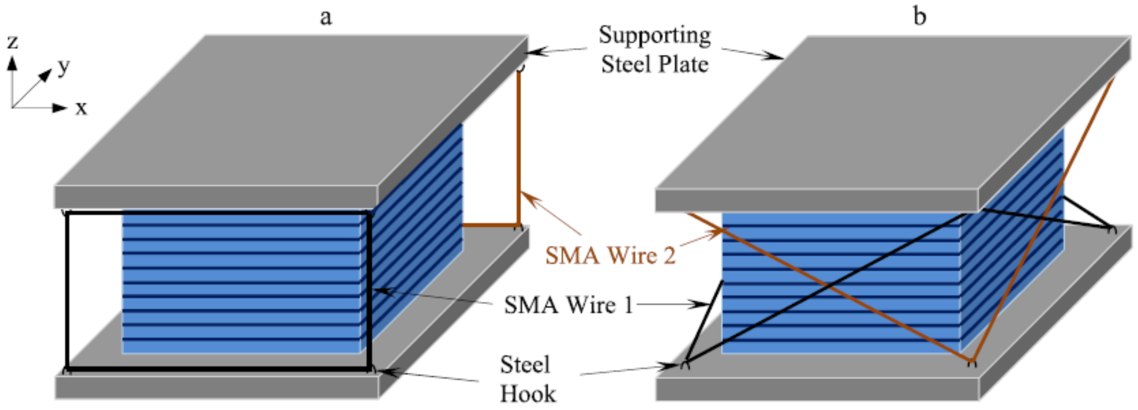

Fig. 2.2: Smart Rubber Bearings (a) straight SMA wires (b) cross SMA wires [37]–[39]

Fe-30Mn-6Si-4Cr-5Ni stainless SMA is used to make Fe-SMA nuts. By using such type of nut; (1) self-locking frictional moment is considerably increased, (2) axial load uniformity among different screw teeth is improved, (3) failure phenomena is reduced, (4) thread connection loosening is prevented, (5) disengaging is controlled, and (6) thread fatigue fracture is prevented [40]. SMA stone breakers based on Fe-SMA have their example applications such as stone exploitation, pre-splitting blasting, and demolition blasting. The devices like rock splitter are based on high force and high temperature shape memory alloys (HTSMAs). They need the material which can generate extremely large force by thermal input [41]. Fig. 2.3 shows the mechanism for Fe-SMA wires with cross-sectional area of 19.6mm^2 which are passed through the hole located in the bolt in order to avoid sliding. The wire is wrapped around this bolt which results in pre-strain of SMA wire (2%). The advantage of the suggested mechanism is its high accuracy in adjusting the level of pre-strain by accurately tightening the bolt [38].

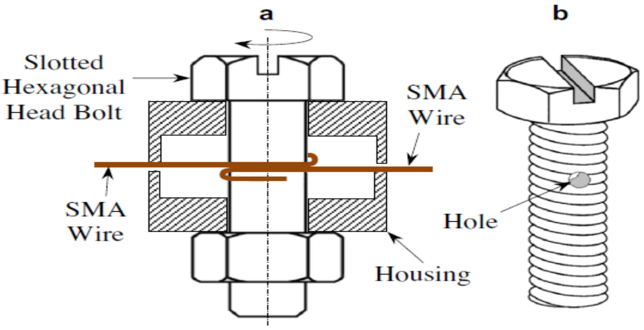

Fig. 2.3: Pre-strain Fe-SMA wires [38]

Coupling for shafts as shown in Fig. 2.4 is one of the inspiring applications because couplings of Fe-15Mn-5Si-9Cr-5Ni SMA are found to recover 83% of their diametrical expansion. Hence, suitable for a large number of industrial applications [42][43][44].

Fig. 2.4: Finished prototype Fe-SMA coupling [42][43]

In 2003, pipe joints made of Fe-28Mn-6Si-5Cr SMA as shown in Fig. 2.5 have been employed in the construction of the Wakunami tunnel in Kanazawa, Japan. The pipes were short-curved pipes having several meters length with an external diameter of about 300mm. The pipe joints made of Fe-SMA were found to be outstanding for efficiently connecting to these curved pipes [7].

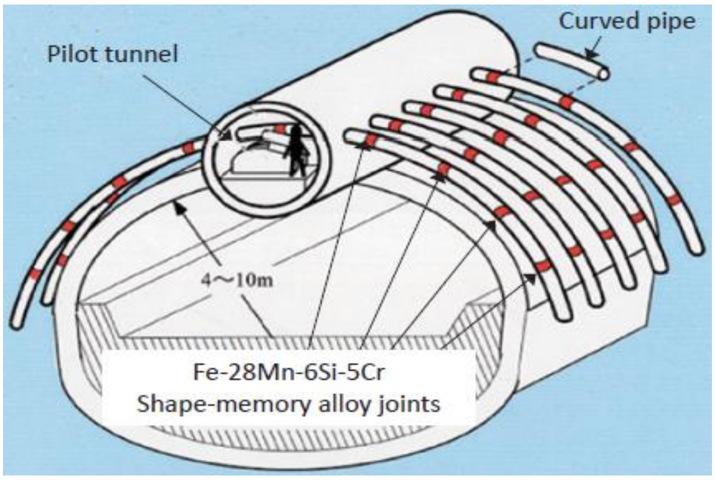

Fig. 2.5: Pipe joints of Fe-SMA [7]

Unique properties of ferromagnetic shape memory alloys (FSMAs) such as magnetic field induced strain (MFIS) and quick response make them useful for diverse applications e.g. sensors and actuators. Furthermore, in order to get excessive MFIS, some specific magnetic and micromechanical requirements must be met. Currently, several types of alloys are found to exhibit a magnetically-induced shape memory effect including NiMnGa, NiFeGa, FePd, FePt [45][46].

The literature manifests the benefits of ferrous (Fe) based alloys over magnesium (Mg) based alloys as stent material, because of their ductility and strength. Pure Fe and Fe based alloys e.g. Fe-21Mn-0.7C-1Pd have been suggested as manufacturing materials for ferrous based alloy's stent applications due to superelasticity as shown in Fig. 2.6. Owing to the already existence of Si in the human body, ferrous based alloy (Fe-30Mn-6Si) has been established due to its compatibility with the human body [47][48].

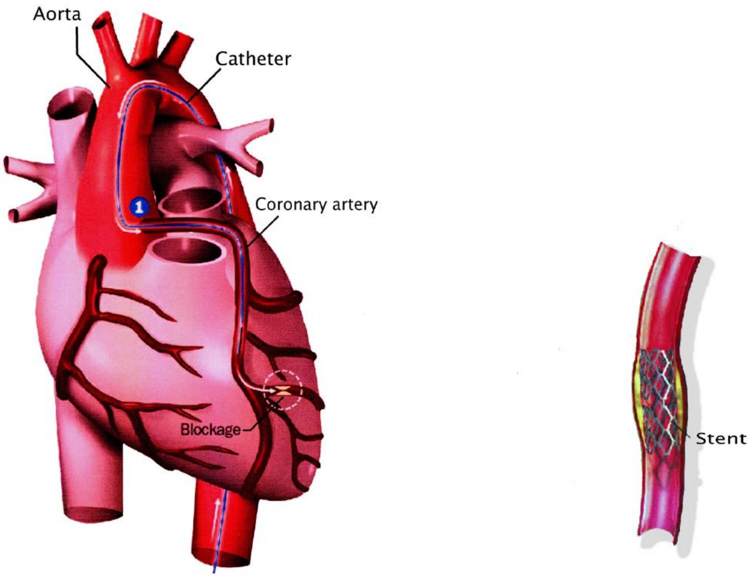

Fig. 2.6: Cardiovascular Stent of Fe-SMA [47]

SMAs are also classified into ferromagnetic shape memory alloys (FSMAs) which exhibit remarkable properties such as magnetically switchable strains of several percents at a constant temperature. Besides, they also show superelasticity in addition to ferromagnetic shape memory (FMSM); that make them appropriate for medical applications. Fe-Pd has been a promising candidate for new types of biomedical devices. Several biomedical devices such as actuators, valves, stents, bone prostheses, and matrices for tissue engineering use Fe-Pd SMA because of its biocompatibility with different cell types [49].

A bridge girder is reinforced by inserting Fe-Mn-Si-Cr SMA rods of 10.4mm diameter which cross through the cracks and strengthens the girder as shown in Fig. 2.7. The property of shape memory effect was used in this application. The rods were heated by electric power, thus, crack width reduces by 40% [50].

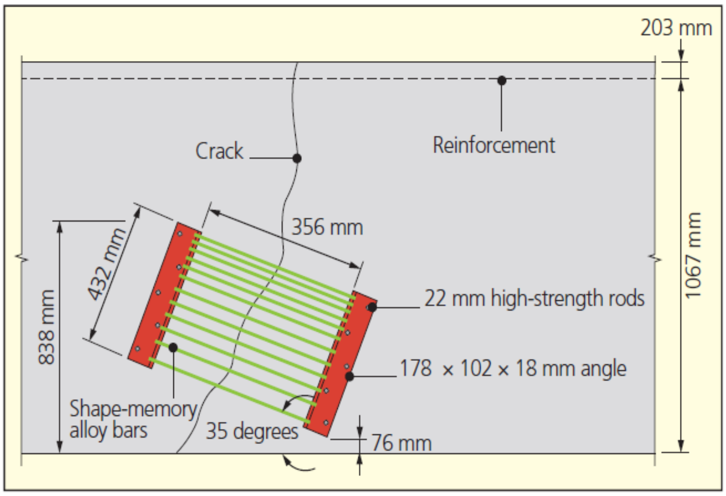

Fig. 2.7: Fe-SMA rods crossing the cracks [50]

It has been observed that the features like shape memory behavior, critical stress and proof stress for Fe-14Mn-3Si-10Cr-5Ni SMA can be improved by thermomechanical treatments, making them useful for the applications such as large shape memory devices, hard metal/alloy joining in transport systems, protective casings for ceramic parts, nozzles of bottom blown oxygen furnaces for melting of iron and railway rail tracks joining [51]–[55]. The crane rail fishplates are manufactured by using Fe-27Mn-6Si-5Cr-0.05C SMA and Fe-28Mn-6Si-5Cr SMA as shown in Fig. 2.8 [7][56].

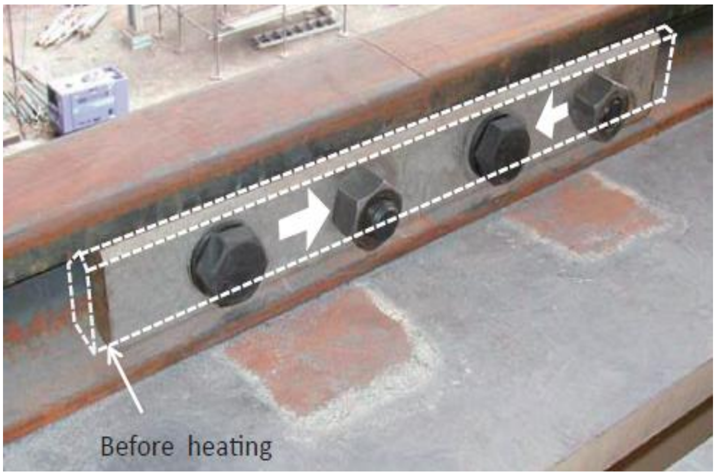

Fig. 2.8: Fishplates [7]

W. Huang has reported the selection of SMAs for actuators amongst three different polycrystalline SMAs using the parameters investigated through differential scanning calorimetry (DSC), laser flash analysis (LFA) and dilatometry [57]. The SMAs are suitable for active vibration control which sometimes uses tuning of material properties in order to control vibrations. SMAs are more suitable for low-frequency vibration control [58]. A ferromagnetic shape memory alloy (FSMA) actuator as shown in Fig. 2.9, shows its working principle where spring is actuated by generating a magnetic field, consequently, the spring elongates. The greater the magnetic flux the larger will be the magnetic field produced. SMAs function as actuators due to their shape memory effect [59].

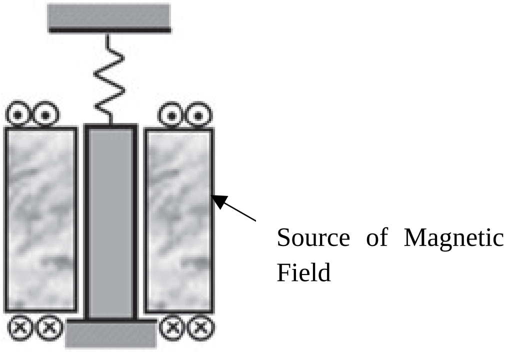

Fig. 2.9: FSMA actuator [59]

The FSMA actuators have the ability to replace pneumatic, hydraulic and electromagnetic drives in many applications. Fe-Ni-Co-Al-Nb has the potential for temperature independent and large-scale actuator applications [60][61]. It has been observed that thermal diffusivity differs considerably during the range of transformation temperatures for active materials and the temperature dependence of thermal diffusivity is very significant when SMA is used as thermally activated actuators because the switching time of actuators is linked with the ability of SMA to transfer heat [62]. Fig. 2.10 shows three different types of SMA actuators; (i) an

SMA element is elongated primarily in the one-way actuator of Fig. 2.10a at low temperature, then it is heated to pull the element P towards left, (ii) heating and cooling of an SMA element cause back and forth movement of P element in the biased actuator of Fig. 2.10b and (iii) alternate heating and cooling of two one-way SMA elements cause back and forth movement of P in the two-way actuator of Fig. 2.10c. Additionally, SMAs can be heated by; (i) passing an electrical current through SMA if it is in the form of wire or spring of small diameter, (ii) passing electrical current through high resistance wire or tape which is wrapped around SMA if there is bulk SMA, or (iii) hot water or hot air or exposing to thermal radiation [63]. It has been revealed that thermomechanical applications of Fe-15Mn-10Cr-8Ni-4Si SMA have not been investigated so far.

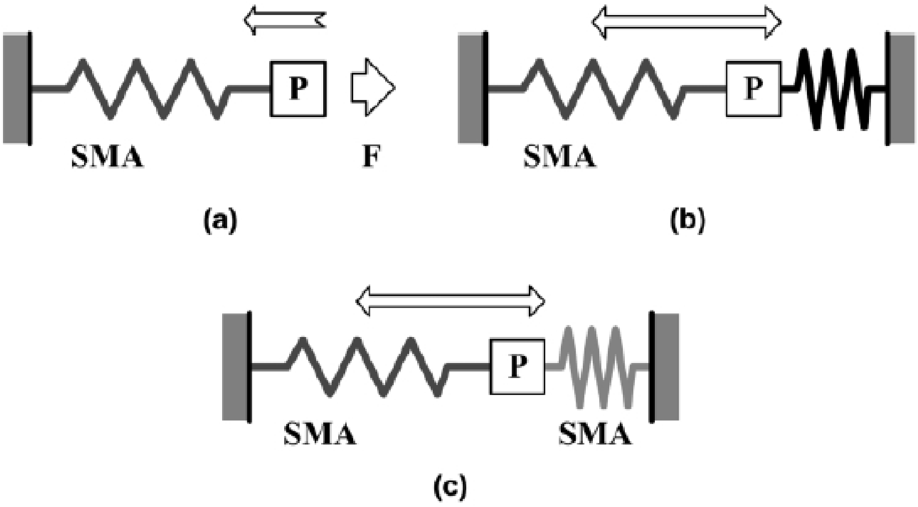

Fig. 2.10: Different basic types of actuators [63]

2.3 Production of investigated alloy

The production of investigated Fe-15Mn-10Cr-8Ni-4Si SMA is the very first step of work done in this thesis, therefore, a brief literature study is performed how to produce the investigated alloy.

Sawaguchi et al. [4] prepared many Fe-SMAs including Fe-15Mn-10Cr-8Ni-4Si SMA by melting different elements and formed into 10kg ingots. Stanford [64] produced the stainless FeMnSi-SMA as a 27g button using arc melting for the analysis of transformation behavior. Stanford et al. prepared FeMnSi SMAs by using arc-melting as 50g buttons under an argon atmosphere using high-purity Fe, Mn and Si [65]. Lin et al. and Gurau et al. produced Fe-28Mn-6Si-5Cr-0.1Ta SMA and Fe-28Mn-6Si-5Cr SMA by an arc melting furnace [66][67]. The Fe-15Mn-7Si-9Cr-5Ni SMA has been prepared by Maji et al. using non-consumable arc melting [68]. Tsuzaki et al. [69] prepared Fe-15Mn-10Cr-8Ni-4Si SMA by electric arc melting which was casted into a 2t ingot for fatigue crack propagation analysis related to martensitic transformation from face centered cubic (fcc) to hexagonal close-packed (hcp) phase. The ingot was hot rolled into a 21mm thick plate which was solution treated at 1100°C for 3600s and subsequently air cooled. The advantage of electric arc melting is that it is pollution free, outstanding metallurgical control (the close control of chemical analysis due to lack of atmosphere), independent control of pressure & temperature, prevent the reactions with atmospheric gases, the undesirable gases and potentially harmful volatile elements are eliminated from the melting chamber, and high temperature (3500°C) can be reached in this method. However, it needs better furnace material, less rust and oil.

Nikulin et al. [6][70] produced shape memory alloys with chemical compositions of Fe-15Mn-10Cr-8Ni-xSi (x = 0, 2, 4, 6 wt.%) by induction furnace melting in order to analyze their low cycle fatigue (LCF). Later, they again produced the investigated Fe-15Mn-10Cr-8Ni-4Si seismic damping alloy by induction furnace melting as 10kg ingots in order to see the effect of strain amplitude on its LCF. The advantage of the induction furnace is that well-controllable melting process, clean, and energy efficient. The life of refractory lining of induction furnace is low as compared to electric arc furnace. Refining in Induction Furnace is not as effective as in electric arc furnace.

Cladera et al. [10] said that the most common method used for the production of FeMnSi-SMAs is a thermo-mechanical process involving melting and casting in high vacuum. It is advantageous in improving the mass production. It is cost-effective as well. The other advantages include the gas elimination in order to control the chemical composition. In recent years, there has been a massive growth in installations of new melting and casting equipment under vacuum. It is mainly due to increasing demand from aerospace and power turbine industries which follow the simple philosophy: “Impurities that are not generated do not have to be removed.” It means, the machine parts which are used under high thermal stress, cleanliness, non-metallic inclusion content and inclusion size are very important because they influence the lifetime of such parts.

The investigated Fe-15Mn-10Cr-8Ni-4Si SMA used in this thesis has been produced by the available facility of electric arc melting at the Institute of Materials and Joining Technology (IWF), Otto von Guericke University (OvGU) Magdeburg, Germany.

2.4 Thermally induced phase transformation

It has been observed from the detailed study of the literature that thermally induced phase transformation behavior of Fe-15Mn-10Cr-8Ni-4Si SMA has not been investigated so far. However, one should know how to perform an analysis for thermally induced phase transformation, which experimental apparatus should be used, how much should be the temperature range for such analysis, and how to understand and elaborate the obtained results. In order to achieve these goals, following literature study on Fe-SMAs other than Fe-15Mn-10Cr-8Ni-4Si SMA has been performed.

Austenite is the high temperature phase with fcc crystal structure whereas martensite is the lowest temperature phase with hcp crystal structure. Austenite start temperature (A_s) is the temperature at which the martensite (or any intermediate phase like R-phase) to austenite transformation starts upon heating of the material. Austenite finish temperature (A_f) is the temperature at which martensite (or any intermediate phase like R-phase) to austenite transformation is completed upon heating. Martensite start temperature (M_s) is the temperature at which the transformation of austenite to martensite starts upon cooling of material. Martensite finish temperature (M_f) is the temperature at which the transformation of austenite to martensite is completed upon cooling. Van Caenegem et al. [71] used Bähr dilatometer in order to determine the transformation temperatures. Koyama et al. and Khalil et al. [72][73] measured the phase transformation temperatures for different FeMnSi-SMAs using differential scanning calorimetry (DSC). Maji et al. [68] also used DSC to determine the forward and reverse martensite transformation temperatures of Fe-15Mn-7Si-9Cr-5Ni stainless steel shape memory alloy. Dogan et al. [74] performed the DSC analysis at heating/cooling rate of 20 K/min. Then exothermic and endothermic events were identified at 325°C and 75°C during heating and cooling, respectively. DSC (Mettler-Toledo DSC 822e) was used by Maji et al. [75] in order to measure the characteristic martensite transformation temperatures of the specimens containing about 50 to 60mg mass at 10 K/min heating/cooling rate.

Though, FeMnSi-SMAs upon cooling can exhibit a martensitic transformation. Phase transition temperatures for Fe-27Mn-25Si SMA were found by using DSC and by dilatometry with thermal cycle's range of -196°C → 350°C. It was done in order to investigate the effects of thermal cycling on transition temperatures M_s, M_f, A_s, and A_f. The DSC curve in Fig. 2.11 shows that the reverse transition temperatures on heating (A_s and A_f) could easily be measured by the intercept method [76]. Thermally induced phase transformation of the Fe-SMA of interest has been investigated in this thesis by means of differential scanning calorimetry.

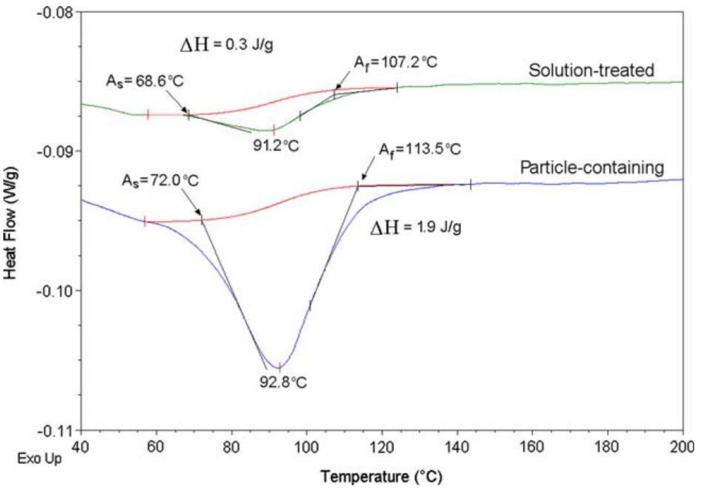

Fig. 2.11: Interception on DSC curves to measure transformation temperature [64]

DSC2920 instrument equipped with liquid nitrogen cooling was used to measure the transformation temperatures of Fe-28Mn-6Si-5Cr and Fe-28Mn-6Si-5Cr-0.1Ta SMAs. Martensite start temperature (M_s) for above-mentioned Fe-SMAs were found to be 11.13°C and -6.39°C respectively in cooling curves whereas enthalpy of transitions are areas under the curves as shown in Fig. 2.12 [77].

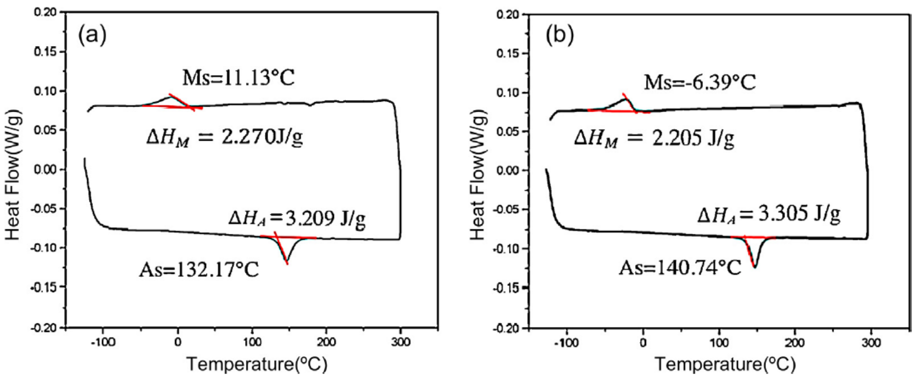

Fig. 2.12: DSC curves for above mentioned SMAs [77]

To circumvent that during DSC measurements the investigated alloy is not consisting a pure martensitic structure. The sample is cooled by liquid nitrogen to approximately -195.8°C and it is assumed that below this temperature no residual austenite should be existing. Then, they were heated in DSC to determine the reverse transformation from martensite to austenite. Disk specimens with a diameter of 5mm were prepared and heated with a controlled rate of temperature with DSC thermal analyzer after immersing into liquid nitrogen for martensitic transformations to take place [72]. Fe-12.5Mn-4.5Si-6.2Ni-9.4Cr-0.5Ti SMA specimen was also immersed in liquid nitrogen before starting the measurement and then heated from room temperature to 300°C, in order to obtain the transformation behavior. The M_s was investigated to be far below the DSC temperature limit [64].

DSC was used with temperature range of 40°C to 300°C and cooling/heating rate of 10 K/min to measure the martensite transformation temperatures (forward and reverse). DSC measurements were made on specimens weighing 40 to 50mg at the range of (-75°C → 200°C) [67][78]. Martensite start temperature (M_s) of FeMnSi-SMAs exists between the temperature ranges of -60°C to 135.85°C, martensite finish temperature (M_f) of FeMnSi-SMAs exists between the temperature ranges of -64°C to 102°C, austenite start temperature (A_s) of FeMnSi-SMAs exists between the temperature ranges of 41°C to 301.85°C, and austenite finish temperature (A_f) of FeMnSi-SMAs exists between the temperature range of 89°C to 387.85°C [79].

2.4.1 The intermediate phase while measurement of thermally induced phase transformation

It is very important to inspect if there exist intermediate phases like the so-called R-phase among others in the material. In most cases, they can influence the material properties in an undesired way.

Sawaguchi et al. observed that ά-martensite intermediate phase (bcc) can exist in Fe-SMAs before deformation. They showed that the alloys in Fe-Mn system possessing ά-martensite intermediate phase exhibit lower number of cycles to fatigue failure (N_f) [4]. Nikulin et al. indicated that ά-martensite is not beneficial for improving LCF resistance [9]. Tsuzaki et al. found out that fatigue cracks have a tendency to propagate through ά-martensite and it can accelerate the secondary cracking and zigzag crack path [69]. Some SMAs have another intermediate phase called rhombohedral phase (R-phase) between austenite and martensite. Upon heating the SMA from low temperature, the material may transform from martensite to R-phase first and then to austenite upon further heating [80]. The difference in bending of SMA orthodontic wires at room temperature is attributed to R-phase which is like a cube with a=b=c but $\alpha=\beta=\gamma\neq 90°$ [81]. Pelton et al. found the emergent R-phase during DSC measurement [82]. Tobushi et al. showed that the slight bend on the loading curve is a plateau phenomenon due to R-phase transformation [83]. The hysteresis related with R-phase is usually narrow and corresponding phase transformation strain upon stressing is also small i.e. about 0.2%, consequently, it cannot be used as actuator other than switch [57]. Fig. 2.13a shows body centered cubic (bcc) lattice showing ά-martensite intermediate phase, whereas, Fig. 2.13b shows rhombohedral lattice showing rhombohedral intermediate phase (R-phase); as discussed above in this paragraph.

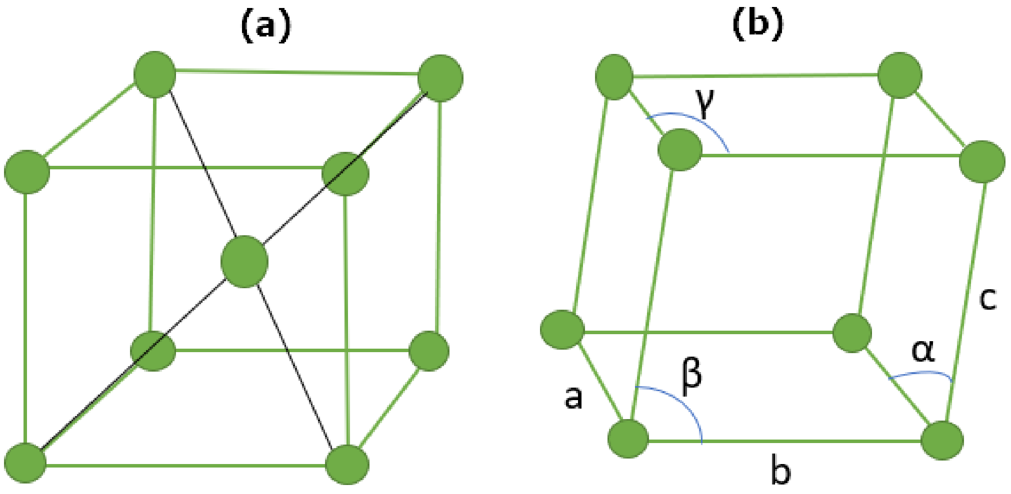

Fig. 2.13: Intermediate phases; (a) body centered cubic (bcc) lattice showing ά-martensite intermediate phase, and (b) rhombohedral lattice showing rhombohedral intermediate phase (R-phase)

The discussion mentioned in this paragraph is very helpful to elaborate the results obtained from differential scanning calorimetry containing intermediate phases. Fig. 2.14 shows the transformation behavior of the specimen weighing approx. 60-100mg and temperature range of 25°C → 625°C at 5 K/min heating rate. According to Fig. 2.14, the specimen with 2% deformation showed two trends in peaks, an endothermic peak which is between 100°C - 200°C as well as an exothermic peak at a temperature range of 400°C - 550°C. Similarly, the specimen with 4 - 10% deformation followed the same trend except for the third endothermic peak (in fact second endothermic peak) between 530°C - 600°C. The first endothermic peak between 100°C - 300°C is possibly associated with ε → γ transformation. Likewise, the second endothermic peak at a range of 530°C – 600°C is associated with ά → γ transformation. It is observed that for the specimen with 6% deformation, the first endothermic peak between 100°C - 200°C associated to ε → γ transformation divides into two more peaks without affecting the other two peaks. At 14% deformation of specimen the first endothermic peak completely splits into two peaks comprising the temperature ranges of 50°C - 140°C and 200°C - 380°C. Alternatively, the second endothermic peak at a range of 530°C - 600°C which is related to ά → γ transformation can only be observed for the specimens having deformation more than 4 %. Reverting the ε-martensite to the parent phase lies in the temperature range of 100°C - 300°C and is shown by the enthalpies of transformation. The quantity of ά-martensite increases by increasing the amount of deformation. It is also evident from the fact that the peak due to ε-γ transformation decreases whereas the peak due to ά → γ transformation increases by increasing the deformation [84].

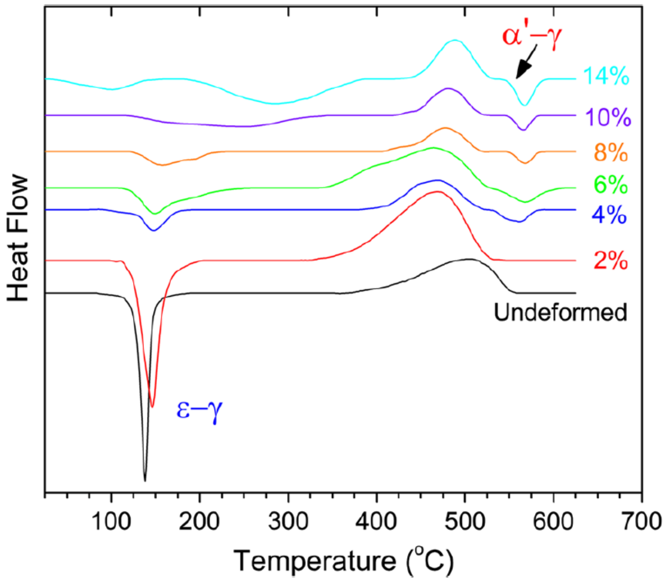

Fig. 2.14: DSC thermograms showing the phase transformation [84]

2.5 Stress-induced phase transformation

The detailed literature study shows that stress-induced phase transformation behavior of Fe-15Mn-10Cr-8Ni-4Si SMA has not yet been investigated. However, it is very important to understand the insight of such type of transformations in order to perform the experimentation associated with stress-induced phase transformation of investigated Fe-SMA.

The stress-strain-temperature diagram in Fig. 2.15 is found to be suitable to learn how to investigate the stress-induced phase transformation for a material. The alloy is in an austenitic state at point O. The alloy is cooled below M_f from O → A without applying any stress, consequently, complete transformation takes place from austenite to martensite (twinned) because it has been cooled below martensite finish temperature, but the material is still un-deformed at A. The stress is applied from A → B, therefore the material is deformed through reorientation and de-twinning of martensite; thus, the material is deformed at B. The load is released from B → C which results into elastic unloading of the reoriented de-twinned martensite, but the material is still deformed at C. The material recovers its initial shape when it is heated from C → D where the austenitic finish temperature is reached [85].

The stress is now applied on austenitic alloy above A_f from O → E, there takes place the stress-induced austenite to martensite transformation. Upon unloading from E → O, there takes place martensite to austenite transformation and the superelastic deformation will be recovered, demonstrating a hysteresis loop in the stress-strain diagram [85].

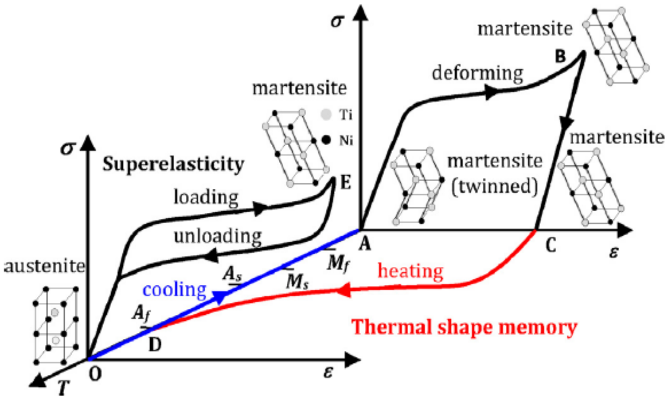

Fig. 2.15: Stress-strain-temperature diagram [85]

Various advantageous mechanical characteristics such as ductility, and strain hardening in austenitic ferrous high-manganese alloys and steels are induced as a result of deformation induced γ to ε martensitic phase transformation (ε-MT) [9], [10], [86]–[88]. In SMAs the martensitic transformation is a crystalline phase change that occurs by applied stresses or by temperature changes. This is a displacive process in which transformation to martensite takes place by shearing mechanism [89][90]. The stress-strain response at different temperatures, the stress-strain responses under loading as well as unloading, and material parameters like modulus of elasticity; are investigated for Fe-SMA of interest through uniaxial compression analysis and biaxial compression analysis.

2.6 Properties of different ferrous based shape memory alloys

FeMnSi-SMAs are being studied intensively as the next-generation structural steels [91]. They exhibit superior mechanical properties owing to characteristic plasticity mechanisms such as mechanical γ-twinning and a deformation-induced γ-ε martensitic transformation; these phenomena are called twinning plasticity (TWIP) effect and transformation-induced plasticity (TRIP) effect respectively [92]. Recently, Sawaguchi et al. [93] proposed that it is possible to use FeMnSi-SMAs for seismic damping, their dampers absorb vibrations of the buildings, however, severe deformations cause fatigue in the damper metal. An FeMnSi-SMA was reported to show a stable damping capacity associated with reversible martensitic transformations under cyclic push-pull loading [94]. The stable deformation behavior with improved fatigue properties makes them highly suitable for application as seismic dampers particularly against long-duration earthquakes. That's why, it was attempted to develop new FeMnSi-SMAs with enhanced LCF (N_f) and a composition of Fe-15Mn-10Cr-8Ni-4Si (wt. %) was found to be fit for this purpose as shown in Table 2.1 [4].

Table 2.1 [4]
Number of cycles to fatigue fracture for different compositions of Fe-SMAs including improved LCF life of the investigated alloy

Sr. #	**Chemical Composition**	**Number of cycles to fatigue fracture, N_f (cycles)**
Fe-xMn		
x = 5	Fe-4.95Mn	278
x = 10	Fe-9.77Mn	294
x = 15	Fe-14.9Mn	426
x = 20	Fe-19.8Mn	684

x = 25	Fe-24.0Mn	1620
x = 30	Fe-28.4Mn	994
x = 35	Fe-32.3Mn	884
x = 40	Fe-39.7Mn	287
Fe-33Mn-ySi		
y = 0	Fe-33.3Mn	917
y = 2	Fe-33.2Mn-1.9Si	2318
y = 4	Fe-33.9Mn-3.9Si	3162
y = 6	Fe-32.5Mn-6.1Si	2833
Fe-30Mn-zSi-(6-z)Al		
z = 0	Fe-30.0Mn-5.8Al	750
z = 1	Fe-29.9Mn-1.0Si-5.25Al	770
z = 2	Fe-30.5Mn-2.0Si-4.1Al	1790
z = 3	Fe-29.9Mn-3.0Si-3.0Al	2112
z = 4	Fe-30.0Mn-4.1Si-2.0Al	8374
z = 5	Fe-30.1Mn-5.0Si-0.97Al	2080
z = 6	Fe-30.1Mn-6.1Si	2024
Fe-15Mn-10Cr-8Ni-sSi		
s = 0	Fe-14.9Mn-10.3Cr-8.1Ni	2858
s = 2	Fe-15.0Mn-10.4Cr-8.1Ni-1.7Si	3205
s = 4	**Fe-15.0Mn-10.0Cr-8.0Ni-4.0Si**	**8466**
s = 6	Fe-15.0Mn-10.4Cr-8.1Ni-1.7Si	4451

2.7 Dimensional changes of material

The literature of dimensional changes for the investigated Fe-15Mn-10Cr-8Ni-4Si SMA is not available at all. However, there must be a knowledge of experimental apparatus, experimental procedure and how to investigate the density change, dimensional changes etc. for the alloy of interest. That's why, the following literature study has been performed.

The shape memory alloy samples have been heated from RT to 130°C with the rate of heating of 280 K/min by means of a dilatometer (DIL 402 C/7 Netzsch), in order to measure the dimensional changes during heating [95]. Huang measured density of SMAs in order to perform their selection for actuators. Transformation temperature and hysteresis decide the environment where the real engineering application of shape memory alloy is. On one hand, high actuation stress is required in some applications, on the other hand, high strain (which corresponds to large displacement) is required. In case of a lightweight actuator instead of actuation stress the specific actuation stress (= stress/density) should be as high as possible [57].

2.8 Biaxial and uniaxial compression

Biaxial compression analysis of the investigated Fe-15Mn-10Cr-8Ni-4Si SMA has not yet been performed. This thesis is also concerned with the mechanical behavior of Fe-15Mn-10Cr-8Ni-4Si SMA under biaxial compression to show and to understand its behavior under complex loading.

It has been observed that multiaxial stresses influence the mechanical behavior of SMAs [96][97][98]. There is high degree of asymmetry between tensile and compressive behavior of SMAs [96][97][99], therefore, mechanical loadings should be performed in all the zones shown in Fig. 2.16 if all mechanical responses of SMA are needed to be observed in this plane. For analyzing the upper semi-plane, tension-compression-internal pressure tests are required on tubular specimen (Fig. 2.16). There are two solutions for analyzing the lower semi-plane (Fig. 2.16); (i) tension-compression-external pressure on tubular specimen which is comparatively difficult and (ii) biaxial compressive test [100]. These tests were initially developed to investigate the behavior of concrete [101] and ice [102]. This biaxial compressive test gives an analysis of left lower quarter zone as shown in Fig. 2.16 [103].

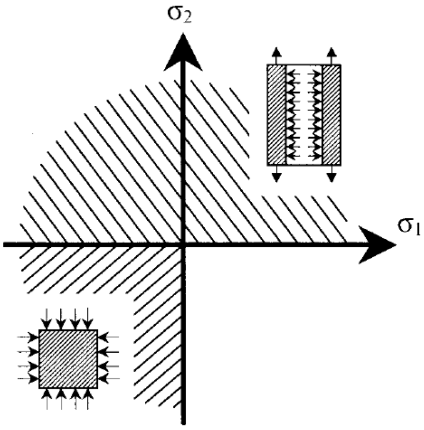

Fig. 2.16: Tension-compression-internal pressure test and bi-compression test [103]

The stress-strain curves for biaxial compression of Cu-Al-Be SMA at 35°C have been reported in Fig. 2.17. These tests are devoted to the study of martensitic transformation [104].

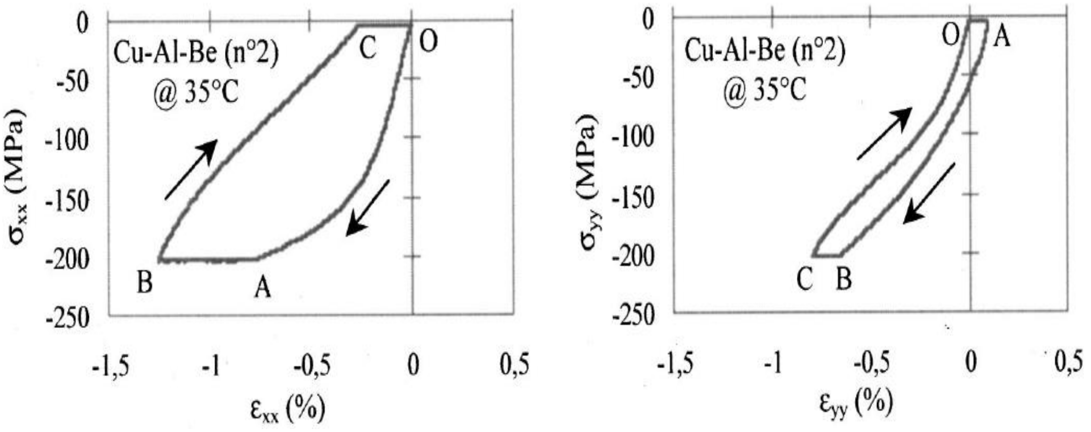

Fig. 2.17: Biaxial compression test showing stress-strain curves in (σ_{xx} ,ε_{xx}) plane and stress-strain curves in (σ_{yy} ,ε_{yy}) plane [104]

The microstructure has also been analyzed in this thesis after deformation by uniaxial compression in order to observe stress-induced ε-martensite (hcp).

Chapter 3

Aim and Focus of the Present Thesis

As discussed in preceding chapters that this thesis focuses on one of the FeMnSiX-SMAs where X shows other elements. They belong to a class of Fe-SMAs which are becoming distinguished nowadays.

3.1 Reason for the selection of Fe-SMA

There are following reasons to select the Fe-15Mn-10Cr-8Ni-4Si SMA in this thesis; (1) it is cheap, (2) it is commercially available, (3) it has been newly invented, (4) increasing rate of applications of Fe-SMAs, (5) its application as seismic vibration control buildings and structures, (6) the research on properties of newly advent of several types of Fe-SMAs during the last decade shows that they have immense potential to be the counterpart of Nitinol, and (7) the complete mechanical behavior and thermomechanical behavior of Fe-SMA have not been investigated so far which are required for many practical mechanical as well as thermomechanical applications.

3.2 Aim of the present thesis

The materials comprising of more than one phases have very special applications where other materials cannot work. The most famous shape memory alloys might be replaced by Fe-SMAs since the research has unfolded their outstanding features as mentioned in chapter 1, therefore, one of the Fe-SMAs is used in this thesis. Numerous researches have been done on Fe-SMAs during last decade. Several studies have been made on mechanical properties of the Fe-SMAs. There are several researches available showing different mechanical applications which exist presently. Interest in Fe-SMAs is still acute due to continuing research on their applications in different fields. They can efficiently be used for several other applications too because their applications and features are not fully discovered, therefore, further research must be done to unfold its advantages and usage. For the future applications, not only mechanical behavior of Fe-SMAs but also the comprehensive view of thermomechanical behavior is important because the phase transformation (austenite ↔ martensite) is also attributed to changes in temperature. It is also required for future thermomechanical modeling of Fe-SMAs. To the author’s knowledge, such a thermomechanical behavior of the valuable Fe-15Mn-10Cr-8Ni-4Si SMA has not been investigated so far to explore its thermomechanical applications, therefore, it has been done in this thesis through experimentation. Besides, a number of significant mechanical investigations are also performed which have not been explored so far.

The scope of the present thesis is to explore the following for Fe-15Mn-10Cr-8Ni-4Si SMA in order to achieve the above-mentioned goals,

- Production of the investigated Fe-SMA.
- The primary objective is the determination of thermal conductivity over a range of temperatures, λ (T) mentioned in Eq. 3.1 for Fe-15Mn-10Cr-8Ni-4Si SMA; which is utmost important to determine the potential of any material for thermomechanical applications as well as due to ever-increasing quantity of materials which can be used in high-temperature applications.

  $$\lambda\ (T) = \alpha\ (T) * \rho\ (T) * C_P\ (T) \tag{3.1}$$

  Where λ (T), α (T), ρ (T) and C_P (T) denote the temperature dependent thermal conductivity, thermal diffusivity, density, and specific heat respectively. These are very significant while using SMA as actuators which require a short-time response. The differential scanning calorimetry is used to measure C_P (T), dilatometry is used to measure ρ (T), and laser flash apparatus is used to measure α (T).
- The prediction of response times of active materials is significant for efficient use as actuators. Rohde et al. observed that thermal diffusivity differs considerably during the range of transformation temperatures for active materials and the temperature dependence of thermal diffusivity is very significant when SMA is used as thermally activated actuators because the switching time of actuators is linked with the ability of SMA to transfer heat [62]. Therefore, this thermal diffusivity over a range of temperatures, α (T) mentioned in Eq. 3.1 for Fe-15Mn-10Cr-8Ni-4Si SMA has been investigated in this thesis.
- The density, ρ (T) and specific heat capacity, C_P (T) over a range of temperatures for Fe-15Mn-10Cr-8Ni-4Si SMA have been investigated which are important to be used in Eq. 3.1 to compute λ (T) whose importance has already been explained.
- Zanotti et al. [105] proved from their numerical work that the dependence of thermal diffusivity, density, specific heat and thermal conductivity on temperature is necessary to start numerical computations.
- The thermally induced phase transformation behavior for Fe-15Mn-10Cr-8Ni-4Si SMA has been investigated in this thesis which decides the environment where the real engineering application of shape memory alloy is.
- The determination if the austenite start temperature, A_s of Fe-15Mn-10Cr-8Ni-4Si SMA is equal to that of human body so that it can be used inside human body. Therefore, A_s for Fe-15Mn-10Cr-8Ni-4Si SMA is investigated in this thesis.
- The austenite finish temperature, A_f is unavoidable to be found out for experimental investigation of pseudoelasticity. Thus, A_f for Fe-15Mn-10Cr-8Ni-4Si SMA is also investigated in this thesis.
- Sawaguchi et al. said that ά-martensite phase (bcc) exists in some materials. They also showed that the alloys possessing ά-martensite phase exhibit a lower number of cycles to fatigue failure (N_f) [4]. Nikulin et al. indicated that ά-martensite is not beneficial for improving LCF resistance [9]. Tsuzaki et al. said that fatigue cracks have a tendency to be propagated through ά-martensite phase i.e. ά-martensite can accelerate the secondary

cracking and zigzag crack path [69]. An approach has been proposed in this thesis to get rid of this disadvantageous ά-phase from Fe-15Mn-10Cr-8Ni-4Si SMA.

- The precise knowledge of dimensional changes of material is crucial for the products which are in contact while heating applications to avoid stresses and possible cracking. It is important because some materials have very high variations with temperature. The expansion of the material is very significant to be considered while designing molds for casting hot materials, beams, and designing large structures where substantial changes in dimension are expected due to temperature. Therefore, the dilatation for Fe-15Mn-10Cr-8Ni-4Si SMA has been investigated in this thesis over a range of temperatures.
- The coefficient of thermal expansion (CTE) is used for design purposes to determine if failure by thermal stress may occur thus design engineers have a considerable interest in CTE values of the material. Khairul Alam et al. said that Invar 36 is useful for aerospace applications because it has a very low value of CTE which means it exhibits very small changes in physical dimensions over a range of temperatures [106]. Therefore, CTE for Fe-15Mn-10Cr-8Ni-4Si SMA has been calculated in this thesis over a range of temperatures as well as the shape recovery, recovery stress, recovery strain, and shape recovery ratio for Fe-SMAs have also been discussed.
- The microstructure of the material and its chemical composition strongly affects the physical properties, therefore, the microstructure of Fe-SMA has been investigated in this thesis prior to all tests. The microstructure has also been investigated after uniaxial compression deformation in order to see what happens to material on microstructure level by uniaxial compression. It is very important to see how different loadings and unloading affect the microstructure.
- The materials containing more than one phases have distinct applications where other materials cannot work, therefore, these phases are needed to be investigated. The properties of materials are affected by accurate crystal lattice structure and lattice planes which are important for structure-based functional studies. It should be investigated what happens to the crystal lattice structure of material upon different types of loadings. All such things have been explored for Fe-15Mn-10Cr-8Ni-4Si SMA in this thesis.
- Martensitic transformation is a crystalline phase change that can be achieved either by applied stresses or by temperature changes. In fact, it is displaced process in which a body-centered cubic parent phase (austenite phase) transforms into martensite (ordered and twinned) by shearing mechanism. Uniaxial compression has also been used to investigate the parameters like start of transformation loading, austenitic modulus of elasticity, residual strain, start of transformation stress during loading, and stress-strain points in the yield curve, yield strength, elastic strain, axial plastic strain, transverse plastic strain, recovery strain, and effect of temperature on the onset transformation stress; which are very important because SMAs take advantage of their large reversible deformation.
- To use Fe-SMAs successfully in new applications, accurate and reliable prediction of their hysteresis response is required. It has been obtained by both loading and unloading processes on sample material during biaxial compression test which is related with stress-induced phase transformation. The mechanical behavior of Fe-SMAs is influenced by biaxial loadings, therefore, an extensive experimental study is necessary to determine; (i) the transformation onset in the left lower quarter plane, and (ii) the possibility of using Fe-SMA in biaxial stresses of high levels. These biaxial outcomes include nominal compressive stress (σ_{yy}), nominal compressive strain (ε_{yy}), nominal stress-strain responses (σ_{yy} - ε_{yy}). Consequently, the biaxial characterization is also significant to be performed for; (i) engineering design, and (ii) numerical modeling. To the author’s knowledge, such type of feasibility study has never been performed on Fe-

15Mn-10Cr-8Ni-4Si SMA. In future, this experimental database will be used for the development of models describing the mechanical behavior of Fe-SMAs under general multiaxial loadings.

The author has performed the detailed review of Fe-SMAs which has also been published in these references [3][17][79][107]. All the facilities required for this work are available at Institute of Materials and Joining Technology (IWF), Institute of Mechanics (IFME) and Institute of Fluid Mechanics and Thermodynamics (ISUT), Otto von Guericke University (OvGU) Magdeburg, Germany.

Chapter 4

Experimental Procedures

4.1 Alloy preparation

The investigated Fe-SMA with material composition described in chapter 1 has been prepared by electric arc melting.

4.1.1 Arc-melting

Five different elements i.e. Ferrous (Fe), Manganese (Mn), Chromium (Cr), Nickel (Ni) and Silicon (Si) have been purchased to produce the investigated Fe-15Mn-10Cr-8Ni-4Si (wt. %) Fe-SMA. These elements are shown in Fig. 4.1.

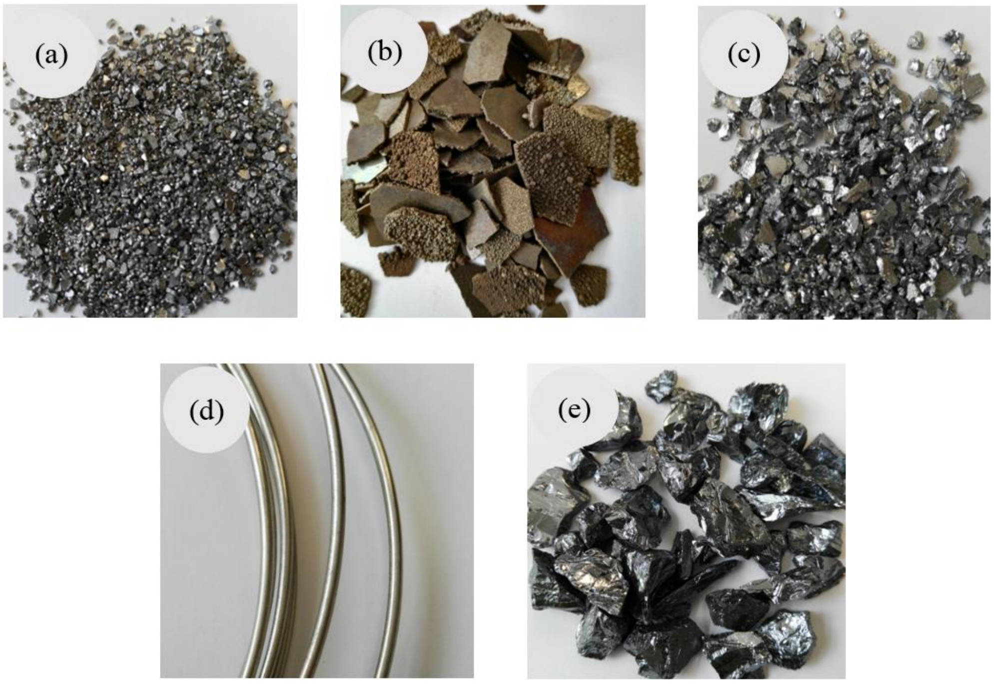

Fig. 4.1: Elements used (a) Fe (b) Mn (c) Cr (d) Ni and (e) Si

The investigated Fe-SMA has been produced having the chemical composition shown in Table 4.1 measured by EDAX energy dispersive spectroscopy (SEM-EDS). At first, the alloy has been produced in the form of a 10g button.

Table 4.1
SEM-EDS chemical composition by weight (wt. %) of different elements in 10g investigated Fe-SMA

Fe	**Mn**	**Cr**	**Ni**	**Si**
62.85	14.63	10.43	7.89	4.2

The investigated Fe-SMA contains the following weight percentage of different elements;

Mn = 15wt. %

Cr = 10wt. %

Ni = 8wt. %

Si = 4wt. %

Fe = Balance = 63 wt. %

Weight of 10g sample has been calculated by well-known relation W = mg, where g = 9.8 m/s^2 hence W = 0.098N. Afterwards, mass of 63wt. % Fe, mass of 15wt. % Mn, mass of 10wt. % Cr, mass of 8wt. % Ni, and mass of 4wt. % Si; are calculated. SARTORIUS electronic micro and analytical precision balance of model CP64 has been used to measure the calculated mass of each of the five elements. However, the exact mass of each element could not be measured as shown in Table 4.2.

Table 4.2
Mass of elements measured by weighing balance for 10g sample

Sr. #	**Element**	**Theoretical mass (gram)**	**Real measured mass (gram)**
1	Fe	6.3	6.3084
2	Mn	1.5	1.5173
3	Cr	1	1.0164
4	Ni	0.8	0.7959
5	Si	0.4	0.4179

Production of the studied alloy has been performed by Compact Arc Melter MAM-1 as shown in Fig. 4.2. This Melter has been designed to melt the samples up to 20g mass and 3500°C temperature. It consists of the following,

1. Dismountable, water-cooled copper crucible plate as shown in Fig. 4.2b.
2. Small melting chamber ensures fast evacuation and low argon gas consumption.
3. Freely movable and water-cooled tungsten electrode has been used to create an arc.
4. Reliable, contactless ignition of the arc.

5. Powerful arc melting generator, integrated in the housing.
6. Eye protector containing a freely movable water-cooled electrode.
7. Pressure Manometer.
8. Valves (integrated in the housing) for evacuation and argon gas inlet into the arc melting chamber.
9. A small roughing vacuum pump (integrated in the housing) for evacuation of the melting chamber.
10. Protection against over-temperature by using a small sensor attached below the copper crucible plate.

Fig. 4.2: (a) Arc melting machine and (b) copper crucible plate

Most of the alloying elements have high affinity for nitrogen, oxygen and hydrogen, hence, formation of oxides and/or nitrides occurs during melting in air which influence the mechanical properties of materials. In order to minimize or avoid the formation of such inclusions, it is necessary to protect the melt from air contact. The vacuum pump has been used to create a vacuum inside the small melting chamber of arc melting machine, which is prerequisite for the insertion of argon inert gas into the melting chamber. Dial gauge shows -1.0bar when a vacuum has been created inside the chamber. Then, switched on the knob of the bottle having inert argon gas letting the gas be inserted into the small melting chamber of the arc melting machine. Pressure manometer shows an increment of pressure from -1.0bar to 0bar after getting insertion of inert argon gas into the chamber. The processes of evacuation and argon insertion have been performed three times. After the creation of inert environment inside the chamber, the vacuum pump is switched off.

The current knob is switched on after switching off the vacuum pump. Tungsten inert gas (TIG) welding process is generally used during arc melting process that’s why it is possible to reach the temperatures of about 4000-10000K in the arc depending on the current. The current of 180A has been used. Five different elements have been melted within few minutes. Switching on/off the current has been repeated three times to prepare an alloy button of good quality. It has been avoided to be repeated more than three times because manganese may evaporate. Additionally, the alloy button is rotated by a stirrer at top of the machine in order to achieve the uniform melting. Tungsten bolt or electrode has been used to create the electric arc. According to the manufacturer specifications, a sample with melting point (MP) up to 3500°C can be melted by arc melting machine, however, a temperature of about 2000°C in the melt has been reached in this work.

Zirconium (Zr) is an element with Atomic Number 40. It has been placed inside the small melting chamber in order to absorb the Residual Oxygen if any or it has been used to absorb any type of oxidation inside the chamber. Zirconium becomes blue whenever there exists residual oxygen inside the chamber or zirconium absorbs Residual Oxygen from the chamber and changes its color within few seconds. It stays metallic whenever there exists no residual oxygen inside the chamber like that in this work.

4.1.2 The produced alloy

The alloy has been prepared in the form of a button as shown in Fig. 4.3. After getting the required button of investigated Fe-SMA, the machine has been cleaned with abrasive fabric dipped in ethanol. The production process of this alloy button has been performed at IWF, OvGU Magdeburg.

Fig. 4.3: Fe-15Mn-10Cr-8Ni-4Si (wt. %) Fe-SMA button

4.2 Analytical methods

The experimental procedures used in this work in order to achieve all the goals described in chapter 3, are mentioned below;

4.2.1 Metallographic preparation

To investigate the microstructure of the alloys, different preparation techniques and analytical methods can be used. Most of them involve metallographic preparation steps such as sample mounting in cold or hot hardening resin, subsequent grinding and polishing steps, and an etching step if necessary.

Diamond or cubic boron nitride (CBN) abrasives are used for cutting the materials having a high value of hardness e.g. above HV700. A Struers cut-off wheel 50A13 has been used during the cutting process of the investigated alloy button. It is lubricated with a cooling liquid to avoid thermal damage. Struers cut-off wheels have been introduced to cut precisely all materials without structural changes because it is free from overheating or deformation. The process of cutting has been performed with simple water cooling at the Institute of Materials and Joining Technology (IWF), OvGU Magdeburg, Germany.

The cutting disks of the investigated Fe-SMA obtained from cutting process are grinded by using waterproof silicon carbide papers FEPA P#n where n=180, 320, 600, 800 or 1200. These silicon carbide papers are produced in the range of grit sizes. The process of grinding has been performed on BUEHLER Alpha Grinder-Polisher. Water has been used as a coolant. Perhaps, the cleaning and drying are the most underestimated processing steps in specimen preparation. Though, misleading results can be caused by improper cleaning. The disks have been cleaned during and after the grinding process with isopropanol and ethanol as well as dried before switching to the other silicon carbide paper. The benefit of cleaning and drying is to protect the material from corrosion. The drying has been performed by Philips beauty jetset control 1900W dryer. From the available dryer, either cold or warm air can be selected to dry the specimen. After completing the process of grinding, the process of polishing has been performed to get the required mirror surface finish of already grinded disks. Polishing is the most important step in preparing a specimen. The process of polishing has been performed on BUEHLER Alpha Grinder-Polisher. Struers MD Mol^{TM} polishing cloth has been used to polish the already grinded disks. MetaDi^{TM} Supreme Polycrystalline Diamond Suspension 3Fμm and Water-based lubricant, have been used on polishing cloth. The cleaning has also been performed after attaining the mirror surface finish of specimen. The specimen has been first cleaned with water, afterwards, the inaccessible abrasives and swarf located in the pores of specimen have been removed by secondary cleaning by ethanol. Now, the sample is ready which has been preserved in the desiccator until SEM and DSC analysis are performed. The processes of grinding and polishing have been performed in the Metallographic laboratory, IWF, OvGU Magdeburg, Germany.

4.2.2 Scanning electron microscopy (SEM)

Microstructure analysis has been performed after successful grinding and polishing processes of the investigated alloy to characterize mainly from a morphological point of view. Microstructural characterization has been carried out by means of a Philips XL30 scanning electron microscope (SEM). The warm embedded specimen has been used for this analysis; it has been grinded and mirror-polished before fitting into SEM. Warm embedding or hot mounting is very important in preparing a specimen for microstructural analysis. G3692 Acheson silver dag 1415 has been applied to the warm embedded specimen before inserting it into SEM as shown in Fig. 4.4a.

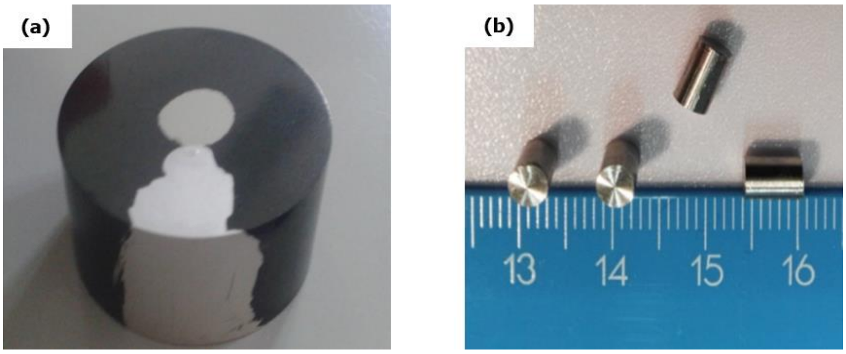

Fig. 4.4: Sample (a) the warm embedded specimen for SEM and XRD analysis (b) undeformed cylindrical specimens for uniaxial compression analysis

This scanning electron microscope has also been equipped with EDAX Energy Dispersive Spectroscopy (EDS) system for chemical composition analysis i.e. chemical composition measurement of the normal surface of the alloy as well as at pores of the alloy. This scanning electron microscope equipped with energy dispersive spectroscopy is available at the Institute of Materials and Joining Technology (IWF), OvGU Magdeburg, Germany.

4.2.3 X-ray diffraction (XRD)

X-ray diffraction (XRD) is a vital tool for structure determination which provides the most direct way of forming three-dimensional images of molecules. It is a technique primarily used for phase identification of a crystalline material and can provide information on unit cell dimensions. It can provide the detailed information on molecular architecture, interatomic distances and bond angles. In fact, it is the study of crystal structure by means of the diffraction of X-rays. Crystals are the objects (molecules, atoms, and ions) arranged in a regularly repeating pattern in three dimensions called unit cells which are characterized by six parameters: three axial lengths (a, b and c) and three inter-axial angles (α, β, γ) e.g. hcp, bcc and fcc crystal lattice structures. X'Pert pro x-ray diffractometer has been used to analyze the crystal lattice structure of the investigated Fe-SMA. The analysis has been performed using warm embedded specimen shown in Fig. 4.4a which has been first grinded and mirror polished and additionally, electrolytic polishing has been performed with very low pressure at a higher amount of time. This electrolytic polishing has been performed in three steps, each of which has taken 2-3hours. During the first step, TexMet polishing cloth and Struers DiaPro Largo 9µm polishing suspension have been used. During the second step, MD-Mol polishing cloth and Aka-Mono 3µm polishing suspension have been used. During the third step, BUEHLER VibroMet 2 vibratory polisher, Struers MD Nap^{TM} polishing cloth (300mm diameter) and BUEHLER Masterprep 0.05µm polishing suspension have been used. The equipment is available at the Institute of Materials and Joining Technology (IWF), OvGU Magdeburg, Germany.

4.2.4 Differential scanning calorimetry (DSC)

Differential scanning calorimetry (DSC) is one of the most employed thermal analysis methods. It is used to analyze any of the energetic effects which occur in liquid or solid during thermal treatment. DSC is operated as per heat flux principle in which sample and reference are exposed to controlled temperature e.g. heating, isothermal or cooling. The sample and reference are maintained at approximately the same temperature throughout the measurement as shown by the colored dotted line in Fig. 5.7 where green dots are representing the reference. Usually, the temperature of the sample holder increases linearly as a function of time during the DSC measurement. Differential scanning calorimeters measure the difference in heat flow between the sample and reference (DSC (uV/mg)) as a function of temperature and time. They measure the amount of heat absorbed or released during transition (DSC (uV/mg)) as a function of temperature and time. They measure difference in the amount of heat required to raise the temperature of a sample and reference (DSC (uV/mg)) as a function of temperature and time. The reference must have well-defined heat capacity over the range of temperatures.

The instrument used is Pegasus® DSC 404 C thermal analyzer (Netzsch-Gerätebau GmbH) as shown in Fig. 4.5, which is eminent in determining the thermodynamic properties of ceramics and metallic high-performance materials. These instruments are usually used to find accurate specific heat capacity (C_P).

Fig. 4.5: Pegasus DSC 404 C thermal analyzer

It has been equipped with a turbo-molecular pump for the measurements under high vacuum. The vacuum-tight construction of the system permits performance of quantitative enthalpy and C_P determinations in a pure gas atmosphere or under vacuum. Graphite furnace has been used because the temperature range has only been required till 400°C. DSC-C_P sensor type S used is capable of measuring the C_P values. Platinum/Rhodium (Pt/Rh) crucible has been used as shown in Fig. 4.6, which is best suited to C_P measurement and very expensive as well. This crucible is located inside the DSC furnace. Pt/Rh crucible with an Al_2O_3 liner has been used in order to prevent the chemical reactions. The DSC Proteus software has been used to evaluate the resulting data. Five samples (small disk specimens of the investigated Fe-SMA) having 5mm diameter and 0.5mm thickness have been prepared for DSC measurement whereas the reference used is aluminum oxide (Al_2O_3).

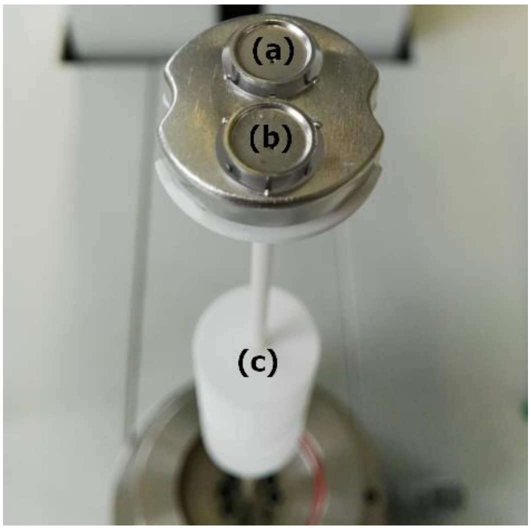

Fig. 4.6: DSC crucible; (a) Reference or R cup made of Platinum/Rhodium (b) Sample/Probe or P cup made of Platinum/Rhodium and (c) white ceramic part made of Al_2O_3

The specific heat capacity (C_P) or specific heat is the amount of heat required to raise the temperature of 1kg by 1K. The water has very high value of C_P or it takes a lot of heat to become hot or it plays a very important role in temperature regulation as it is able to absorb a lot of heat without a significant rise in temperature.

M. K. Stanford [108] calculated the C_P as a function of temperature by following well-known Eq. 4.2 where the values of masses of sample and reference were already known;

$$C_P = q/m\Delta T \tag{4.2}$$

In Eq. 4.2, q is the heat supplied to the material of mass m in order to produce a change in temperature of ΔT.

The following procedure has been adopted during DSC measurement in this work:

1. It has been made sure prior to the measurement that melting point (MP) of the sample is far above the temperature limit used i.e. 400°C. The melting point of Fe-28Mn-6Si-5Cr SMA has been found to be 1320°C-1350°C. The melting point of each element of the investigated Fe-SMA is found to be far above the selected temperature range (20°C to 400°C). The 20°C is the laboratory temperature, therefore, measurement has been started from 20°C.
2. The mass of disk specimen has been measured.
3. The disk specimen has been placed into the DSC crucible (Fig. 4.6).
4. Vacuum up to 3-2mbar has been created inside the DSC furnace by simple rotary or diaphragm vacuum pump.
5. Further vacuum up to $1.4\text{x}10^{-4}$ mbar has been created inside the same furnace by Turbo Molecular Pump. The range of this pump is up to $2.5\text{x}10^{-5}$ mbar.
6. The steps 4 and 5 have been repeated to get rid of air and oxidation from the furnace chamber.
7. Argon inert gas has been inserted into the furnace of DSC. Oxidation is avoided by means of argon atmosphere.
8. Heating and cooling cycles have been performed at a rate of 10 K/min between 20°C to 400°C in the presence of argon inert gas.
9. The empty “a” and “b” cups of DSC crucible (Fig. 4.6) have been heated without sample and reference until the heating cycle has been completed and results are obtained. Such type of heating cycle is called as Baseline (BL) cycle. It is invisible in Fig. 5.7, but it is nearly horizontal straight line starting from near zero value of DSC (uV/mg) on y-axis. It is not zigzag like other curves of Fig. 5.7, because the cups are empty having no material, consequently, there is no change in specific heats as well as there is not any difference of masses.
10. Now, the only reference has been heated after keeping it in “b” cup of DSC crucible (Fig. 4.6), until the heating cycle has been completed and results are obtained.
11. The C_P values for reference are known as excel file which is plotted in the graphical form as shown in Fig. 4.7.

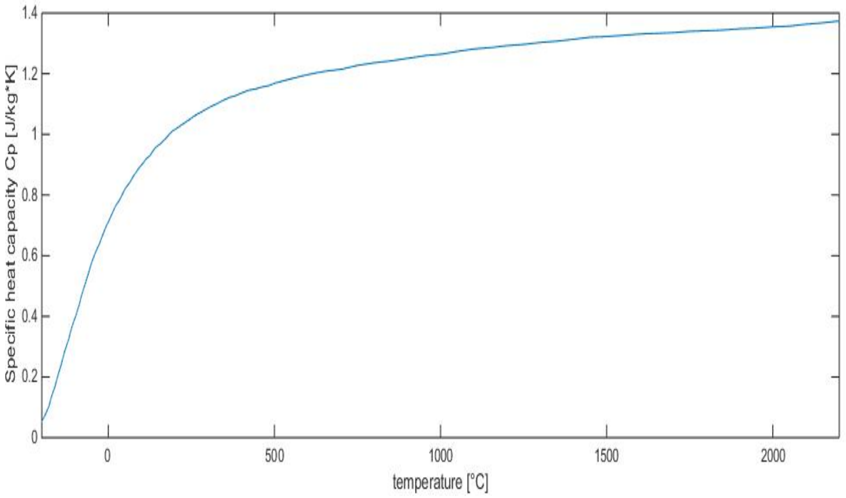

Fig. 4.7: Specific heat capacity (C_P)-temperature diagram for reference

12. The reference has been taken out from “b” cup of DSC crucible (Fig. 4.6) and sample has been inserted in the same cup and heated until the heating cycle has been completed and results are obtained.
13. Now the following Eq. 4.4 can be used for the required C_P calculations,

$$C_p(\vartheta)_{Probe} = \frac{m_{Standard}}{m_{Probe}} + \frac{DSC\ (\vartheta)_{Probe} - DSC\ (\vartheta)_{BL}}{DSC\ (\vartheta)_{Standard} - DSC\ (\vartheta)_{BL}} * C_p(\vartheta)_{Standard} \tag{4.3}$$

or

$$C_p(\vartheta)_{Sample} = \frac{m_{Reference}}{m_{Sample}} + \frac{DSC\ (\vartheta)_{Sample} - DSC\ (\vartheta)_{BL}}{DSC\ (\vartheta)_{Reference} - DSC\ (\vartheta)_{BL}} * C_p(\vartheta)_{Reference} \tag{4.4}$$

The specific heat capacity of sample ($C_P\ (\vartheta)_{sample}$) is the only unknown parameter in Eq. 4.4. The $m_{reference}$ = 41mg. The masses m_{sample} is also known. The values of specific heat capacity of reference ($C_P\ (\vartheta)_{reference}$) are known as in Fig. 4.7. The values of DSC $(\vartheta)_{sample}$ - DSC $(\vartheta)_{BL}$ are shown by the sample curves in Fig. 5.7, whereas the values of DSC $(\vartheta)_{reference}$ - DSC $(\vartheta)_{BL}$ are shown by the reference green curves in Fig. 5.7.

14. There is an isothermal cycle for a short time just after the completion of heating cycle in order to get the (i) precise and accurate results and (ii) to get rid of the measurement errors if any, afterwards, there is a process of cooling as shown in Fig. 5.7 until the cooling cycle has been completed.
15. Air cooling has been used due to lack of CC 200 L liquid nitrogen cooling system for the low-temperature furnace.
16. The voltage “V” of thermocouple has been measured and power “W” has been kept constant in this Pegasus® DSC 404 C. Therefore, the results are in the form of *DSC/(uV/mg)* (not in the form of DSC/(uW/mg) like other DSCs) where V stands for voltage and u stands for micro (μ). Likewise, the case of strain measurement using strain gauges where the strain is shown in voltage.
17. Proteus Software has been used to evaluate the resulting data.

The DSC measurement of the sample has been performed six times at the Institute of Fluid Mechanics and Thermodynamics (ISUT), OvGU Magdeburg, Germany. Table 4.3 shows the preliminary conditions at which the measurement has been performed.

Table 4.3
Preliminary conditions for experimental work

Sr. #	General Information during experimental work	Reference	Sample
1	Material	Al_2O_3	Fe-15Mn-10Cr-8Ni-4Si SMA
2	Instrument	Pegasus DSC 404 C	Pegasus DSC 404 C
3	Specimens	Small disk specimens of Al_2O_3	Small disk specimens of Fe-15Mn-10Cr-8Ni-4Si SMA
4	Average diameter of specimen	5mm	5mm
5	Temperature range	20°C to 400°C	20°C to 400°C
6	Heating rate	10 K/min	10 K/min
7	Cooling rate	10 K/min	10 K/min
8	Reference Temperature (Lab or Room Temperature)	20°C	20°C
9	Atmosphere	argon	argon

4.2.5 Pushrod dilatometry

Pushrod dilatometry is a method for determining dimensional changes versus temperature or time when the sample undergoes a controlled temperature program. The apparatus used is Netzsch DIL 402 C as shown in Fig. 4.8, which has a temperature range of RT to 1600°C and gives precise information on expansion during thermal analysis. It has the following features, (i) easy to use, (ii) few clicks to start the measurement, (iii) simplified operation, (iv) safe operation, (v) gas-tight design and superior insulation of sample's section which reduces effects of temperature fluctuations on the measurement producing the precise results, and (vi) contact pressure on the sample remains constant during the whole measurement time irrespective of its expansion, which helps to measure without breakage and deformation. The apparatus used is available at the Institute of Fluid Mechanics and Thermodynamics (ISUT), OvGU Magdeburg, Germany. It operates as per national and international standards like DIN EN 821, DIN 51045, ASTM E831, ASTM E228. For calibration of the instrument, six standards having a range of coefficients of thermal expansion have been obtained from National Institute of Standards (NIST) which are measured against one another.

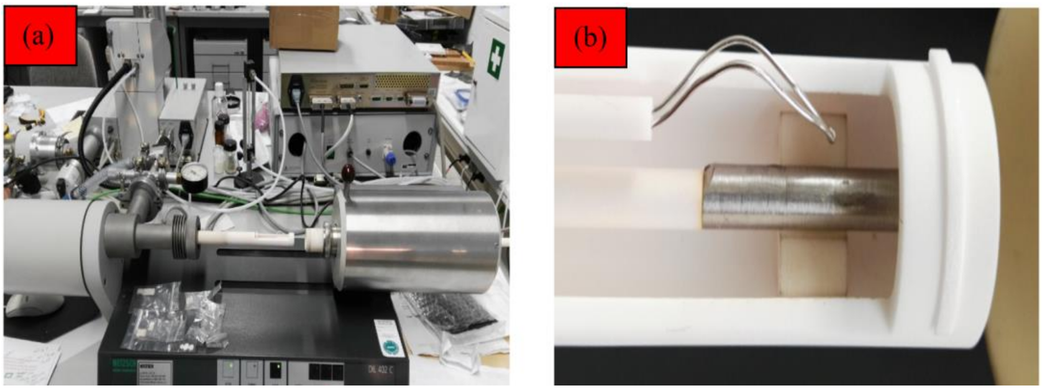

Fig. 4.8: (a) Netzsch DIL 402 C apparatus and (b) specimen holder having specimen along with an S-type thermocouple

Pushrod dilatometry consists of four vital components; (i) measuring unit comprising of furnace and sample holder, (ii) pushrod (iii) displacement system and (iv) data acquisition system including a computer; as shown in Fig. 4.8a. The thermocouple is mounted laterally on the sample carrier tube as shown in Fig. 4.8b; which measures the absolute temperature of the sample (RT to 1600°C). The thermocouple is made adjustable in order to measure the temperature at various sample lengths conveniently. A guiding rod keeps thermocouple in the desired position without bending. A sensor acting as linear encoder can encode into digital signals. The unique, reliable and efficient Proteus® dilatometer software is used.

The rod-shaped specimen (25.073mm x 4.096mm) as shown in Fig. 4.9 where 25.073mm is the length and 4.096mm is its diameter; has been used for this measurement. Its preparation is as per national and international standards like DIN EN 821, DIN 51045, ASTM E831, and ASTM E228. It has been prepared by the process of turning on lathe machine and the process of side milling on a milling machine at workshop of the Institute of Mechanics (IFME), Mechanical Department, OvGU Magdeburg, Germany.

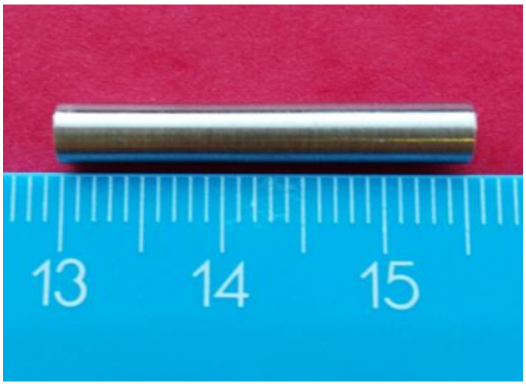

Fig. 4.9: Sample (rod-shaped specimen) for dilatometry measurement

The main interest is to investigate the behavior of the alloy after making it complete martensite by making the alloy temperature below martensite finish temperature (M_f) using liquid nitrogen dip prior to the dilatometry measurement because liquid nitrogen is at an extremely low temperature. The measurement is prepared by inserting the sample into the sample holder and bringing it into contact with pushrod as shown in Fig. 4.8b. The sample holder is located inside the furnace of the apparatus. After closing the furnace, the measurement can be started by evacuating the test chamber using a vacuum pump to reduce the presence of oxygen and filling pure inert argon gas with a flow rate of 75 ml/min. The process of evacuation and filling is repeated three times. Therefore, the measurement is performed in a pure inert argon gas using a pushrod dilatometer according to a standard test procedure. The sample is heated with a rate of 5 K/min. The expansion of the specimen is compared with that of reference (aluminium oxide Al_2O_3). The thermal expansion of the sample is detected by the displacement system which the pushrod is connected to. Now, it is possible to make the measurements by using Proteus® dilatometer software.

4.2.6 Laser flash analysis (LFA)

The experimental work is based on heating the Fe-SMA sample, radiating with laser and recording the temperature history at various positions of the sample. The apparatus used in this work is Netzsch LFA 427 as shown in Fig. 4.10, which has a temperature range of RT to 1550°C. It operates as per national and international standards like ASTM E1461, DIN EN 821, DIN 30905, ISO 22007-4 and ISO 18755. It has advantages over direct measurement of thermal conductivity like; (i) non-contact method, (ii) non-destructive method, (iii) sample geometry is simple, (iv) easy to prepare the sample, (v) sample size is small, (vi) applicability for a wide range of diffusivity values, (vii) excellent accuracy, (viii) reproducibility, (ix) very little time is required for any measurement, (x) a wide range of temperatures is covered within a short period of time, (xi) a compact enclosed system with space-saving design meets the highest safety (laser class 1); no additional safety precautions are essential, (xii) simple and horizontal insertion of the sample, (xiii) short distances involved, minimize the loss of laser energy & energy impinging upon IR detector and (xiv) measurements are possible to be carried out in static or dynamic, and oxidizing or inert gas atmosphere or under vacuum. The apparatus used is available at the Institute of Fluid Mechanics and Thermodynamics (ISUT), OvGU Magdeburg, Germany.

Fig. 4.10: (a) Netzsch LFA 427 apparatus and (b) specimen holder having specimen along with a thermocouple

Netzsch LFA 427 consists of four vital components; (i) measuring unit comprising of the furnace with red graphite heating element, sample carrier and infrared (IR) detector, (ii) controller for measuring unit, (iii) laser system and (iv) data acquisition system including a computer: as shown in Fig. 4.11. The measuring unit is connected to the laser system by a glass fibre. The sample is placed on sample carrier located above an aluminum oxide (Al_2O_3) sample carrier tube, it is shown in yellow color in Fig. 4.10 and Fig. 4.11. This tube is mounted on the recipient block which is situated above laser optics. The thermocouple is also mounted laterally on this tube as shown in Fig. 4.10b and measures the absolute temperature of the sample (RT to 1550°C). Several thermocouples are available depending upon temperature range of interest. The laser produces a pulse having energy which is the requirement of LFA technique. Its emission wavelength is 1064nm thus lies in infrared range shown in Table 4.4. However, the pulse width of the laser varies.

Table 4.4
Electromagnetic spectrum

γ-rays	X-rays	ultraviolet	visible	**infrared**	microwaves	radio waves

A vacuum seal helps to create a vacuum, it acts as a gas-tight coupling between furnace & recipient block and allows the measurements under high vacuum or in static/dynamic inert gas atmosphere or in oxidizing atmospheres. The furnace system can be raised/lowered using hoist driven by a motor. An IR detector measures the temperature increase on the rear face of the sample.

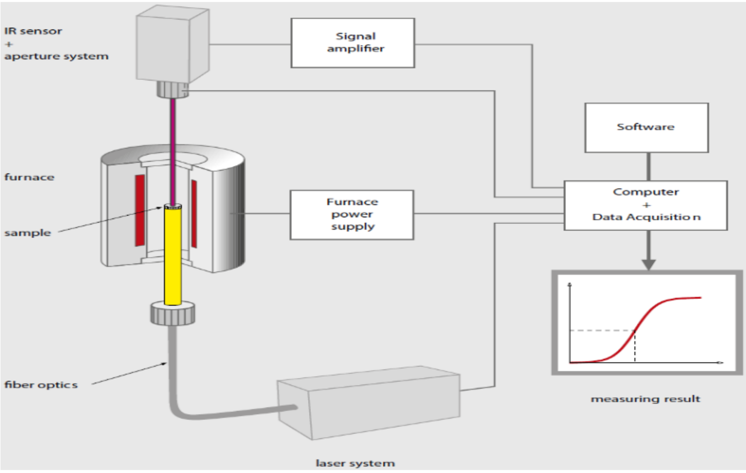

Fig. 4.11: Principle of Netzsch LFA 427 apparatus (Netzsch)

The disk specimens of 12.5mm x 2.5mm have been used for LFA measurement, where 12.5mm is the diameter and 2.5mm is thickness. Its preparation is as per national and international standards like ASTM E1461, DIN EN 821, DIN 30905, ISO 22007-4 and ISO 18755. These specimens as shown in Fig. 4.12 have been prepared by the process of turning on lathe machine and process of side milling on a milling machine at workshop of the Institute of Mechanics (IFME), Mechanical Department, OvGU Magdeburg, Germany.

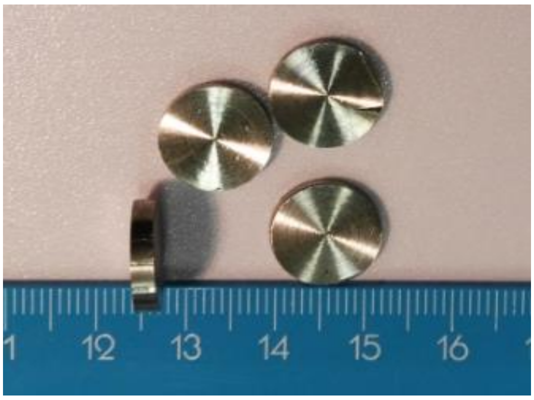

Fig. 4.12: Sample (disk specimens) for LFA measurement

The sandblasting process has been performed to apply a coating on the specimen before starting the experimental procedure. The Renfert sandblasting unit has been used for this purpose. Small 25-50µm particles of aluminum oxide (Al_2O_3) have been used as sandblasting material. The sandblasting tank is filled with these particles, the specimen is put inside the sandblasting chamber, and afterwards, the handpiece spreads these particles on the specimen. The single layer of particles having 10µm to 50µm thickness has been applied around the whole specimen. Note: Graphite is used as sandblasting material in case of testing the non-metals unlike Al_2O_3 particles for metals. Graphite is not used for metals because it has carbon which diffuses in the material and changes the properties, thus causing problems with metals. This process has been performed to get rid of expected reflections during LFA experiment as well as to increase the emissivity and absorptivity of the sample. These reflections cause problems because the laser is reflected from the sample while shooting, then IR sensor on the top measures not only the emitted energy from the sample but also the reflected energy because the sample has high reflectivity.

The experimental procedure starts by mounting the coated sample on sample carrier located inside the furnace, evacuating the test chamber by vacuum pump to reduce the presence of oxygen and then filling pure inert argon gas with flow rate of 75 ml/min at approximately ambient working pressure (a slight above ambient pressure) because argon continuously flows in (through inlet pipe) and flows out (through exhaust pipe) during the whole measurement. The sample is heated by means of the furnace not by laser, the laser is only for the measurement. Moreover, LFA measurement is not taken during heating or cooling like that in DSC measurement; rather it is taken when some special/specific/predetermined temperature has been reached and becomes stable. If the sample is heated or cooled during LFA measurement and there is no stability, then accurate and precise measurements are not possible to be obtained. In other words, when the sample reaches a special temperature (e.g. each of 25.8°C, 50.4°C, 99.1°C, 199.8°C, 300°C and 400.2°C) and becomes stable, then laser shoots and a burst of energy originating from pulse of laser is absorbed on the front face of the coated sample causing homogeneous heating. After that, IR detector measures the increase of relative temperature as a function of time on the other rear face of the coated sample. Now, thermal diffusivity can be measured by means of software. Note: The beauty of LFA measurement is that it replaces the troublesome measurement of laser energy absorbed by the sample and absolute temperature increase with accurate and direct measurement of time versus relative temperature increase.

4.2.7 Uniaxial compression

The Zwick/Roell Z100 materials testing machine as shown in Fig. 4.13 has been used in this work to perform uniaxial compression analysis. It can test up to 100kN. It has advantages e.g.; (i) fast and easy to operate, (ii) very low speeds can be set with excellent speed-accuracy, (iii) high test speed range can be used without restriction, (v) equipped with Xforce load cells which are very stable and less sensitive to transverse forces in compression and flexure tests, (vi) fast measurement using high data transmission rate of 2000Hz, (viii) precise force, (ix) strain control, (x) minimal force changes on the specimen can be recorded and displayed precisely, and (xi) high safety. It operates as per national and international standards like ASTM E4 and DIN EN ISO 7500-1 for standard practices for the verification of force of testing machines and calibration/verification of static uniaxial testing machines respectively. The specimen holder in testing machine is surrounded by thermal system which heats up the specimen to the required precise temperature. The testing machine is available at the Institute of Materials and Joining Technology (IWF), OvGU Magdeburg, Germany.

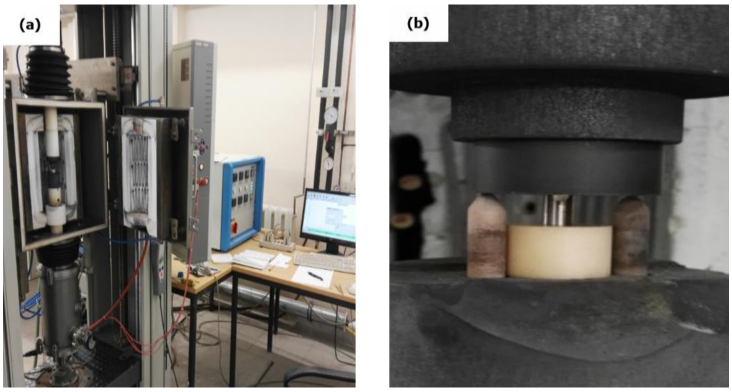

Fig. 4.13: (a) Zwick/Roell Z100 materials testing machine and (b) specimen holder having specimen

Cylindrical specimens of 6mm x 4mm prepared from 15g button have been used for uniaxial compression test, where 6mm is the height and 4mm is the diameter of solid cylinder. Its preparation is as per national and international standards like ASTM E4 and DIN EN ISO 7500-1. These cylindrical specimens as shown in Fig. 4.4b have been prepared by the process of turning on lathe machine and process of side milling on milling machine at workshop of the Institute of Mechanics (IFME), Mechanical Department, OvGU Magdeburg, Germany.

4.2.8 Biaxial compression

All the tests related to biaxial part are performed on WPM BIAXE100-14620 biaxial testing machine (Fig. 4.14) which has servo-hydraulic actuators. It has a maximum static test load up to 100kN, a dynamic test loads up to 10kN at a maximum of 5Hz and total stroke of 300mm per axis. A variety of strain measuring devices, e.g. strain gauges and extensometer, generate the input signals. The data acquisition is performed by an object-oriented programming software. The digital controller permits each actuator to be independently controlled. The testing machine is available at the Institute of Materials and Joining Technology (IWF), OvGU Magdeburg, Germany.

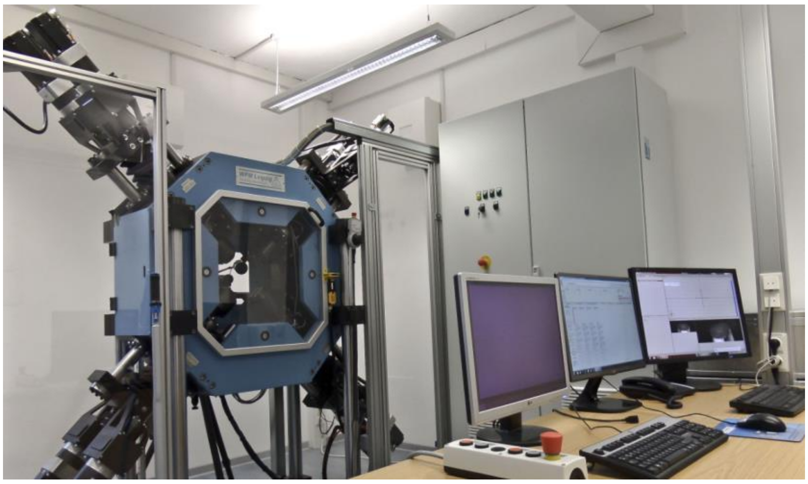

Fig. 4.14: WPM BIAXE100-14620 biaxial testing machine

The square sheet (4.2mm x 4.2mm x 1mm) specimens as shown in Fig. 4.15 are used for biaxial compression analysis, where 4.2mm is the length of each side and 1mm is its thickness.

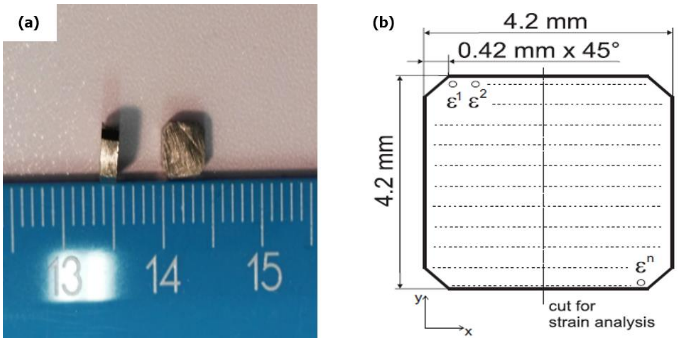

Fig. 4.15: Sample (a) square sheet specimens for biaxial compression analysis (b) Zillmann et al. [109] geometry of biaxial compression specimen

These specimens are prepared as per geometry of Zillmann et al. [109] shown in Fig. 4.15b, at workshop of the Institute of Mechanics (IFME), Mechanical Department, OvGU Magdeburg, Germany.

4.2.9 Hardness test

The equipment used for measuring the hardness of investigated Fe-SMA is HBRVU-187.5 Brinell Rockwell and Vickers Optical Hardness Tester as shown in Fig. 4.16. It is suitable for testing the hardness of ferrous metals. Multiple testing methods like Brinell, Rockwell or Vickers hardness tests are possible using it by selecting different indenters.

Fig. 4.16: HBRVU-187.5 Brinell Rockwell and Vickers Optical Hardness Tester

Chapter 5

Results and Discussions

This chapter summarizes the results obtained from the experimental procedures described in chapter 4. The discussions on these results have also been performed in this chapter.

5.1 Thermally induced phase transformation and specific heat of the investigated Fe-SMA over a range of temperatures

Obviously, understanding of the thermal behavior of smart material is not possible without reflecting the basic principles of thermally induced phase transformation. In many engineering applications, the structures and components experience thermal loadings. The phase transformation behavior decides the environment where the real engineering application of shape memory alloy is. The thermally induced phase transformation behavior is also vital to be determined because the phase transformation is attributed to changes in stress and/or temperature and many characteristics are induced in SMAs as a result of γ to ε martensitic phase transformation. In this section, a series of DSC measurements are performed in order to investigate the numerous aspects of thermal behavior and thermally induced phase transformation of Fe-15Mn-10Cr-8Ni-4Si SMA.

The DSC measurement of the investigated Fe-SMA specimen has been performed four times between 20°C to 400°C at a rate of 10 K/min using graphite furnace built inside the Pegasus DSC 404 C thermal analyzer. The mass of the specimen is 41mg. Steps 1 to 17 of subsection 4.2.4 have been performed to obtain the DSC results. Four runs of the specimen have been performed. First three runs of the specimen have been performed without any prior nitrogen dip before starting the measurement, however, the fourth run has been performed with prior nitrogen dip. The main interest is to investigate the behavior of the alloy after making it complete martensite by dipping into the liquid nitrogen. In this way, the alloy temperature has been brought below martensite finish temperature (M_f) in order to make it fully martensite because liquid nitrogen is the nitrogen in the liquid form at an extremely low temperature, colorless, clear liquid, with a density of 0.807 g/ml and the boiling point of -195.8°C.

5.1.1 The results of first run of the specimen without prior nitrogen dip

Fig. 5.1 shows DSC heating curve for the sample as well as for reference, and DSC cooling curve for the sample as well as for reference; during first run of the specimen. In Fig. 5.1, blue curve shows heating of the reference, then an isothermal vertical portion of the same curve comes, and after that brown curve shows cooling of the reference; these curves are exactly the same as complete green curve in Fig. 5.7. In Fig. 5.1, black curve shows heating of the sample, then an isothermal vertical portion of the same curve comes, and after that henna green curve shows cooling of the sample; these curves are exactly the same as complete red curve in Fig. 5.7. By comparing brown and henna green cooling curves in Fig. 5.1, it has been found that 10 K/min rate remains constant from 400°C to 175°C because both curves move parallel from 400°C to 175°C which can also be seen in excel data. After that sample cooling curve (henna green curve) deviates towards reference cooling curve (brown curve) which means the cooling rate is no more 10 K/min rather it can be calculated by dividing the temperature value to the value of time at any specific point on curve, these values of temperatures and time can be obtained from excel data of the results, therefore the measurement has been stopped. The martensite start and finish temperatures (M_s and M_f) are not possible to be calculated because there exists no reverse transformation (γ-austenite fcc → ε-martensite hcp OR γ-austenite fcc → ά-martensite bcc) while cooling in DSC till 115°C. The reason is that the instrument used in this work has been designed only for heating. Hence, it can be concluded that M_s and M_f are far below the limit of the DSC instrument.

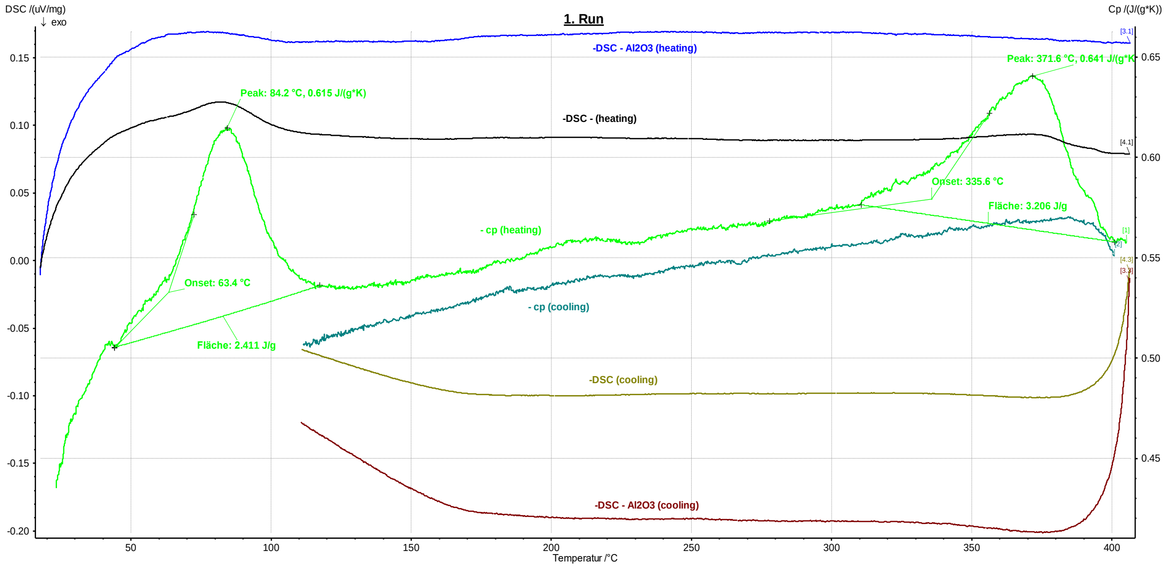

Fig. 5.1: Temperature Modulated DSC (TM-DSC) measurement of first run of the specimen without any prior nitrogen dip, compared with that of reference (Temperature-heat flow curves)

The specific heat capacity (C_P) has now been calculated using Eq. 4.4 by means of the DSC results mentioned in Fig. 5.1. The light green curve in Fig. 5.2 shows heating (C_P vs T) of the sample and green curve shows normal air cooling (C_P vs T) of the sample during first run of the specimen over a range of temperatures between 20°C to 400°C without prior nitrogen dip. There are two endothermic peaks in light green curve showing two thermally induced phase transformations in the investigated Fe-SMA. The first endothermic peak in the range of 40°C-120°C is associated with ε→γ transformation whereas the second endothermic peak between 300°C-400°C is associated with ά→γ transformation. The XRD analysis proves the existence of bcc crystal lattice structure in the investigated Fe-SMA which denotes α-ferrite phase which causes magnetic properties and a classic example of ferromagnetic material. Sawaguchi et al. said that this is actually ά-martensite phase (bcc) which can exist before deformation [4]. Consequently, it can be concluded that the two endothermic peaks showed by investigated Fe-SMA are associated with the transformation of two different fractions of the martensite. These two thermally induced phase transformations of the alloy have been occurred at 63.4°C as well as at 335.6°C respectively. The austenitic start temperature (A_s) resulted from the first and second endothermic peaks are 63.4°C and 335.6°C respectively. The austenitic finish temperature (A_f) resulted from the first and second endothermic peaks are 110°C and 390°C respectively. The austenite start temperature (A_s) is higher than 37°C. The austenite finish temperature (A_f) is unavoidable to be determined for an experimental investigation of pseudoelasticity. The area under the first endothermic peak gives the enthalpy of transition as 2.441 J/g, whereas area under the second endothermic peak gives the value of enthalpy of transition as 3.206 J/g. The peak temperature of the first endothermic peak is 84.2°C, whereas the peak temperature of second endothermic peak is 371.6°C; the changes in crystal structure occur at these peak temperatures. The peak associated with ά-martensite is smaller than that of ε-martensite. The peak is due to a change in magnetic properties of the material (the Curie transition). Certain materials lose their permanent magnetic properties above Curie temperature (T_C). The specific heat capacity (C_P) at first endothermic peak is found to be 0.615 J/g*K or 615 J/Kg*K, whereas specific heat capacity (C_P) at second endothermic peak is found to be 0.641 J/g*K or 641 J/Kg*K.

Besides, there is a cooling curve (green curve) in Fig. 5.2, which does not show any endothermic and/or exothermic peak. Cooling in this work has been performed by air not with liquid nitrogen as discussed before. It means, by heating the sample till 400°C followed by cooling from 400°C to 115°C results; (i) the material does not return to its martensitic phase by cooling till 115°C rather remains in austenitic phase or there is no reverse transformation (γ→ε or γ→ά) by cooling till 115°C, (ii) light green and green curves move parallel until cooling up to 175°C, after that cooling curve deviates from its path. The process of cooling has been stopped after the deviation of the cooling curve.

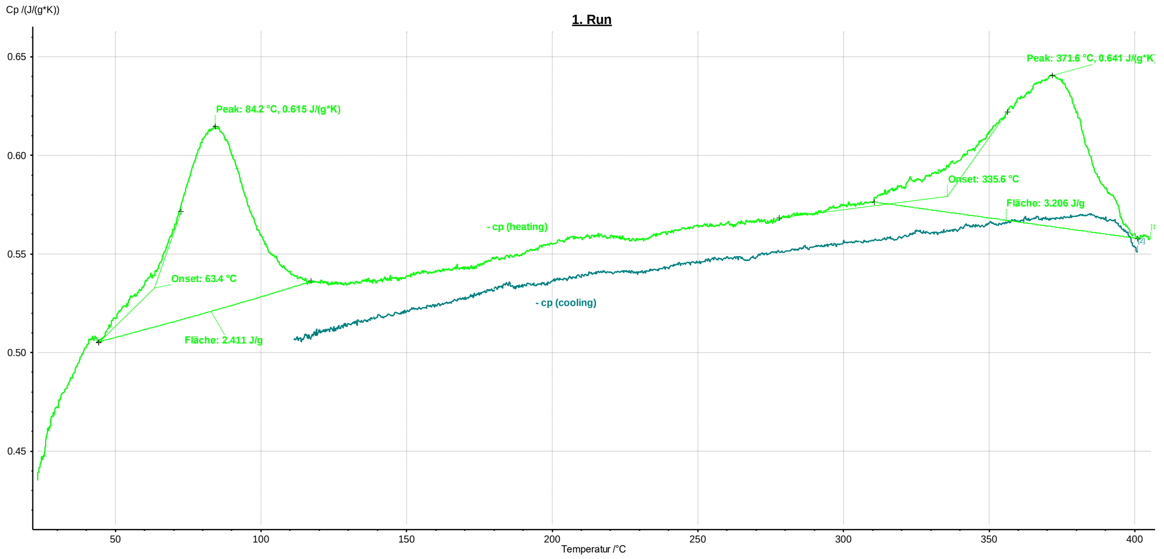

Fig. 5.2: Specific heat capacity over wide temperature range (C_P (T)) of first run of the specimen without any prior nitrogen dip

The above-mentioned results of first run of the specimen have been tabularized in Table 5.1.

Table 5.1
The DSC results obtained during all runs of the specimen of the investigated Fe-SMA

Results	**Symbol**	**First run**	**Second and Third run**	**Fourth run**
Phase transformation	-	Indicated	Not indicated	Indicated
Thermally induced phase transformation (endotherm1)	$(\varepsilon \rightarrow \gamma)$ transformation	63.4°C	Not indicated	60.6°C
Thermally induced phase transformation (endotherm2)	$(\acute{\alpha} \rightarrow \gamma)$ transformation	335.6°C	Not indicated	Not indicated
Austenitic start temperature (endotherm1)	A_s	63.4°C	-	60.6°C
Austenitic finish temperature (endotherm1)	A_f	110°C	-	100°C
Martensite start temperature	M_s	-	-	-
Martensite finish temperature	M_f	-	-	-
Enthalpy of transition (endotherm1)	ΔH	2.441 J/g	-	2.289 J/g
Enthalpy of transition (endotherm2)	ΔH	3.206 J/g	-	-
Austenitic start temperature (endotherm2)	A_s	335.6°C	-	-
Austenitic finish temperature (endotherm2)	A_f	390°C	-	-
Feasibility to be used inside the human body in terms of austenite start transformation temperature	-	No	-	No
Peak temperature (bigger peak of endotherm1)	-	82.2°C	-	79.5°C
Peak temperature (smaller peak of endotherm2)	-	371.6°C	-	-
Specific heat capacity (endotherm1)	C_P	0.615 J/g*K or 615 J/Kg*K	-	0.621 J/g*K or 621 J/Kg*K
Specific heat capacity (endotherm2)	C_P	0.641 J/g*K or 641 J/Kg*K	-	-
Dependence of specific heat on temperature	C_P (T)	Obtained	Obtained	Obtained
Reverse transformation by cooling till 115°C	$(\gamma \rightarrow \varepsilon)$ transformation and/or $(\gamma \rightarrow \acute{\alpha})$ transformation	No. The specimen has not been returned to martensitic phase while cooling from 400°C to 115°C during the first run OR in other words, there has not been any effect of cooling until 115°C on material's reverse transformation to martensite.	No. Austenitic phase has been confirmed before the start of second and third runs of the specimen because the specimen was not returned to martensitic phase while cooling from 400°C to 115°C during the first run OR in other words there has not been any effect of cooling until 115°C on material's	No. Austenitic phase has been confirmed before the start of fourth run of the specimen because the specimen was not returned to martensitic phase while cooling from 400°C to 115°C during first, second and third runs OR in other words there has not been any effect of cooling until 115°C on material's

			reverse transformation to martensite.	reverse transformation to martensite.

5.1.2 The results of second and third runs of the specimen without prior nitrogen dip

Fig. 5.3 shows DSC heating curve for the sample as well as for reference, and DSC cooling curve for the sample as well as for reference; during second run of the specimen. In Fig. 5.3, blue curve shows heating of the reference, then an isothermal vertical portion of the same curve comes, and after that brown curve shows cooling of the reference; these curves are exactly the same as complete green curve in Fig. 5.7. In Fig. 5.3, black curve shows heating of the sample, then an isothermal vertical portion of the same curve comes, and after that henna green curve shows cooling of the sample; these curves are exactly the same as complete blue curve in Fig. 5.7. By comparing brown and henna green cooling curves in Fig. 5.3, it has been found that both curves move parallel from 400°C to 175°C and after that sample cooling curve (henna green curve) deviates towards reference cooling curve (brown curve); which can be elaborated as that of Fig. 5.1.

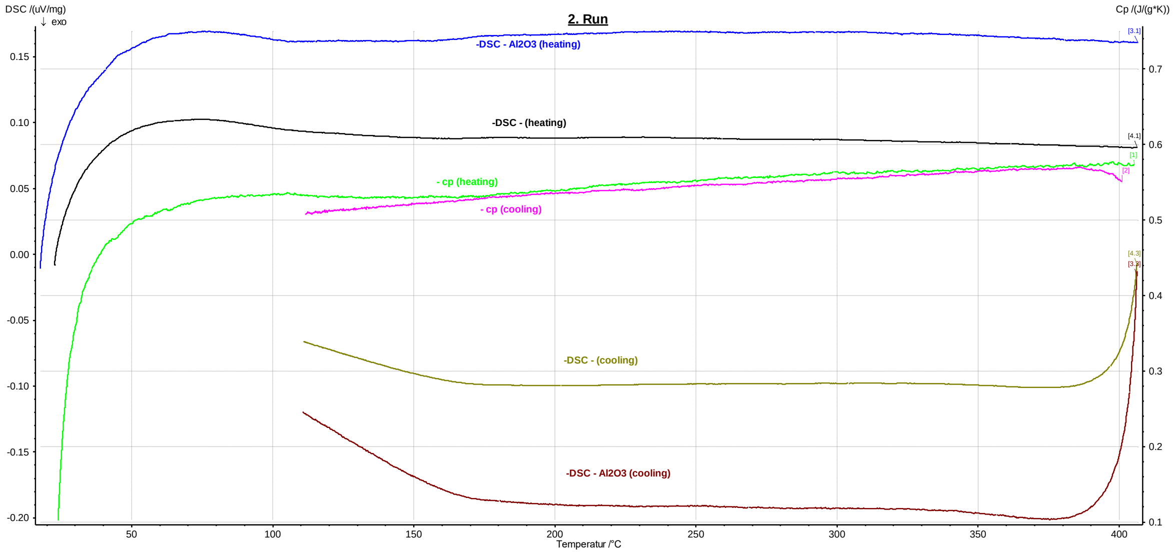

Fig. 5.3: Temperature Modulated DSC (TM-DSC) measurement of second run of the specimen without any prior nitrogen dip; compared with that of reference

The specific heat capacity (C_P) has now been calculated using Eq. 4.4 by means of the DSC results mentioned in Fig. 5.3. The light green curve Fig. 5.4, shows heating (C_P vs T) of the sample during second run of the specimen and pink curve shows normal air cooling (C_P vs T) of the sample. The specific heat capacity (C_P) at any temperature can be found out by the light green curve of Fig. 5.4, but there is no endothermic peak (i.e. no indication of phase transformation) during second run of the sample. It confirms that material was already in austenitic phase before starting the second run of the specimen and it was not returned to martensitic phase while cooling from 400°C to 115°C during first run of the specimen or in other words there has not been any effect of cooling until 115°C on material’s reverse transformation to martensite. Additionally, shown is a cooling curve (pink curve) in Fig. 5.4, which does not show any endothermic and/or exothermic peak too while cooling from 400°C to 115°C. It can be explained in a way as that of cooling curve (green curve) of Fig. 5.2. The third run of the specimen has also been performed and the results of third run are similar as that of second run showing that the material was already in austenitic phase before starting the third run and it was not returned to martensitic phase while cooling from 400°C to 115°C during both first and second runs of the second specimen.

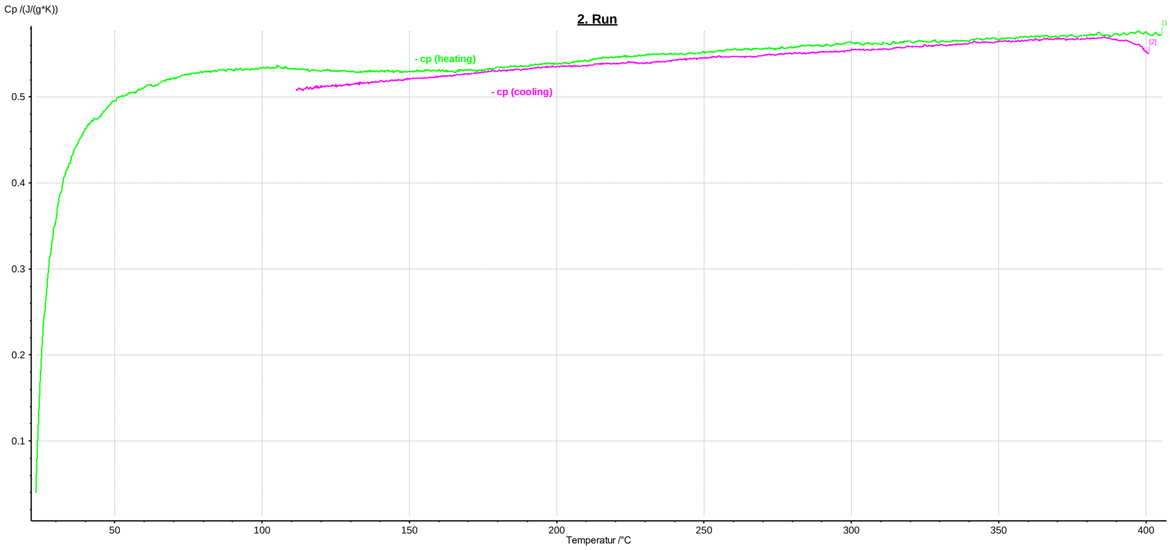

Fig. 5.4: Specific heat capacity over wide temperature range (C_P (T)) of second run of the specimen without any prior nitrogen dip

The above-mentioned results of second and third runs of the specimen have been tabularized in Table 5.1.

5.1.3 The results of fourth run of the specimen with prior nitrogen dip

During fourth run of the specimen, the transformation behavior has been examined in the quenched form i.e. DSC sample is dipped in liquid nitrogen before starting the measurement; in order to make it fully thermal martensite. Afterward, it has been heated in DSC to determine the specific heat capacity and thermally induced transformation behavior from martensite to austenite.

Fig. 5.5 shows DSC heating curve for the sample as well as for reference, and DSC cooling curve for the sample as well as for reference; during fourth run of the specimen. In Fig. 5.5, blue curve shows heating of reference, then an isothermal vertical portion of the same curve comes, and after that brown curve shows cooling of reference; these curves are exactly the same as complete green curve in Fig. 5.7. In Fig. 5.5, black curve shows heating of the sample, then an isothermal vertical portion of the same curve comes, and after that henna green curve shows cooling of the sample; these curves are exactly the same as a complete brown curve in Fig. 5.7. By comparing brown and henna green cooling curves in Fig. 5.5, it has been found that both curves move parallel from 400°C to 175°C and after that sample cooling curve (henna green curve) deviates towards reference cooling curve (brown curve) which can be discussed as that of Fig. 5.1.

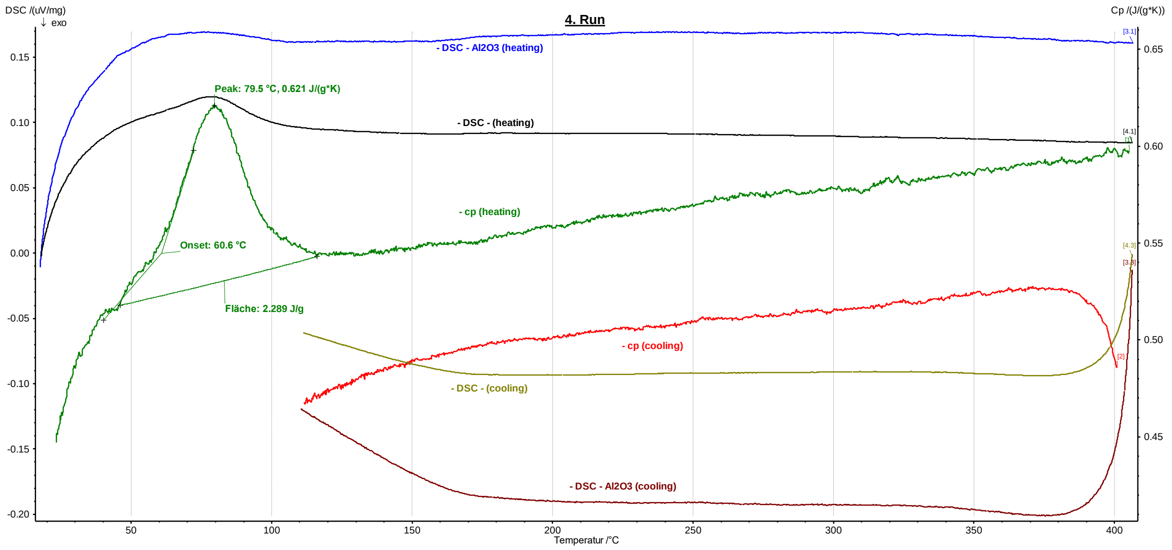

Fig. 5.5: Temperature Modulated DSC (TM-DSC) measurement of fourth run of the specimen by prior dipping in liquid nitrogen; compared with that of reference

The specific heat capacity (C_P) has now been calculated using Eq. 4.4 by means of the DSC results mentioned in Fig. 5.5. Fig. 5.6 shows, (i) the green curve which denotes heating (C_P vs T) of the sample whereas red curve shows normal air cooling (C_P vs T) of the sample during fourth run of the specimen over a range of temperatures between 20°C to 400°C with prior dipping in liquid nitrogen i.e. the sample has been brought below the martensitic finish temperature (M_f) with the help of liquid nitrogen, (ii) thermally induced phase transformation of Fe-SMA occurs only once at 60.6°C and this transition does not repeat itself like the previous case of first run, (iii) only one endothermic peak showing $\varepsilon \rightarrow \gamma$ thermally induced phase transformation is left whereas the second endothermic peak in this case showing $\acute{\alpha} \rightarrow \gamma$ thermally induced phase transformation has been disappeared. This ά-martensite phase was not an advantageous phase as per literature study. The existence of bcc crystal lattice structure denoting ά-martensite phase in the investigated Fe-SMA has been described earlier. Sawaguchi et al. showed that the alloys in Fe-Mn system possessing ά-martensite phases exhibit lower number of cycles to fatigue failure (N_f) [4]. Nikulin et al. indicated that ά-martensite is not beneficial for improving LCF resistance [9]. Tsuzaki et al. said that fatigue cracks have a tendency to be propagated through ά-martensite and it can accelerate the secondary cracking and zigzag crack path [69]. Consequently, the nitrogen dip prior to the measurement in this work has removed the disadvantageous ά-martensite phase from the investigated Fe-SMA, and (iv) the austenitic start temperature A_s and austenitic finish temperature A_f resulted from the obtained endothermic peak are 60.6°C and 100°C respectively. It has also been concluded that the investigated Fe-SMA is not suitable to be used inside the human body because its austenite start temperature (A_S) is higher than that of human body. The area under the endothermic peak gives the enthalpy of transition as 2.289 J/g. The peak temperature of the endothermic peak is 79.5°C on which there are changes in crystal structure and magnetic properties occur. The specific heat capacity (C_P) at the obtained endothermic peak is found to be 0.621 J/g*K or 621 J/Kg*K. The specific heat capacity of the investigated Fe-SMA over a range of temperatures (C_P (T)) can also be found out by Fig. 5.6, which is required to be used in Eq. 3.1 for the calculations of thermal conductivity over a range of temperatures (λ (T)) which decides the potential of a material for thermomechanical applications. Besides, the cooling curve (red curve) in Fig. 5.6 shows the cooling from 400°C to 115°C, it can be explained like that of cooling curve (green curve) of Fig. 5.2.

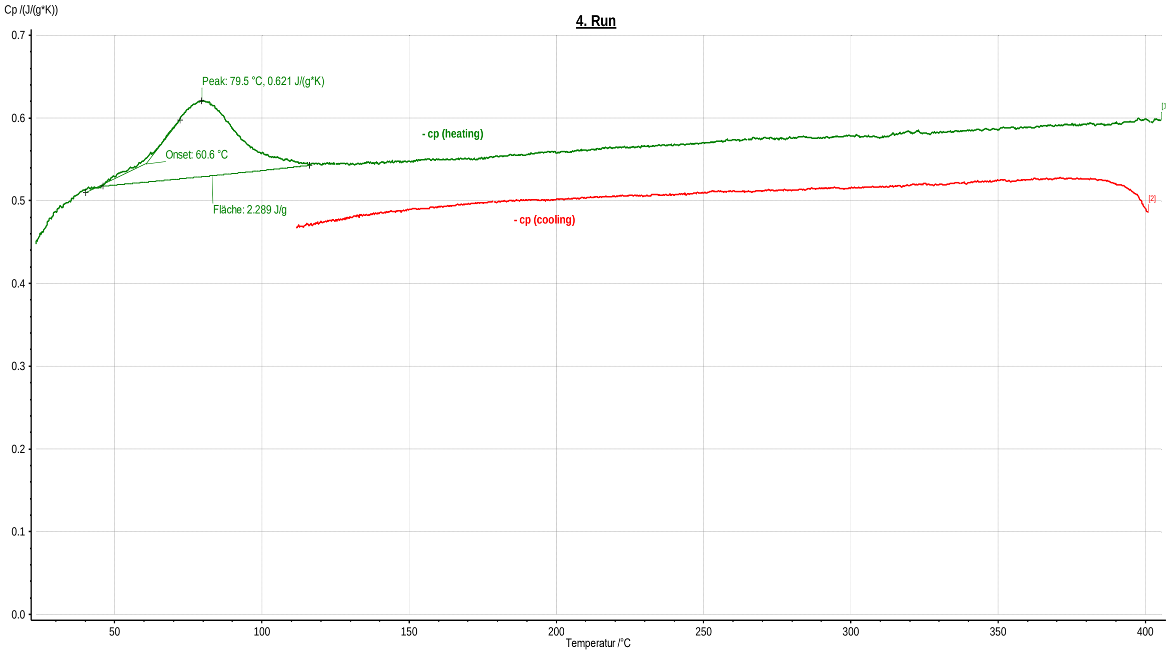

Fig. 5.6: Specific heat capacity over a wide temperature range (C_P (T)) of fourth run of the specimen by prior dipping in liquid nitrogen

The above-mentioned results of fourth run of the specimen have been tabularized in Table 5.1.

5.1.4 The combined runs of the specimen

The DSC results which have already been explained in above-mentioned subsection 5.1.1 to subsection 5.1.3, are combined in Fig. 5.7. The green curve in Fig. 5.7 shows DSC results of the reference, and the curves with other colors show run1 → run4 of the specimen from 20°C to 400°C. The first three runs i.e. run1 to run3 are without any prior nitrogen dip, but specimen has been cooled by dipping in liquid nitrogen before starting the fourth run as explained in the preceding subsections. There are significant differences between the results of reference and four runs of the sample, in the form of deviations. These deviations show the phase transformations. Unlike two endothermic peaks of the first run, there is only one endothermic peak obtained during the fourth run as shown in Fig. 5.7 as explained in subsection 5.1.3. It has been clearly observed from Fig. 5.7 that second endothermic peak disappears by making the alloy fully martensite prior to the measurement using nitrogen dip or in other words disadvantageous ά-martensite is removed from the material by prior nitrogen dip.

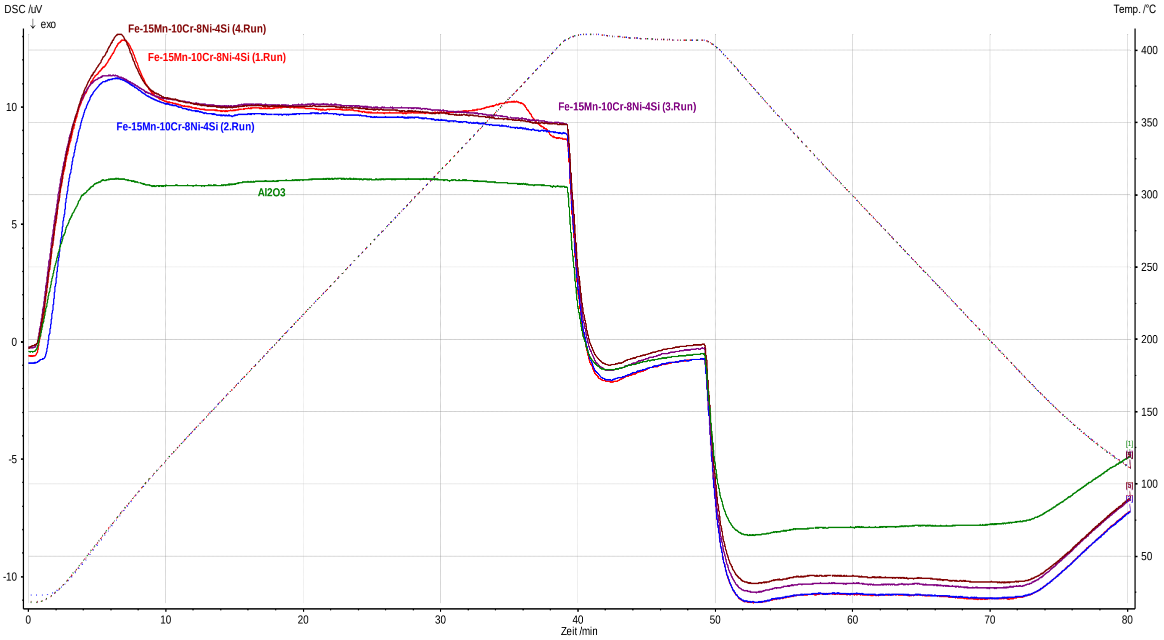

Fig. 5.7: Temperature Modulated DSC (TM-DSC) measurements of combined first, second, third and fourth run of the specimen; compared with that of reference

Table 5.2 shows the comparison of thermal properties which have been investigated in this work for Fe-SMA of interest with state-of-the-art SMAs and some well-known conventional materials e.g. Nitinol (typically composed of approximately 55 wt. % Nickel and 45 wt. % Titanium), stainless steel, 60-Nitinol (typically composed of approximately 60 wt. % Nickel and 40 wt. % Titanium), and two different Cu-SMAs due to unavailability of literature related to that of Fe-SMAs. It also shows that specific heat values of the investigated Fe-SMA are comparable with that of Nitinol.

Table 5.2 [63][108][110][111]
Comparison of parameters measured by DSC with that of known materials

Property	**Fe-15Mn-10Cr-8Ni-4Si SMA**	**Nitinol**	**CuZnAl**	**CuAlNi**	**Stainless steel 316L**	**60-Nitinol**
Specific heat	475-574 J/Kg.K	450-620 J/Kg°C or 490 J/Kg.K i.e. 490 J/Kg°C	390-400 J/Kg°C or 440 J/Kg.K i.e. 440 J/Kg°C	373-574 J/Kg°C or 390 J/Kg.K i.e. 390 J/Kg°C	500 J/Kg.K i.e. 500 J/Kg°C	453-504 J/Kg.K
Compatibility with the human body in terms of austenite start transformation temperature	Poor	Very good	Poor	Poor	Very good	-

5.1.5 Microstructure prior to thermal and mechanical investigations

The shape memory alloys are very sensitive to the exact composition, microstructure, grain size, processing & heat treatment and loading conditions [57]. Microstructure is the arrangement of phases on microscopic level; therefore, it can be observed by a microscope. The microstructure of the material and its chemical composition strongly effect the physical properties like toughness, ductility, strength, hardness, corrosion resistance, wear resistance etc. The purpose of the current study is to provide a detailed information of the microstructure before and particularly after deformation.

The results have been obtained by scanning electron microscopic (SEM) analysis. Typical SEM microstructure formed in the surface of investigated Fe-SMA prior to deformation without any type of heat treatment is shown in Fig. 5.8. The selected alloy used in this work is produced by arc melting. Two phases have been detected by this analysis in the investigated Fe-SMA at room temperature; (i) grey color phase shows face-centered cubic (fcc) crystal lattice structure which denotes γ-austenite phase, and (ii) white color phase shows body-centered cubic (bcc) crystal lattice structure which denotes α-ferrite phase which causes magnetic properties and classic example of ferromagnetic material, it is also called as ά-martensite phase (bcc) or ά-phase (bcc) as per literature debate and considered to be non-advantageous phase.

Nikulin et al. observed the average austenitic grain size of 92µm for investigated Fe-SMA. Nikulin et al., Jun et al. and Sadeghpour et al. observed that the effect of grain size can be neglected if it is higher than 40 µm. Less than 40 µm grain size produces a considerable effect on deformation mechanism of the high manganese ferrous alloys. The cross-slipping and climbing of perfect dislocations have been observed [9][112][113].

A dislocation structure containing planar pileups with long stacking faults has also been observed but it is difficult to say where they came from, whether grinding or polishing or from the addition of any element in the alloy. The morphologies of investigated Fe-SMA have been observed using Philips XL30 Environmental Scanning Electron Microscope (ESEM).

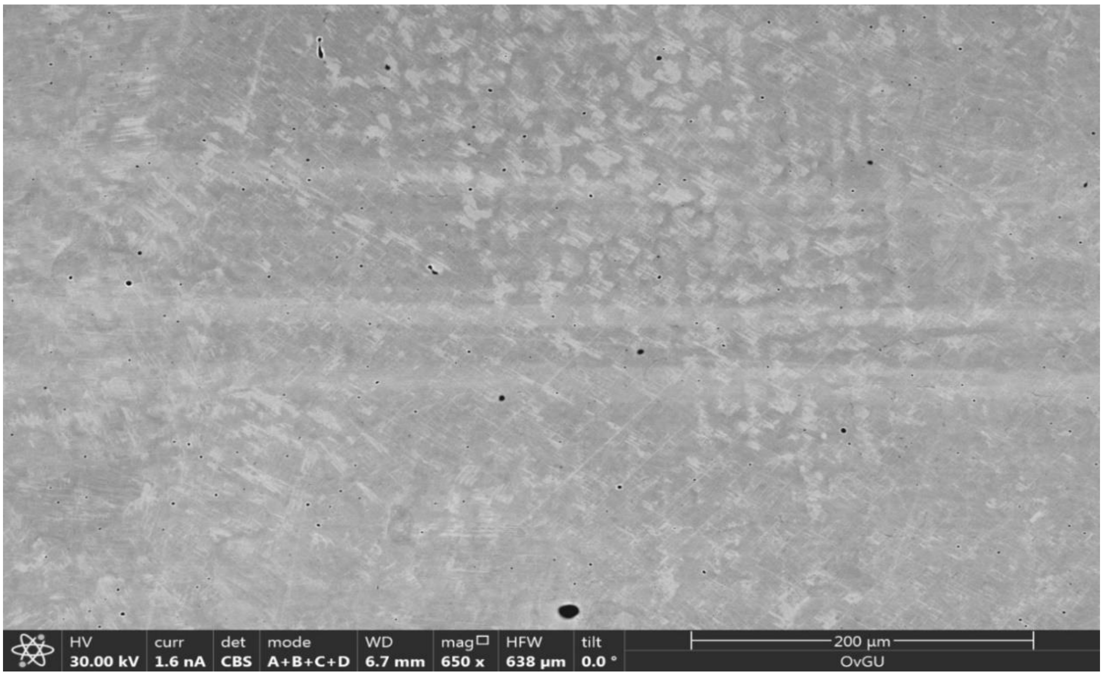

Fig. 5.8: SEM microstructure prior to deformation

5.1.6 Chemical composition of the investigated Fe-SMA

The scanning electron microscope has also been equipped with EDAX Energy Dispersive Spectroscopy (EDS) system for chemical composition analysis of the investigated Fe-SMA. This scanning electron microscope and energy dispersive spectroscopy (SEM-EDS) are available at IWF, OvGU Magdeburg, Germany.

Qualitative analysis in chemistry is the determination of chemical composition of a sample, it tells which elements are present in a sample, however it does not provide the information about their quantity. The alloy surface has qualitatively been analyzed to comprise of the Fe, Mn, Cr, Ni, and Si elements by SEM-EDS as shown in Fig. 5.9.

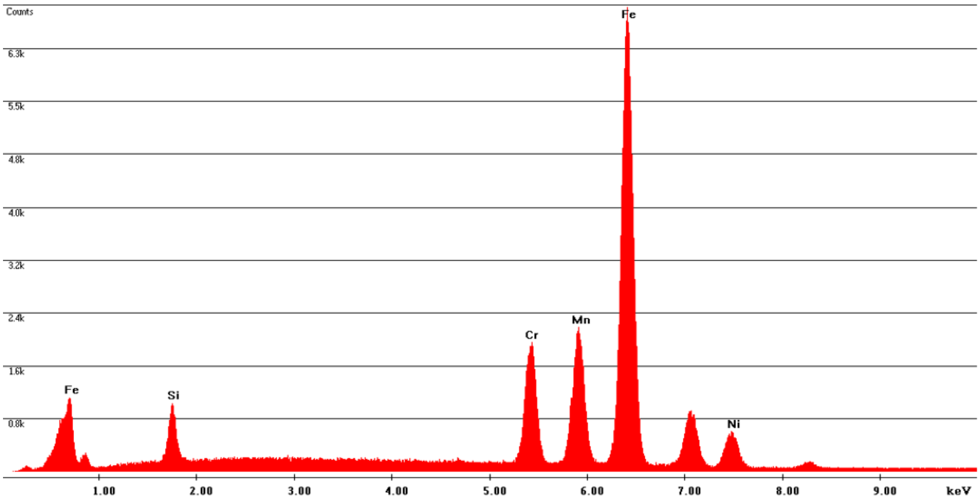

Fig. 5.9: SEM-EDS qualitative analysis of alloy surface

The quantitative analysis provides the information about the quantity of elements present in a sample. The alloy surface has quantitatively been analyzed showing the chemical composition measured by SEM-EDS as shown in Table 5.3. The theoretical values of different elements are also described in Table 5.3.

Table 5.3
The SEM-EDS quantitative analysis at the normal surface of the investigated Fe-SMA in weight percentage (wt. %)

Sr. #	**Elements**	**Theoretical Chemical Composition (wt. %)**	**SEM-EDS Chemical Composition (wt. %)**
1	Fe (wt. %)	63	62.85
2	Mn (wt. %)	15	14.63
3	Cr (wt. %)	10	10.43
4	Ni (wt. %)	8	7.89
5	Si (wt. %)	4	4.2

Micropores have also been found at the top of alloy button while analyzing with an optical microscope as well as with scanning electron microscope. The presence of micropores and little porosity at top of the sample is usual which cannot be avoided. The alloy surface at pore has qualitatively been analyzed by SEM-EDS to comprise of the Fe, Mn, Cr, Ni, Si, S and Se elements as shown in Fig. 5.10, where S (Sulpher) and Se (Selenium) are impurities. It is proposed in the literature that impurities are purposely, accidentally, inevitably, and/or incidentally added or these impurities may be present from the beginning.

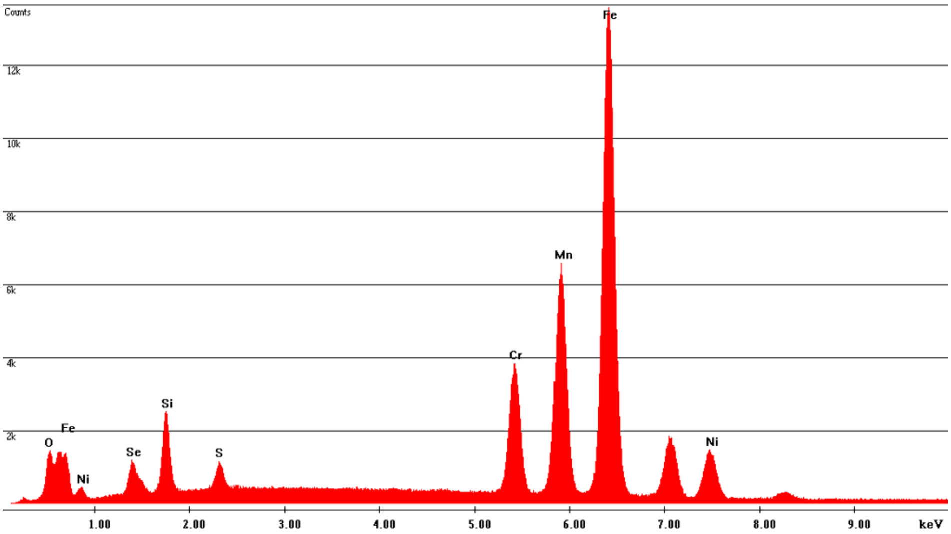

Fig. 5.10: SEM-EDS qualitative analysis at the pore

5.1.7 Phase identification of the investigated Fe-SMA

The knowledge of accurate molecular structure is a prerequisite for understanding and predicting the chemistry of the whole molecule, material design and for structure-based functional studies. X-rays diffraction (XRD) is a technique primarily used for phase identification of a crystalline material and can provide information on unit cell dimensions. The basic principle of XRD analysis is based on Bragg's Law in which X-rays generated by X-rays tube are diffracted from a crystal lattice and the following Eq. 5.1 is used for the required measurements,

$$2d.\sin\theta = n.\lambda \tag{5.1}$$

where,

n = order of diffraction OR an integer for peak order
λ = wavelength of incident X-ray
d_{hkl} = inter-planar spacing of the hkl planes in the crystal lattice
θ = diffraction angle or Bragg's angle i.e. angle between incoming X-ray and the surface it is hitting

Besides, d is the distance of the lattice plane, it is the only unknown quantity in the above-mentioned Eq. 5.1. The value of λ (wavelength of incident X-ray) found from the results of this work is $\lambda_{\mathrm{Cuk}\alpha 1}$ = 1.540598Å where Å is an abbreviation of Angstrom which is an internationally recognized unit of length and 1Å = 1x10^{-10} m (1Å = 0.1 nm), it is widely used unit to express the dimensions of atoms, molecules, and electromagnetic wavelengths.

Suppose n = 1, the obtained λ is 1.540598Å, and 2θ is 30 then d can be calculated by the relation 2 (d) sin (30/2) = (1) (1.540598Å). Hence, d = 2.9762Å. Suppose n = 1, λ is 1.540598Å, and d is 3Å then 2θ can be calculated by the relation 2 (3) sin θ = (1) (1.540598). Therefore, θ =

14.88° and 2θ will of course be 2θ = 2 x 14.88° = 29.76°.

The XRD results of the investigated Fe-SMA prior to deformation are shown in Fig. 5.11. X-rays tube which is located inside the diffractometer is made of Copper, therefore, Cu is in Fig. 5.11. There is an intensity of X-rays (I) on y-axis of Fig. 5.11 in counts per second (cps). High intensity for higher peak and lower intensity for lower peak.

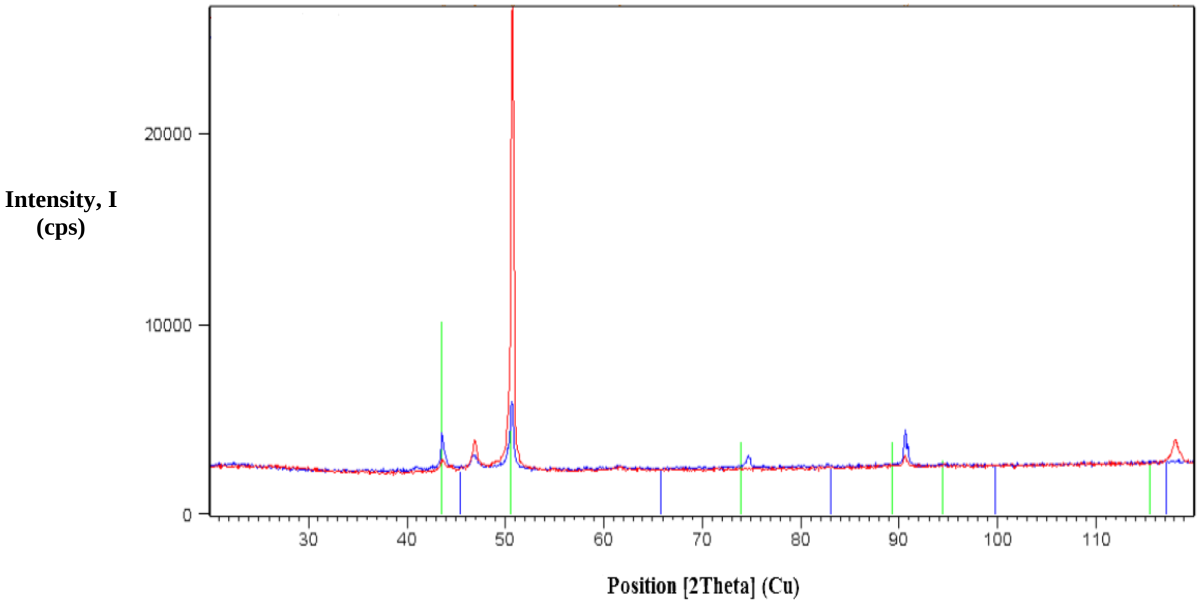

Fig. 5.11: XRD results of the investigated Fe-SMA

The above-mentioned Fig. 5.11 illustrates the following results,

- Red peaks in Fig. 5.11 correspond to green vertical lines of Fig. 5.12 which indicate the face-centered cubic (fcc) crystal lattice structure denoting γ-austenitic phase. It is consistent with Sawaguchi et al. [4] that fcc γ-austenite Fe-Mn-Si based alloys are known to show a shape memory effect associated with the deformation-induced martensitic transformation from face-centered cubic γ-austenite to hexagonal close-packed ε-martensite on loading and its reversion on subsequent heating; such type of alloys are austenitic before deformation except for those having lower Mn concentrations, which exhibit a body-centered cubic (bcc) α-ferrite.

- Blue peaks in Fig. 5.11 correspond to blue vertical lines of Fig. 5.13 which indicate the body-centered cubic (bcc) crystal lattice structure denoting α-ferrite phase, which implies that this phase also exists in the material causing magnetic properties and classic example of ferromagnetic material. Sawaguchi et al. [4] said that this is actually ά-martensite phase (bcc) which also exists before deformation and it should be noted that the alloys possessing ά-martensite phases exhibit lower number of cycles to fatigue failure (N_f) values.

- The largest red peak in Fig. 5.11 corresponding to green vertical line implies that γ-austenitic phase does mainly exist in the material.

- Several lattice planes obtained for the investigated Fe-SMA at different values of 2θ are stated in Table 5.4 and Table 5.5 in terms of Miller Indices i.e. h, k, and l.

The above-mentioned results have been obtained by comparative study of XRD results of investigated Fe-SMA with that of standard iron (Fe) charts and tables shown in Fig. 5.12, Fig. 5.13, Table 5.4, and Table 5.5.

There are two phases in the investigated Fe-SMA as described above but it not possible to calculate the ratio between these two phases as the specimen is with texture. The XRD analysis requires fine grains (20 microns) and statistical orientation (without texture) in the sample. Due to unavailability of fine grains and statistical orientation (availability of crystal structure and texture) in the sample, it is not possible to calculate that ratio. For exact results the specimen should be without texture or with known texture. If the crystals in the specimen are oriented in different directions, then it is possible that there is no texture. If the crystals are oriented in any preferred direction, then it is possible that there is texture. Therefore, the crystals should be oriented in all directions instead of any preferred direction. If the crystals are in any preferred direction and this texture is known then experiments can be performed to bring them in all directions, but if the texture is not known then it is not possible to bring them in all directions. If for example the crystals are oriented only in one direction, it is possible that a peak which is in another direction disappears and the sample has to be moved in order to make it visible.

The red as well as blue peaks of the specimen in Fig. 5.11 are slightly shifted from the green fcc iron pattern and blue bcc iron pattern respectively. Therefore, the standard XRD diagram is not obtained. The shifting of peaks is the problem that the investigated Fe-SMA is not purely iron, there are also some additional elements like Mn, Si, Cr and Ni present in the investigated Fe-SMA. But the results are being compared with the data bank of pure iron. Consequently, the lattice planes and the distances between lattice planes are also slightly different.

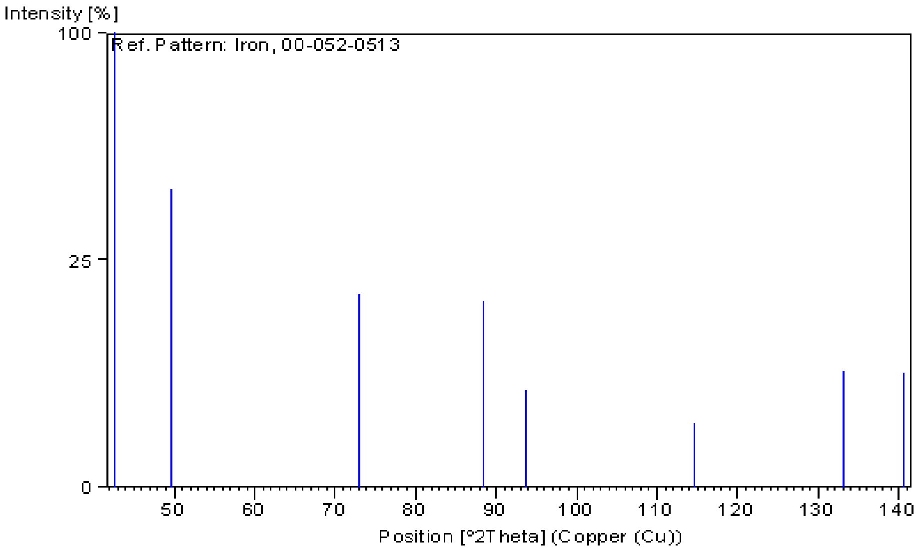

Fig. 5.12: Stick pattern corresponding to green vertical lines of Fig. 5.11; indicating fcc iron (ovgu)

The values of Miller Indices i.e. h, k, and l denoting different lattice planes for fcc iron at different values of 2θ are stated in Table 5.4. The values of Table 5.4 have been obtained from Fig. 5.12 which is consistent with the results for the investigated Fe-SMA. There are additional elements too in the investigated Fe-SMA along with Fe, therefore, it is hard to say that these are the lattice planes for fcc phase of investigated Fe-SMA. However, the lattice planes for fcc phase of investigated Fe-SMA are close to the lattice planes mentioned over here.

Table 5.4 (ovgu)
Lattice planes corresponding to red peaks and green vertical lines of Fig. 5.11 (fcc iron)

Sr. #	**h**	**k**	**l**	**d (A)**	**2Theta (deg)**	**I (%)**
1	1	1	1	2.11304	42.759	100.0
2	2	0	0	1.82995	49.788	42.8
3	2	2	0	1.29397	73.068	17.9
4	3	1	1	1.10350	88.542	16.8
5	2	2	2	1.05652	93.621	4.6
6	4	0	0	0.91497	114.679	2.0
7	3	3	1	0.83964	133.103	6.6
8	4	2	0	0.81838	140.525	6.3

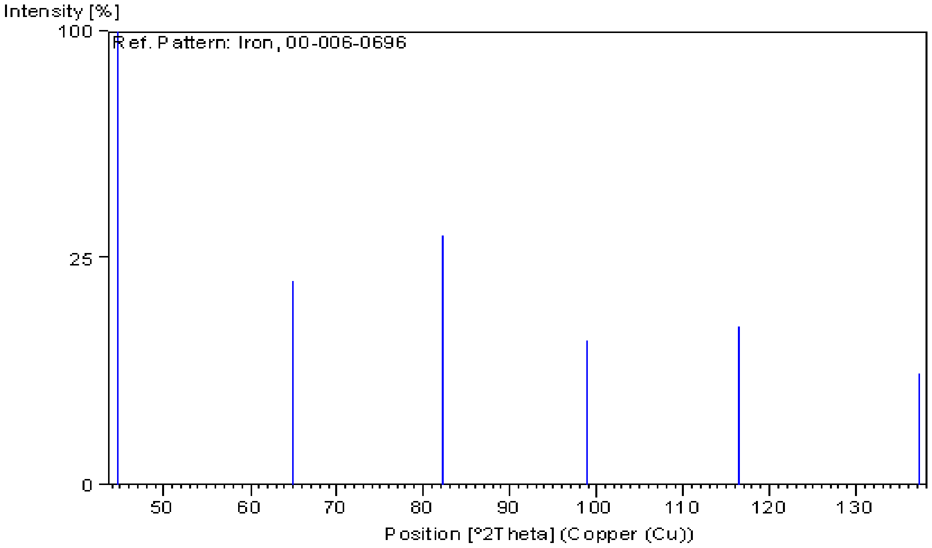

Fig. 5.13: Stick pattern corresponding to blue vertical lines of Fig. 5.11; indicating bcc iron (ovgu)

The values of Miller Indices i.e. h, k, and l denoting different lattice planes for bcc iron at different values of 2θ are stated in Table 5.5. The values of Table 5.5 have been obtained from Fig. 5.13 which is consistent with the results for the investigated Fe-SMA. There are additional elements too in the investigated Fe-SMA along with Fe, therefore, it is hard to say that these are the lattice planes for bcc phase of investigated Fe-SMA. However, the lattice planes for bcc phase of investigated Fe-SMA are close to the lattice planes mentioned over here.

Table 5.5 (ovgu)
Lattice planes corresponding to blue peaks and blue vertical lines of Fig. 5.11 (bcc iron)

Sr. #	**h**	**k**	**l**	**d (A)**	**2Theta (deg)**	**I (%)**
1	1	1	0	2.02680	44.674	100.0
2	2	0	0	1.43320	65.023	20.0
3	2	1	1	1.17020	82.335	30.0
4	2	2	0	1.01340	98.949	10.0
5	3	1	0	0.90640	116.390	12.0
6	2	2	2	0.82750	137.144	6.0

5.2 Dimensional changes of the investigated Fe-SMA over a range of temperatures

The precise knowledge of dimensional changes of material is crucial for the products which are in contact while heating applications to avoid stresses and possible cracking. Some findings are directly investigated by dilatometer and the rest are calculated using the dilatometry results. These findings are very significant due to ever-increasing quantity of materials which can be used in high-temperature applications as well as very important in engineering design and application success. Table 5.6 shows the preliminary conditions at which dilatometry measurement of the investigated Fe-SMA is performed. The reference temperature is the temperature of laboratory where the experiments have been performed, it remains constant inside the laboratory at a value of 20°C. It can also be called room temperature. Experiments have been performed under pure inert argon gas atmosphere.

Table 5.6
Preliminary conditions for experimental work

Sr. #	General information during experimental work	Reference	Sample
1	Material	Al_2O_3	Fe-15Mn-10Cr-8Ni-4Si SMA
2	Instrument	Netzsch DIL 402 C	Netzsch DIL 402 C
3	Sample	A rod-shaped specimen of Al_2O_3	A rod-shaped specimen of Fe-15Mn-10Cr-8Ni-4Si SMA
4	Specimen length	25 mm	25.073 mm
5	Measuring mode	Standard expansion	Standard expansion
6	Pure gas	Pure argon gas	Pure argon gas
7	Flow rate	75 ml/min	75 ml/min
8	Temperature range	20°C to 400°C	20°C to 400°C
9	Heating rate	5 K/min	5 K/min
10	Reference temperature (Lab or Room temperature)	20°C	20°C

Arc melting process has been found to be suitable to produce a 25g button of the investigated Fe-SMA as discussed in the preceding chapter. The quantity of different elements in 25g button is given in Table 5.7.

Table 5.7
The quantity of different elements in 25g button of investigated Fe-SMA used in dilatometry measurement

Quantity of elements	Fe	Mn	Cr	Ni	Si
Theoretical	15.75g	3.75g	2.5g	2g	1g
Actual	15.7488g	3.7492g	2.4976g	2.013g	1.0171g

5.2.1 Density of the investigated Fe-SMA over a range of temperatures

Dilatometer measures the density of material and its dependence upon temperature. The results have been obtained in the form of excel data which shows the values of material density with respect to different temperatures between the temperature range of 20°C to 400°C during dilatometry measurement of the investigated Fe-SMA. This excel data has been plotted as density-temperature diagram as shown in Fig. 5.14.

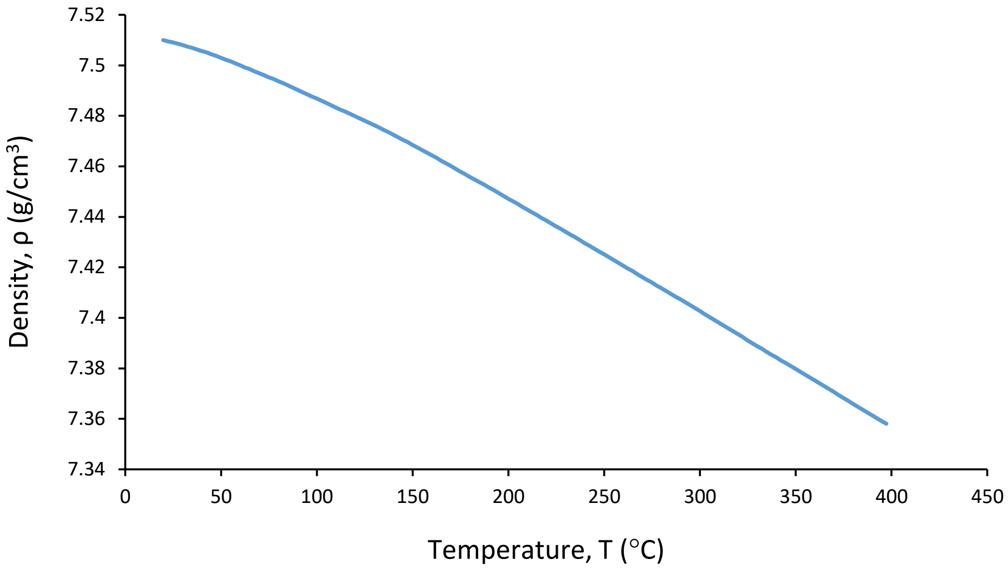

Fig. 5.14: Density-temperature diagram for the investigated Fe-SMA

W. Huang [57] said that specific actuation stress (= stress/density) is considered instead of actuation stress in case of a lightweight actuator.

This density of the investigated Fe-SMA over a range of temperatures (ρ (T)) found out by dilatometry measurement is required to be used in Eq. 3.1 for the calculations of thermal conductivity over a range of temperatures (λ (T)) which decides the potential of any material for thermomechanical applications. Besides, Table 5.10 shows that density values of the investigated Fe-SMA are comparable with that of Nitinol.

5.2.2 Dilatation of the investigated Fe-SMA over a range of temperatures

The dilatometer also heats-up the sample and measures how much the sample expands with

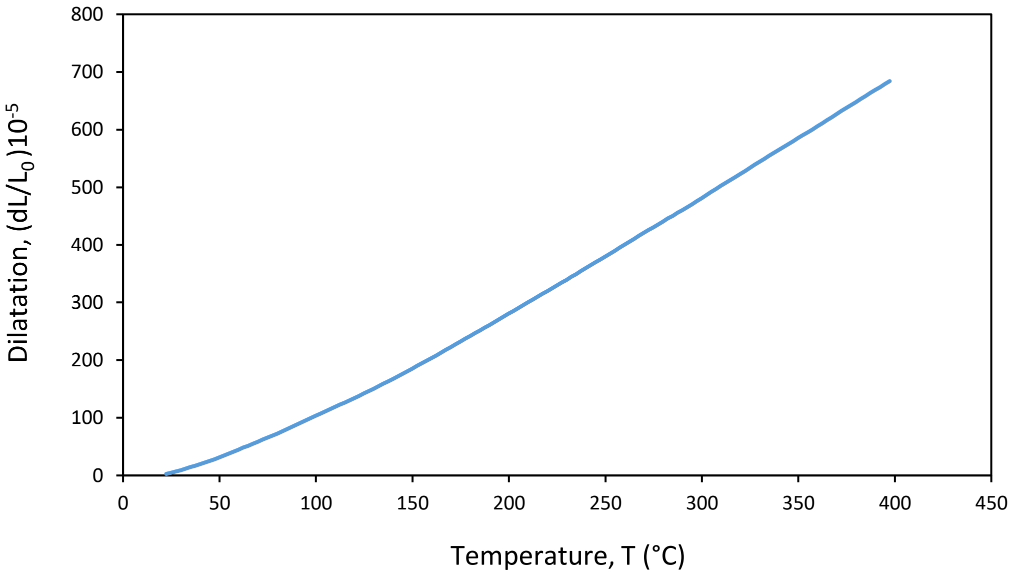

Fig. 5.15: Dilatation-temperature diagram for investigated Fe-SMA during heating in dilatometer; showing relative change in length of a specimen during heating

temperature which is called as longitudinal expansion or change in length denoted by dL. Dilatation is defined as the longitudinal expansion or change in length (by temperature or any other state variable) divided by initial length denoted by dL/L_0. The results have been obtained in the form of excel data which also shows the dilatation over a range of temperatures between the temperature range of 20°C to 400°C during dilatometry measurement of the investigated Fe-SMA. This data has been plotted as dilatation-temperature diagram as shown in Fig. 5.15.

Such type of data is beneficial to calculate the coefficient of thermal expansion (CTE) which is very useful parameter for design engineers to design against failure by thermal stresses and this expansion characteristic is important for application success.

Van Caenegem et al. [114] investigated the shape memory behavior of each of Fe29Mn7Si (mass %) and Fe29Mn7Si5Cr (mass %) alloys. The shape recovery has been quantified using dilatometry experiments on already compressed samples as shown in Fig. 5.16. The recovery strain ε_{rec} and shape recovery ratio η; have been measured by dilatometry as mentioned in Table 5.8. The shape recovery ratio η has been calculated as the change in length during heating in dilatometer (L_1-L_2) which has been measured from dilatation curve, divided by change in length while compression/deformation (L_1-L_o). The data of Table 5.8 shows that higher the value of pre-strain lower the shape recovery ratio. The recovery stresses have been measured using the designed procedure, which is caused by the change of dimensions due to the shape memory effect. The recovery stress is that stress which is generated when the recovery of deformation is hindered under constraint.

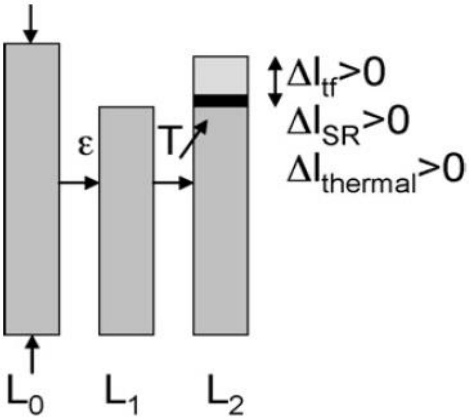

Fig. 5.16: Shape recovery after compression by dilatometry [114]

Table 5.8 [114]
Recovery strain ε_{rec} and shape recovery ratio η

Sr. #	**Alloys**	**Pre-strain**	**ε_{rec} = (L_1-L_2)/L_1**	**η = (L_1-L_2)/(L_1-L_o)**
1	Fe29Mn7Si (mass %)	1.6	0.67	41
2		3.6	1.28	34
3		8.1	1.85	21
4		17.5	1.72	8
5	Fe29Mn7Si5Cr (mass %)	1.8	0.52	28.4
6		3.4	1.44	41
7		7.9	1.75	20
8		17.6	1.64	8

In applications like pipe couplings, the stainless SMAs replace more expensive Nitinol because their remarkable shape recovery upon pseudoplastic deformation is about 3 to 4%. Otubo et al.

proved the existence of better shape recovery in Fe-Mn-Si-Cr-Ni-C SMA alloy without Co instead of that with Co, shown by 80% shape recovery upon 4% tensile strain and 65% recovery for the same tensile strain [115]. The recently developed Fe-17Mn-5Si-10Cr-4Ni-1(V, C) SMA is found to be suitable for civil and mechanical engineering applications because it has high strength, ductility and recovery stress. The most important application of FeMnSi-SMAs is to use their recovery stress for pre-stressing of structural elements such as concrete and metallic beams and plates to increase their performance.

However, the first step ($L_o \rightarrow L_1$) shown in Fig. 5.16 consisting of pre-straining through compression; has not been performed in this work because the available arc melting machine has been designed for melting the samples up to 20g only. A 25g button (which is above the capacity of the machine) has been prepared by arc melting machine, it has been used to prepare a maximum of 25mm long specimen. Heavier than 25g button is not possible to be prepared at all by using arc melting machine, consequently, longer than 25mm specimen is also not possible to be prepared from available facilities. The specimen having less than 25mm length does not fit inside the dilatometer. Also, it is not possible to get 25mm length after performing the first step consisting of pre-straining by compression. Hence, in this work 25mm long specimen is directly heated in the dilatometer.

5.2.3 Phase Transition in the investigated Fe-SMA

The phase transition in investigated Fe-SMA has been investigated by means of dilatometry too over a range of temperatures while analyzing the data obtained from dilatometry measurement. The dilatometer heats-up the sample and measures how much the sample expands with temperature; which is used to investigate the phase transition in the material. The data of the change in length of a specimen during different temperature intervals has been obtained from the data of Fig. 5.15; this obtained data is described in Table 5.9.

Table 5.9
Change in length of the specimen during different temperature intervals during dilatometry measurement

Sr. #	**Temperature intervals (°C)**	**Change in length of a specimen during different temperature intervals x10^{-5}**
1	32 to 52	336.3
2	52 to 72	138
3	72 to 92	299
4	92 to 112	309
5	112 to 132	320
6	132 to 152	350
7	152 to 172	380
8	172 to 192	380
9	192 to 212	390
10	212 to 232	390
11	232 to 252	410
12	252 to 272	410
13	272 to 292	400
14	292 to 312	410
15	312 to 332	420
16	332 to 352	410
17	352 to 372	420
18	372.346 to 392.346	420

The obtained data of Table 5.9 has been plotted as Fig. 5.17 and Fig. 5.18 which show the occurrence of martensite to austenite phase transition during the temperature interval of 52°C to 72°C because there is a substantial decrease during this temperature interval presenting drastic change in length of the specimen during the said interval.

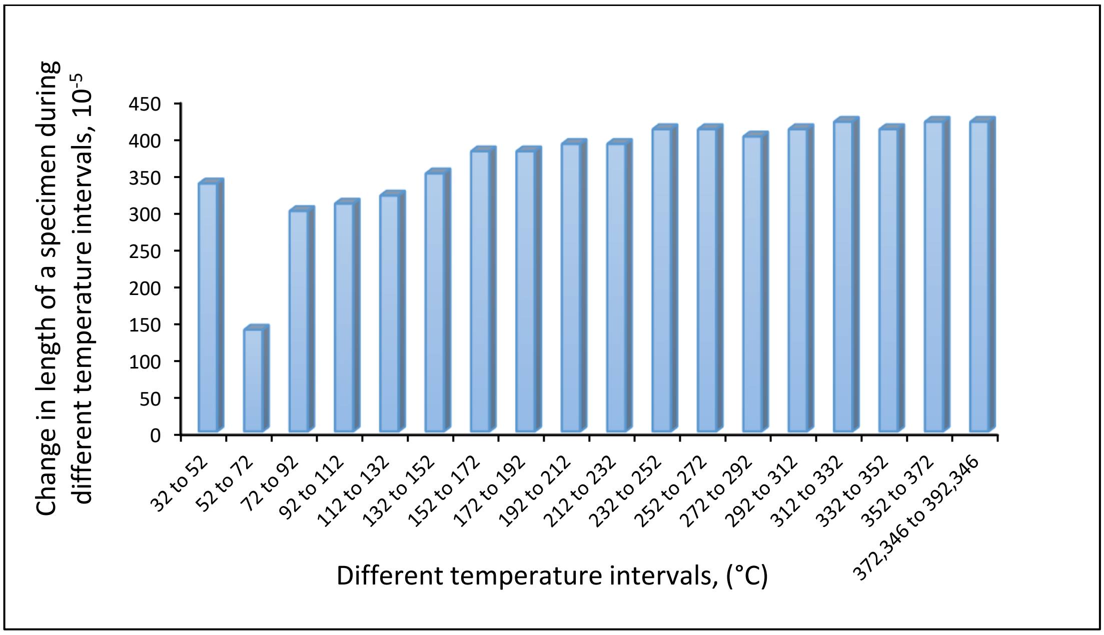

Fig. 5.17: Change in length of the specimen during different temperature intervals showing a phase transition

By analyzing the dilatometry curve in Fig. 5.15 it has been noted that the curve deviated to a small extent between 40°C to 100°C after that it became straight, however, it was difficult to locate the exact temperature interval possessing the phase transition. Therefore, Fig. 5.17 and Fig. 5.18 have been drawn.

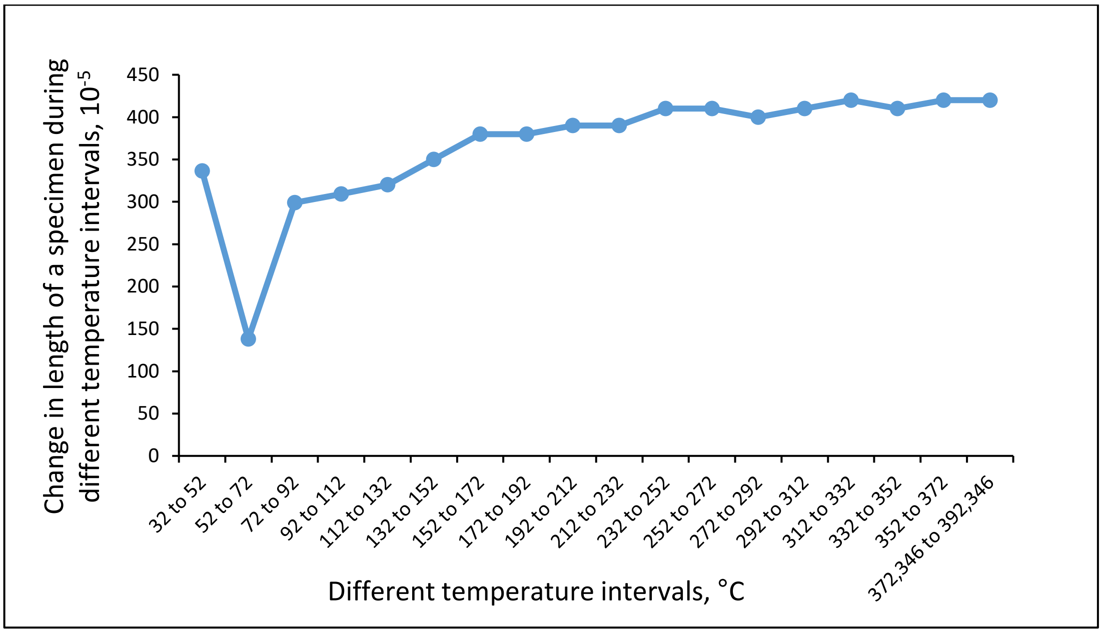

Fig. 5.18: Change in length of the specimen during different temperature intervals showing a phase transition

The austenitic start temperature (A_S) investigated in subsection 5.1.3 is 60.6°C which confirms the existence of martensite to austenite phase transformation between 52°C to 72°C. The discussion on the importance of investigation of austenitic start temperature has already been performed in subsection 5.1.3. The author has published the results of subsection 5.2.3 in a Journal having high impact factor [116].

5.2.4 Coefficient of thermal expansion calculations for the investigated Fe-SMA

The coefficient of linear thermal expansion (CTE) denoted by α is the material property which indicates the extent to which a material expands upon heating. It is defined as the change in length of a material per unit change in temperature.

M. K. Stanford [108] used the well-known relation of Eq. 5.2 for CTE calculations.

CTE has been calculated in this work for the investigated Fe-SMA over a range of temperatures while analyzing the data obtained from dilatometry measurement. It has been calculated by means of Eq. 5.2 using the dilatometry results. Eq. 5.2 shows that CTE is calculated by a change in length divided by initial length multiplied by the change of temperature or by measuring the relative change in length of the specimen with respect to temperature. CTE has SI unit of $(°C)^{-1}$ or 1/°C and U.S. customary unit of $(°F)^{-1}$ or 1/°F.

$$\alpha = (dL/L_o) / (T - T_o) \qquad (5.2)$$

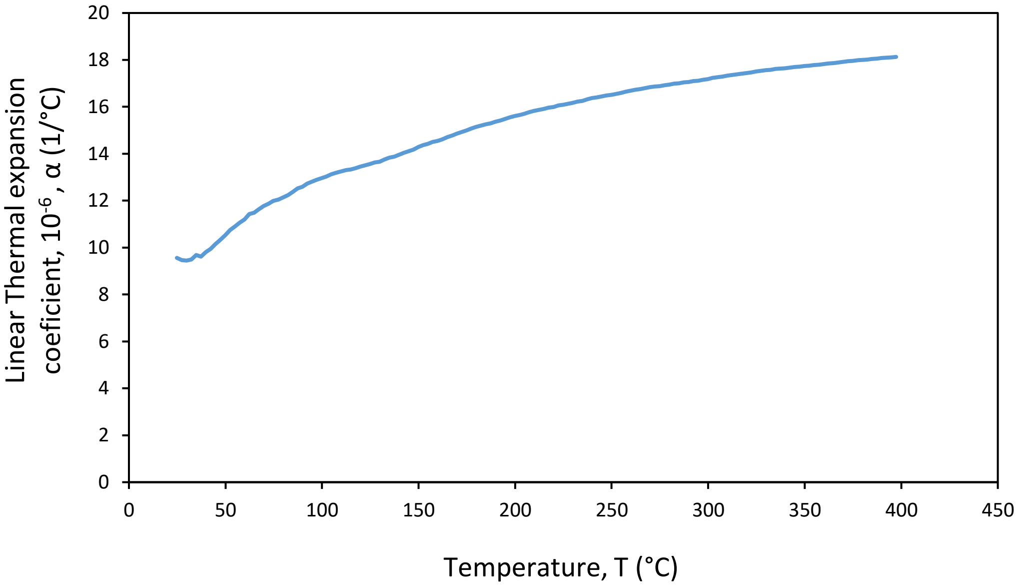

Fig. 5.19: Thermal expansion coefficient-temperature diagram for investigated Fe-SMA

where,

α coefficient of thermal expansion $(°C)^{-1}$
L_o initial sample length (25.073 mm)
T test temperature of the sample (obtained from dilatometry results)
T_o initial temperature "20°C"
dL/L_o the change in length per initial length (obtained from dilatometry results)

After calculating the CTE, the results have been plotted as thermal expansion coefficient-temperature diagram shown in Fig. 5.19.

Khairul Alam et al. [106] said that Invar 36 is useful for aerospace applications because it has a very low value of CTE which means it exhibits very small changes in physical dimensions over a range of temperatures.

Such type of calculation is important because some materials have very high variations with temperature. It is also used for design purposes to determine if failure by thermal stress may occur therefore design engineers have a considerable interest in CTE values. The expansion of the material is vital to be considered while designing large structures, beams, molds for casting hot materials, and in other engineering applications where substantial changes in dimension are expected due to temperature. The fitting parts over one another is the mechanical application of thermal expansion e.g. inner diameter of the bushing is kept slightly smaller than that of shaft in order to fit it on the shaft; then it is heated, brought over the shaft and let it be cooled to achieve shrink fit.

Table 5.10 shows the comparison of density and thermal expansion coefficient which have been investigated in this work for investigated Fe-SMA with state-of-the-art SMAs and some well-known conventional materials e.g. Nitinol, stainless steel, 60-Nitinol, and two different Cu-SMAs. It also shows that thermal expansion coefficient of the investigated Fe-SMA is in the range as that of Nitinol.

Table 5.10 [63][108][110][111]
Comparison of density and the thermal expansion coefficient of investigated Fe-SMA with that of well-known materials

Property	**Fe-15Mn-10Cr-8Ni-4Si SMA**	**Nitinol**	**CuZnAl**	**CuAlNi**	**Stainless steel 316L**	**60-Nitinol**
Density	7509-7358 Kg/m^3	6400-6500 Kg/m^3 or 6.45 g/cm^3 i.e. 6450 Kg/m^3 or 6.45 g/cm^3 i.e. 6450 Kg/m^3	7540-8000 Kg/m^3 or 7.15 g/cm^3 i.e. 7150 Kg/m^3	7100-7200 Kg/m^3 or 7.9 g/cm^3 i.e. 7900 Kg/m^3	7.90 g/cm^3 i.e. 7900 Kg/m^3	-
Thermal expansion coefficient, 10^{-6}	9.45-18.1 (1/°C)	6.6-11 (1/K)	17 (1/K)	17 (1/K)	-	11.2 (1/°C)

5.3 Potential of investigated Fe-SMA for thermomechanical applications

Table 5.11 shows the preliminary conditions at which laser flash analysis (LFA) of the investigated Fe-SMA has been performed. The reference temperature is a temperature of the laboratory where the experiments have been performed, it is kept constant around the clock inside the laboratory at a value of 20°C. It can also be called room temperature. Experiments have been performed under pure inert argon gas atmosphere.

Table 5.11
Preliminary conditions for experimental work

Sr. #	General Information during experimental work	Experimental conditions
1	Material	Fe-15Mn-10Cr-8Ni-4Si SMA
2	Instrument	Netzsch LFA 427
3	Sample	Disk specimen of Fe-15Mn-10Cr-8Ni-4Si SMA
4	Reference temperature (Lab or Room temperature)	20°C
5	Mass of sample “m” after blasting??	1.94539g
6	The volume of sample “v” after blasting??	0.26314 cm^3
7	Type	Single layer
8	Coating	Al_2O_3 25-50µm particles
9	The thickness of the sample (average of five values)	2.5 mm
10	The diameter of the sample (average of five values)	12.5 mm
11	Atmosphere	Pure inert argon gas
12	Gas flow rate (argon gas)	75 ml/min

Arc melting process has also been found to be suitable to produce a 15g button of the investigated Fe-SMA as discussed in the preceding chapter. The quantity of different elements in 15g button is given in Table 5.12.

Table 5.12
The quantity of different elements in 15g investigated Fe-SMA used in LFA measurement

Quantity of elements	Fe	Mn	Cr	Ni	Si
Theoretical	9.45g	2.25g	1.5g	1.2g	0.6g
Actual	9.4520g	2.2462g	1.4909g	1.1942g	0.6002g

5.3.1 Thermal diffusivity of the investigated Fe-SMA

The prediction of response time of active materials is significant for efficient use as actuators. This thermal diffusivity of the investigated Fe-SMA over a range of temperatures (α (T)) found out by LFA measurement, is required to be used in Eq. 3.1 for the calculations of thermal conductivity over a range of temperatures (λ (T)). Table 5.13 shows the results in terms of average thermal diffusivity of four/five different values at laser shots during LFA measurement of the sample alloy. Five measurements have been taken at 25.8°C by means of five laser shots, five measurements have been taken at 50.4°C by means of five laser shots, four measurements have been taken at 99.1°C by means of four laser shots, four measurements have been taken at 199.8°C by means of four laser shots, four measurements have been taken at 300°C by means of four laser shots, and four measurements have been taken at 400.2°C by means of four laser shots. Afterwards, averages of four/five different measurements of thermal diffusivity have been taken which are mentioned in Table 5.13. The data has not been recorded between 25.8°C to 50.4°C, 50.4°C to 99.1°C, 99.1°C to 199.8°C, 199.8°C to 300°C and 300°C to 400.2°C because LFA technique is completely different from that of DSC and dilatometry measurements in which measurements are taken while heating and cooling at some specific heating/cooling rate; contrary in LFA it has been waited until some special temperature reaches as described earlier. Table 5.13 also shows the data related to the dependence of thermal diffusivity on temperature during the temperature range of 20°C to 400°C. The data of thermal diffusivity mentioned in Table 5.13 has been plotted as thermal diffusivity-temperature diagram shown in

Fig. 5.20. Such type of data is very significant while using SMA as thermally activated actuators which require a short-time response.

Table 5.13
Thermal diffusivity of the investigated Fe-SMA at different temperatures

Sr. #	**Laser Shot Number**	**Temperature (°C)**	**Average Thermal Diffusivity "α" (mm^2/s)**
1	1, 2, 3, 4, 5	25.8	3.308
2	6, 7, 8, 9, 10	50.4	3.364
3	11, 12, 13, 14	99.1	3.552
4	15, 16, 17, 18	199.8	3.894
5	19, 20, 21, 22	300	4.151
6	23, 24, 25, 26	400.2	4.427

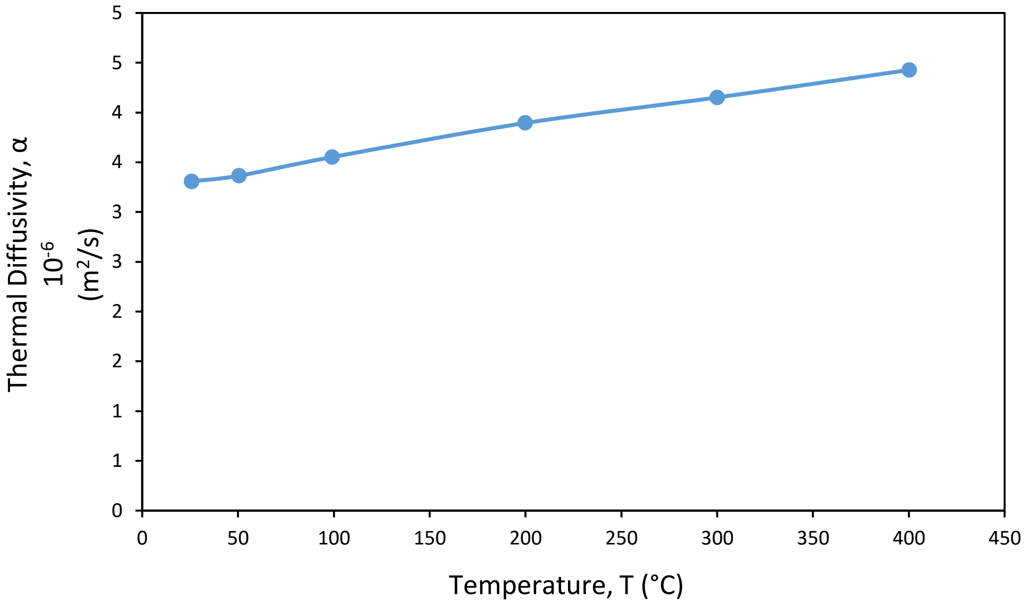

Fig. 5.20: Thermal diffusivity-temperature diagram for investigated Fe-SMA

In fact, the shape of the experimental curve in Fig. 5.20 shows that while heating from 25.8°C to 50.4°C, the thermal diffusivity of investigated Fe-SMA increases with less slope and the curve tends to be straight, afterward, the slope of the curve increases until it reaches the maximum temperature.

Fig. 5.21 shows the features of thermal diffusivity for Nitinol that there is a drastic decrease and then increase of thermal diffusivity during M-A transformation. It is mainly due to the heat capacity change [105].

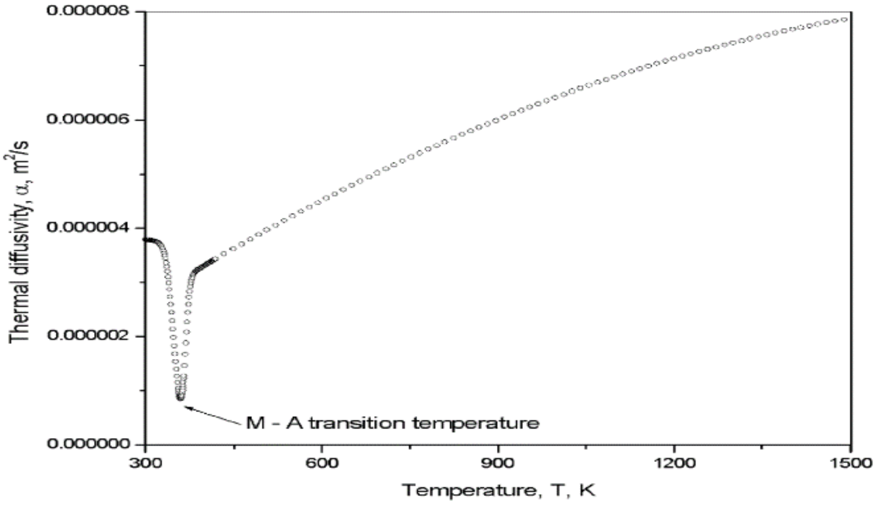

Fig. 5.21: Thermal diffusivity-temperature diagram for Nitinol [105]

A small temperature variation of Nitinol between M_f and A_f can produce large changes in properties like critical stresses and initial modulus because Nitinol is very sensitive to temperature between this transformation range of M_f and A_f which is very important characteristic in the sense that it helps to keep the operating temperature outside the transformation range while designing Nitinol actuators. Such a characteristic is also very important to be investigated for the design of other SMA actuators [117]. The sensitivity of SMA seems to be an intrinsic disadvantage [57].

However, Fig. 5.20 shows that the investigated Fe-SMA is not very sensitive to a temperature between that transformation range, also, there is no sudden decrease and increase of thermal diffusivity during M-A transformation contrary to that of Nitinol (Fig. 5.21).

5.3.2 Thermal conductivity calculations for the investigated Fe-SMA

The best method to find out thermal conductivity as a function of temperature is to compute using Eq. 3.1. It is utmost important to determine the potential of any material for thermomechanical applications. The thermal diffusivity of the investigated Fe-SMA over a range of temperatures (α (T)) has been found out by LFA measurement in subsection 5.3.1, the density of the investigated Fe-SMA over a range of temperatures (ρ (T)) has been found out by dilatometry measurement in subsection 5.2.1 whereas the specific heat capacity of the investigated Fe-SMA over a range of temperatures (C_P (T)) has been found out from Fig. 5.6 using DSC measurement in subsection 5.1.3. Now, the thermal conductivity of the investigated Fe-SMA over a range of temperatures (λ (T)) can be calculated by means of Eq. 3.1.

Table 5.14 shows the values of density of the investigated Fe-SMA at temperatures of 24.846°C, 49.846°C, 99.846°C, 199.846°C, 299.846°C, and 397.846°C; obtained from dilatometry results.

Table 5.14
The density of investigated Fe-SMA at different temperatures measured by dilatometry

Sr. #	**Temperature (°C)**	**Density "ρ" (g/cm^3)**
1	24.846	7.509056281
2	49.846	7.503019813

3	99.846	7.486824402
4	199.846	7.447223771
5	299.846	7.402780736
6	397.846	7.35806137

However, it is necessary to get the values of density of investigated Fe-SMA at LFA special temperatures of 25.8°C, 50.4°C, 99.1°C, 199.8°C, 300°C, and 400.2°C. These values have been calculated by unity method and the obtained values of density at LFA special temperatures of 25.8°C, 50.4°C, 99.1°C, 199.8°C, 300°C, and 400.2°C; are mentioned in Table 5.15.

Table 5.15
The density at LFA special temperatures calculated by unity method

Sr. #	**Temperature (°C)**	**Density “ρ” (g/cm^3)**
1	25.8	7.508825929
2	50.4	7.502840368
3	99.1	7.487066038
4	199.8	7.447223771
5	300	7.402710463
6	400.2	7.356987193

The obtained values of specific heat at LFA special temperatures of 25.8°C, 50.4°C, 99.1°C, 199.8°C, 300°C, and 400.2°C; are mentioned in Table 5.16. These values of specific heat have been taken from the DSC results described in section 5.1; except the first value of 0.47516 J/(g*K) at 25.8°C which has been obtained by extrapolating the logarithmic behavior of DSC curve by means of Eq. $y = 0.0354\ln(x) + 0.3601$ mentioned on DSC curve shown in Fig. 5.22. This value of C_P at 25.8°C was not available in DSC results because DSC measurement was started at a slightly higher temperature.

Table 5.16
The specific heat at LFA special temperatures measured by DSC

Sr. #	**Temperature (°C)**	**Specific Heat “C_P” (J/(g*K))**
1	25.8	0.47516
2	50.4	0.49571
3	99.1	0.53253
4	199.8	0.53854
5	300	0.56306
6	400.2	0.57498

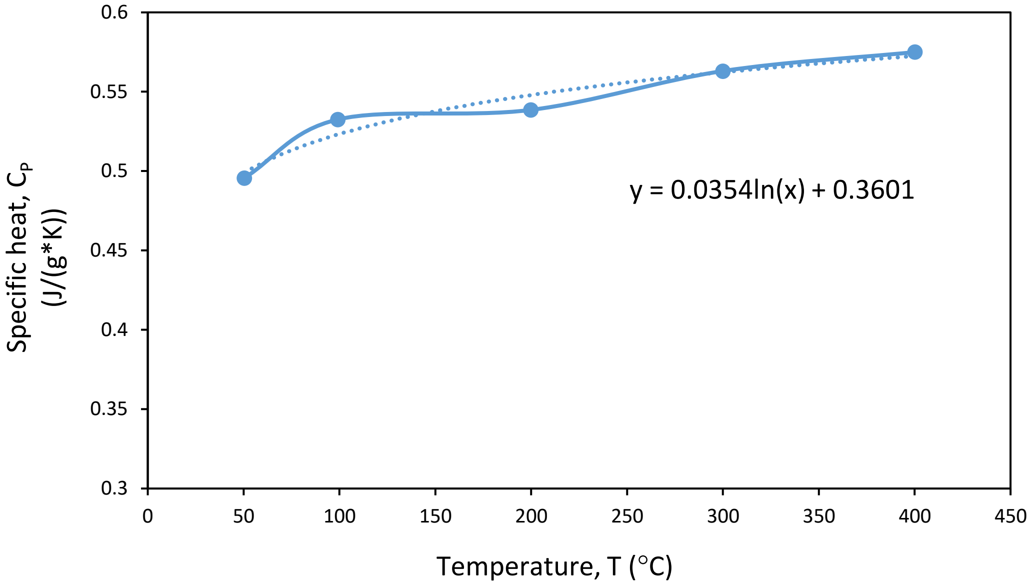

Fig. 5.22: Extrapolation of DSC curve to obtain the value of specific heat at 25.8°C

Now, thermal conductivity can be calculated by means of Eq. 3.1 at temperatures of 25.8°C, 50.4°C, 99.1°C, 199.8°C, 300°C, and 400.2°C as mentioned in Table 5.17 which also implies the data related to the dependence of thermal conductivity on temperature. The values of average thermal diffusivity in m^2/s obtained from Table 5.13, the values of density in Kg/m^3 obtained from Table 5.15, and the values of specific heat in J/Kg*K obtained from Table 5.16; at LFA special temperatures of 25.8°C, 50.4°C, 99.1°C, 199.8°C, 300°C, and 400.2°C are mentioned in Table 5.17. Thermal conductivity values in Table 5.17 have been calculated by multiplying the values of α, ρ and C_p stated in the same Table 5.17.

Table 5.17
The thermal conductivity of the investigated Fe-SMA calculated at different temperatures

Sr. #	**Laser Shot Number**	**Temperature (°C)**	**Average Thermal Diffusivity "α" (m^2/s)**	**Density "ρ" (Kg/m^3)**	**Specific Heat "C_P" (J/(Kg*K))**	**Thermal Conductivity "λ" (W/m*K)**
1	1, 2, 3, 4, 5	25.8	0.000003308	7508.825929	475.16	11.80259245
2	6, 7, 8, 9, 10	50.4	0.000003364	7502.840368	495.71	12.51149981
3	11, 12, 13, 14	99.1	0.000003552	7487.066038	532.53	14.16213401
4	15, 16, 17, 18	199.8	0.000003894	7447.223771	538.54	15.617385
5	19, 20, 21, 22	300	0.000004151	7402.710463	563.06	17.30207431
6	23, 24, 25, 26	400.2	0.000004427	7356.987193	574.98	18.72674344

The data of thermal conductivity mentioned in Table 5.17 has been plotted as thermal conductivity-temperature diagram as shown in Fig. 5.23.

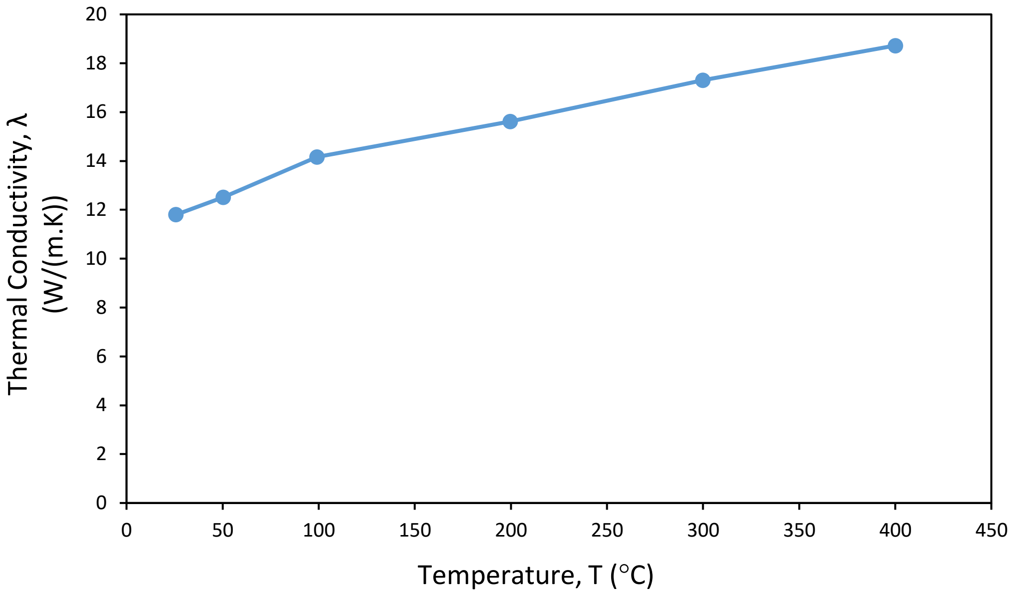

Fig. 5.23: Thermal conductivity-temperature diagram for investigated Fe-SMA

M. K. Stanford stated the thermal conductivities of several conventional bearing materials. These materials are M50 bearing steel, 440C stainless steel, 304 stainless steel, Stellite 6B and Hastelloy C [108]. It has been observed that their thermal conductivities are in the same range as that of investigated Fe-SMA in this work. Consequently, it can be stated that the range of thermal conductivity of investigated Fe-SMA is in the range of a variety of conventional engineering alloys used in bearings.

Thermal conductivity of the investigated Fe-SMA in this work is also comparable with that of 60-Nitinol which is useful to make different tools. It has also the useful properties like hardness (22 RC to 64 RC), high strength, low density, fine surface finish, low modulus, low thermal conductivity, low CTE, non-magnetic, and corrosion resistant [108][118]. Consequently, it can be stated that the range of thermal conductivity of investigated Fe-SMA is in the range of an alloy (60-Nitinol) used to make several tools.

The following Table 5.18 shows the thermal conductivities of numerous materials along with their applications in bearings, turbine blades, several pipe joints, rods, pipes, bolts, nuts, wires, studs, screws, allen keys, flange plates, seals, tools and washers; whose values are comparable with that of investigated Fe-SMA.

Table 5.18
Numerous materials and their applications whose thermal conductivities match with that of investigated Fe-SMA

Sr. #	**Material**	**Thermal Conductivity “λ” (W/m*K)**	**Applications**	**Reference**
1	304 stainless steel	15.1	Bearings, several pipe joints like elbow, rods, pipes, bolts, allen keys, flange plates, washers and so on.	[108]
2	Stellite 6B	14.7	Bearings, several pipe joints, rods, pipes, Nuts, bolts, flange plates and so on.	

3	Hastelloy C	11.5	Bearings, several pipe joints, rods, pipes, Nuts, bolts, flange plates, seals and so on.	
4	M50 bearing steel	25.9	Bearings	
5	Silicon nitride	22	Bearings	
6	Titanium	19-23	Bearings	
7	Antimony	18.5	Bearings	Engineering Toolbox
8	Chrome Nickel Steel (18% Cr, 8 % Ni)	16.3	Bearings and tools	
9	Monel	26	Bolts, nuts, several pipe joints, flange plates, rods, wires, studs, screws, and washers etc	
10	Silicon Carbide	15.2	Bearings	
11	Inconel	15	Turbine blades, several pipe joints, rods, pipes, bolts, nuts, flange plates, washers and so on	
12	Incoloy	12	Several pipe joints, rods, pipes, bolts, nuts, flange plates, washers and so on	
13	60-NITINOL (water-quenched)	8.9-13.7	Tools	[108][118]

Table 5.19 shows the comparison of thermal diffusivity and thermal conductivity which have been investigated in this work for the investigated Fe-SMA with state-of-the-art SMAs and some well-known conventional materials e.g. Nitinol, stainless steel, 60-Nitinol, and two different Cu-SMAs. The values of thermal diffusivities for stainless steel and two different Cu-SMAs mentioned in Table 5.19, have been calculated by means of $\lambda = \alpha * \rho * C_P$ i.e. (i) for CuZnAl, the equation becomes 84 W/m.K = α * 440 J/Kg.K * 7150 Kg/m^3, which gives thermal diffusivity "α" as 2.670057216x10^{-5} m^2/s or 0.267 cm^2/s; where W shows Watt which is equal to J/s, (ii) for CuAlNi, the equation becomes 69 W/m.K = α * 390 J/Kg.K * 7900 Kg/m^3, which gives thermal diffusivity "α" as 2.239532619x10^{-5} m^2/s or 0.224 cm^2/s, and (iii) for Stainless steel 316L, the equation becomes 16.3 W/m.K = α * 500 J/Kg.K * 7900 Kg/m^3, which gives thermal diffusivity "α" as 4.126582278x10^{-6} m^2/s or 0.0413 cm^2/s.

Table 5.19 [63][108][110][111]
Comparison of obtained thermal properties of investigated Fe-SMA with that of well-known materials

Property	**Fe-15Mn-10Cr-8Ni-4Si SMA**	**Nitinol**	**CuZnAl**	**CuAlNi**	**Stainless steel 316L**	**60-Nitinol**
Thermal conductivity (20°C) (Watt/meter *kelvin)	11.8-18.7 W/m K	8.6-18 W/m K or 10-18 W/m K	84-120 W/m K or 84 W/m K	30-75 W/m K or 69 W/m K	16.3 W/m K	8.9-13.7 W/m K
Thermal diffusivity	0.03308-0.04427 cm^2/s	0.125 cm^2/s	0.267 cm^2/s	0.224 cm^2/s	0.0413 cm^2/s	-

Zanotti et al. [105] proved from their numerical work that the data related dependence of thermal diffusivity, density, specific heat and thermal conductivity on temperature is necessary to start numerical computations. The parameters in the below-mentioned Table 5.20 have been used to perform numerical work.

Table 5.20 [105]
Parameters used to start numerical work

Sr. #	Parameter	Symbol	Unit
1	specific heat	C_P	J/(Kg K)
2	thermal conductivity	K or λ	J/(m s K)
3	thermal diffusivity	α	m^2/s
4	density	ρ	Kg/m^3
5	sample cross-sectional area	A	m^2
6	convection heat transfer coefficient	h	J/(m^2 s K)
7	surface reflectivity index	r	-
8	sample perimeter	S	m
9	temperature	T	K
10	time	t	s
11	1D space abscissa	x	m
12	heated surface emissivity	ε	-
13	Boltzmann constant	σ	-
14	reference	ref	-
15	heated surface	0	-
16	cold surface	e	-
17	sample surrounding atmosphere	g	-
18	lateral (cylindrical surface)	s	-

5.4 Uniaxial compression analysis

In this section, a series of uniaxial compression tests is performed to investigate numerous aspects of mechanical behavior of Fe-SMA. These tests have been performed on the samples shown in Fig. 4.4b by means of Zwick/Roell Z100 materials testing machine operating in axial strain control. Two samples are tested at room temperature, third sample at 200°C, whereas fourth one at 400°C. The quasi-static load has been applied during the tests with a loading speed of 5.8×10^{-4} mm/s. Unlike static and dynamic load, the quasi-static load is slow enough in a way that its inertial effects are negligible. Table 5.21 shows the preliminary conditions at which uniaxial compression tests of the investigated alloy have been performed.

Table 5.21
Preliminary conditions for experimental work

General information during experimental work	
Machine	Zwick/Roell Z100 materials testing machine
Measuring mode	Compression
Sample	Cylindrical specimen of Fe-15Mn-10Cr-8Ni-4Si SMA
Initial length of the specimen, $L_{initial}$	6mm (ideal)
Initial diameter of the specimen, $D_{initial}$	4mm (ideal)
Initial cross-sectional area of the specimen ($A=\pi r^2$)	12.5664 mm^2
Loading speed during uniaxial compression	5.8×10^{-4} mm/s
Temperature	Room temperature (20°C), 200°C, 400°C

Following results have been obtained from these monotonic tests at room temperature as well as at elevated temperatures. The results have also been tabularized as well as approximated values are taken e.g. 8000 MPa instead of 7990 MPa.

5.4.1 Uniaxial compression at room temperature

The first specimen has been compressed by applying an axial compressive force, F_{zz} shown in Fig. 5.24; up to a maximum value of 6100N at a loading speed of 5.8×10^{-4} mm/s. The strain is the ratio of the deformation of an object over its original dimension. For axial strain there should be axial deformation shown in Fig. 5.24 in the same direction to the applied force.

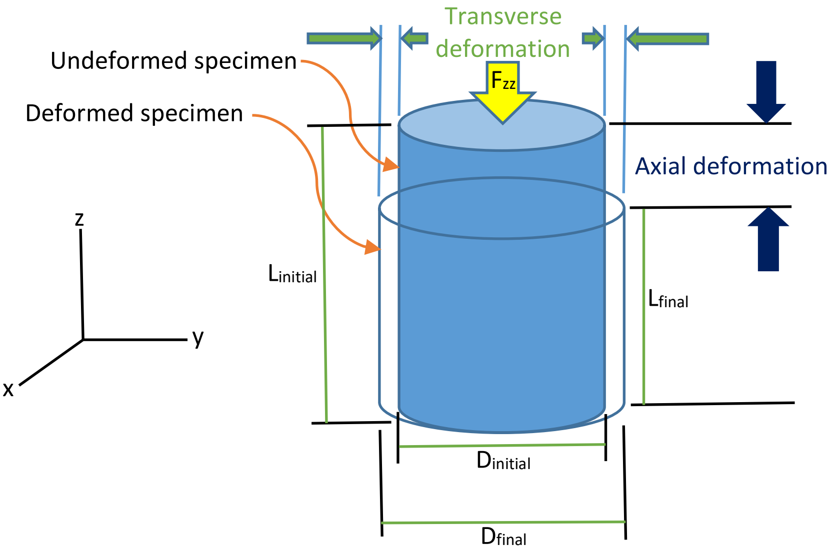

Fig. 5.24: The representation of axial plastic deformation and transverse plastic deformation in the sample used for uniaxial compression analysis of the investigated Fe-SMA

The total deformation in the length of cylindrical specimen over the original length equals axial strain. The strains ε_{xx}, ε_{yy}, and ε_{zz} are aligned x, y, and z of coordinate system in Fig. 5.24.

The total strain (ε_{zz}) is the sum of elastic strain ($\varepsilon_{e,\ zz}$) and the plastic strain ($\varepsilon_{p,\ zz}$) i.e. $\varepsilon_{zz} = \varepsilon_{e,\ zz} + \varepsilon_{p,\ zz}$.

The curves in this section 5.4 are not perfectly straight in the very beginning which can be due to the disturbance effect because at the start of experiments the specimens are not perfectly in contact and aligned with pressing plate. The specimens are first kept on the lower plate then upper plate is moved towards the specimens. A perfect contact is built on each specimen in order to make the plates aligned with these specimens. While doing this process the material is supposed to be the softer material thus the curve is not perfectly straight in the very beginning. After achieving the required contact and alignment, the material is possible to be compressed perfectly and precise material behavior is obtained.

The axial compressive displacement (ΔL_{zz}) of first specimen at different values of force (F_{zz}) is mentioned in Fig. 5.25 which shows a maximum axial compressive displacement of 0.6mm that means the initial undeformed length ($L_{initial}$) having a value of 6mm for first specimen reduces by an amount of 0.6mm after compression. That’s why, 0.6/6*100 = 10% is the total axial compressive strain after compression as shown in Fig. 5.26. However, a part of the displacement

(0.6mm) is recovered after removing the load because the investigated alloy is SMA as elaborated below. Likewise, a part of total axial compressive strain (10%) is recovered after removing the load as indicated in Fig. 5.26. The data has been obtained in .TRA file which is transferred in excel file before plotting.

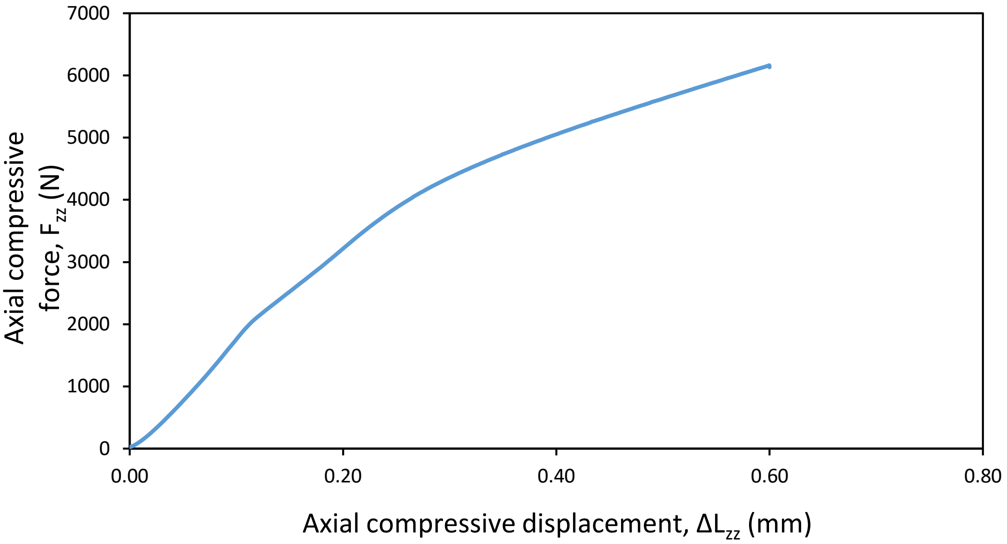

Fig. 5.25: Force-deformation behavior for uniaxial compression of first specimen of the investigated Fe-SMA at room temperature

The stress has been calculated by means of $\sigma_{zz} = F_{zz}/A$, where F_{zz} is the axial compressive force mentioned in Fig. 5.24 and Fig. 5.25 and A is the initial cross-sectional area of the cylindrical specimen. The axial compressive force is in N whereas area is in mm^2, therefore, the unit of stress is N/mm^2 (MPa).

Besides, the strain percentage has also been calculated by means of $\varepsilon_{zz} = \Delta L_{zz}/L_{initial}*100$, where ΔL_{zz} is the axial compressive displacement mentioned on x-axis of Fig. 5.25 and $L_{initial}$ is the initial length of the specimen before compression.

Note: There should be minus sign with axial compressive displacement due to uniaxial compression, however, it is not mentioned in this section 5.4 therefore the results are in first quadrant instead of third quadrant.

The stress-strain curve has now been plotted in Fig. 5.26. The yield strength evaluated from Fig. 5.26 is 170 MPa and the range of elastic strain is about 2%. The total axial compressive strain after compression is 10% which has been elaborated earlier, a part of it is recovered after removing the load as shown in Fig. 5.26. The value of initial length ($L_{initial}$) of undeformed first specimen used at room temperature is 6mm. The final length of first specimen after compression should be 6mm – 0.6mm = 5.4mm, however, it expands to a small extent after removing the load because it is SMA thus final length (L_{final}) becomes 5.81mm. Now the axial plastic deformation, $\Delta L_{p,\, zz}$ under uniaxial compression can be obtained as follows;

$$\text{Axial plastic deformation, } \Delta L_{p,\, zz} = L_{initial} - L_{final} = 6\text{mm} - 5.81\text{mm} = 0.19\text{mm}$$

Note: The value of axial plastic deformation, $\Delta L_{p,\, zz}$ cannot be greater than the maximum displacement described in force-deformation diagram.

The axial plastic strain, $\varepsilon_{p,\ zz}$ of first specimen after compression is obtained by Eq. 5.3, then axial strain recovered is possible to be calculated.

$$\varepsilon_{p,\ zz} = \frac{\Delta L_{p,\ zz}}{L_{initial}} = \frac{0.19}{6} = 0.032 \tag{5.3}$$

Note: The axial plastic strain is positive in case of tension but negative in case of compression because final length decreases in compression. However, the positive convention is used in this thesis as discussed earlier.

In other words, the specimen with 6mm length is displaced to a value of 0.6mm (shown in Fig. 5.25) but the remaining length after deformation is 5.81mm (instead of 6mm – 0.6mm = 5.4mm) which is 96.8% of 6mm, consequently, the remaining 100 – 96.8 = 3.2% is the axial plastic strain ($\varepsilon_{p,\ zz}$) as located on x-axis of Fig. 5.26. The total axial compressive strain on x-axis of Fig. 5.26 is 10% out of which 3.2% is axial plastic strain, therefore, the remaining 6.8% is the axial strain recovered. There is an imaginary unloading curve (linearly approximated) because exact unloading curve could not be obtained due to unavailability of unloading analysis on uniaxial compression machine.

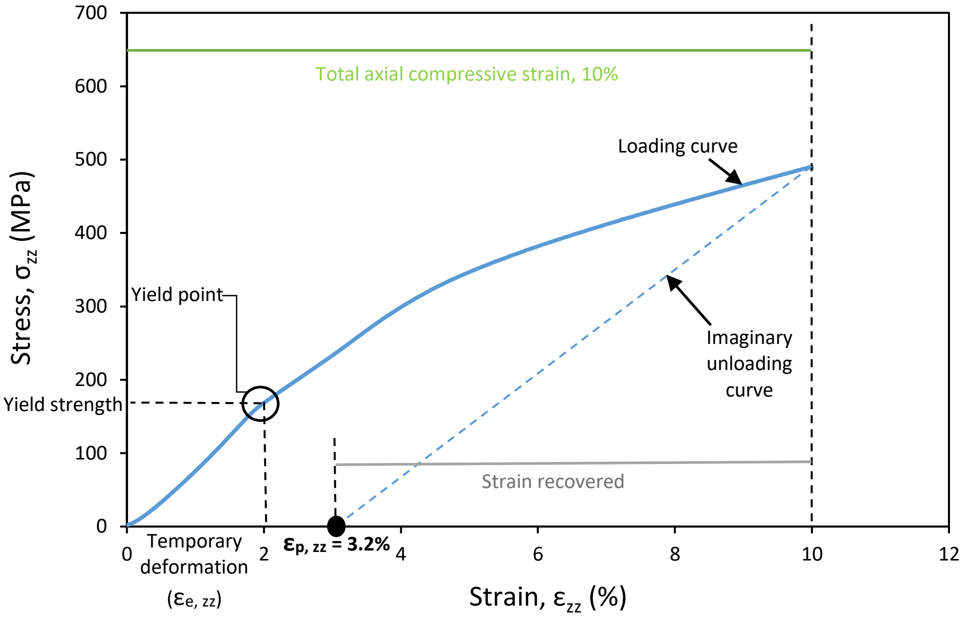

Fig. 5.26: Stress-strain behavior for uniaxial compression of first specimen of the investigated Fe-SMA at room temperature

Modulus of elasticity of a material is the ratio of stress (force per unit area) and strain (proportional deformation) in linear elastic regime. It is also a measure to the stiffness of a solid material. Stiffness is the extent to which a material resists the elastic deformation in response to an applied force.

The elastic part has been plotted in Fig. 5.27. The data on x-axis is dimensionless strain ($\Delta L_{zz}/L_{initial}$) instead of percent strain in order to calculate the modulus of elasticity for the investigated Fe-SMA which is possible to be calculated by slope of this curve in elastic range. The modulus of elasticity evaluated from Fig. 5.27 is 8000 MPa, in fact it is austenitic modulus of elasticity denoted by E_A because the material is in austenitic state at room temperature as shown by XRD results in subsection 5.1.7.

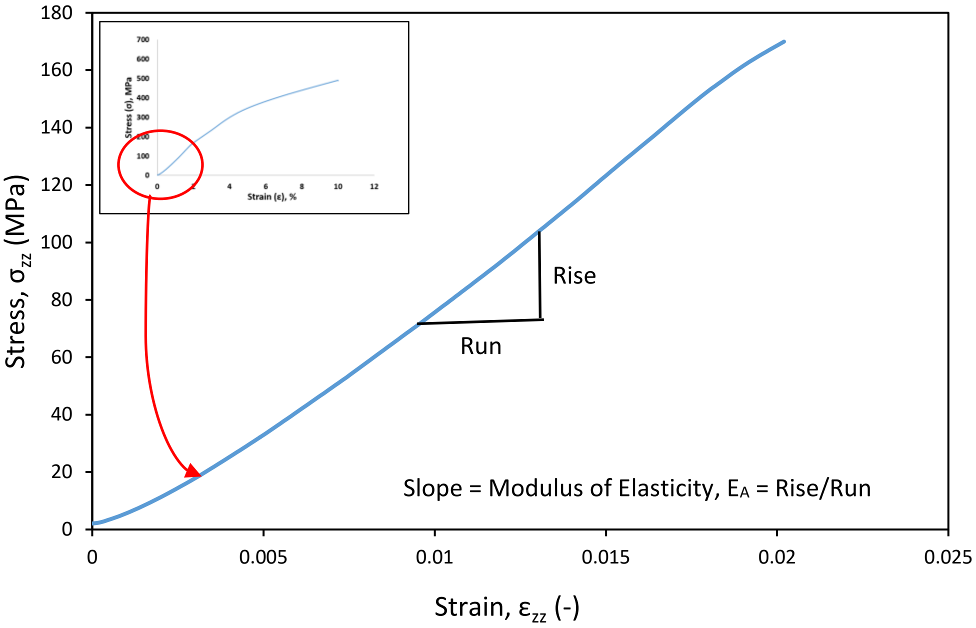

Fig. 5.27: Stress-strain behavior in elastic range for uniaxial compression of first specimen of the investigated Fe-SMA at room temperature

All the obtained results of uniaxial compression of first specimen at room temperature, are tabularized in Table 5.22. These are experimental investigations which are expected to be the exact values due to lack of research on Fe-15Mn-10Cr-8Ni-4Si SMA.

Table 5.22
The investigated mechanical properties for Fe-SMA of interest at room temperature (first specimen)

Sr. #	**Mechanical property**	**Value**
1	Yield Strength, σ_y	170 MPa
2	Elastic strain, $\varepsilon_{e,\ zz}$	2.02%
3	Total axial compressive strain after compression	10%
4	Modulus of elasticity, E_A	8000 MPa
5	Axial plastic strain, $\varepsilon_{p,\ zz}$	3.2%
6	Axial strain recovered	6.8%

The second specimen has also been tested at room temperature on the same conditions as that of first specimen. The quite similar results have been obtained by second specimen as described below.

The force-deformation diagram showing axial compressive displacement of second specimen at different values of force is mentioned in Fig. 5.28 which shows a maximum axial compressive displacement of 0.63mm that means the initial undeformed length ($L_{initial}$) having a value of 6.18mm for second specimen reduces by an amount of 0.63mm after compression. That's why, 0.63/6.18*100 = 10.2% is the total axial compressive strain after compression as shown in Fig. 5.29. However, a part of displacement as well as a part of total axial compressive strain is recovered after removing the load as indicated in Fig. 5.29.

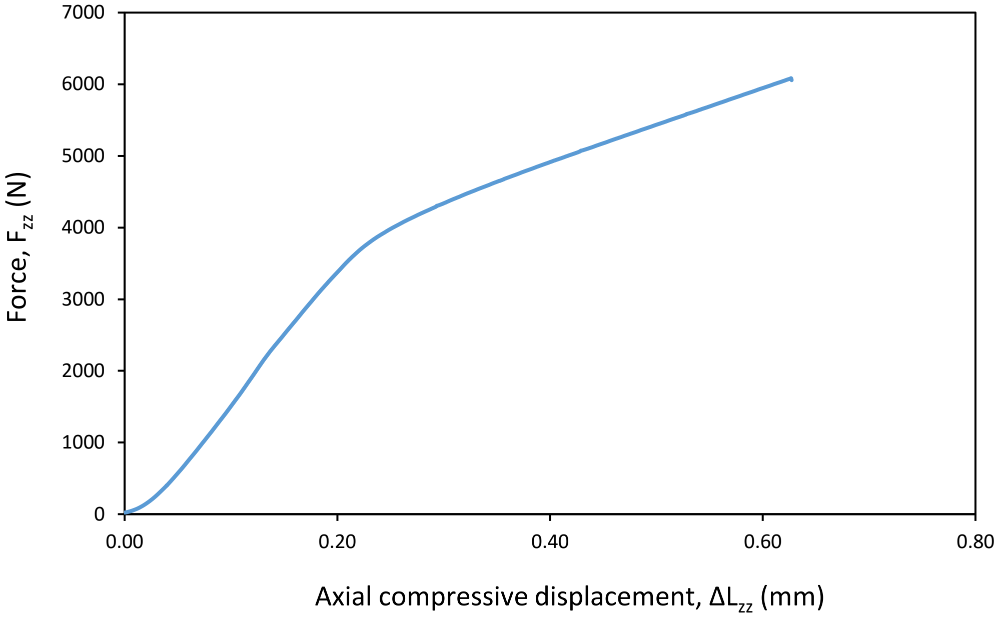

Fig. 5.28: Force-deformation behavior for uniaxial compression of second specimen of the investigated Fe-SMA at room temperature

The stress-strain diagram for second specimen at room temperature is mentioned in Fig. 5.29. The yield strength evaluated from Fig. 5.29 is 180 MPa and the range of elastic strain is about 2.4%. The total axial compressive strain after compression is 10.2% a part of which is recovered after removing the load as shown in Fig. 5.29. The value of initial length ($L_{initial}$) of undeformed second specimen used at room temperature is 6.18mm. The final length of second specimen after compression should be 6.18mm – 0.63mm = 5.55mm, however, it expands by unloading because it is SMA thus final length (L_{final}) becomes 5.77mm. Now the axial plastic deformation, $\Delta L_{p,\ zz}$ under uniaxial compression is;

Axial plastic deformation, $\Delta L_{p,\ zz} = L_{initial} – L_{final}$ = 6.18mm - 5.77mm = 0.41mm

The axial plastic strain, $\varepsilon_{p,\ zz}$ for second specimen after compression is evaluated by Eq. 5.4, then axial recovery strain is possible to be calculated.

$$\varepsilon_{p,\ zz} = \frac{\Delta L_{p,\ zz}}{L_{initial}} = \frac{0.41}{6.18} = 0.066 \tag{5.4}$$

In other words, the specimen with 6.18mm length is displaced to a value of 0.63mm (shown in Fig. 5.28) but the remaining length after deformation is 5.77mm (instead of 6.18mm – 0.63mm = 5.55mm) which is 93.4% of 6.18mm, consequently, the remaining 100 – 93.4 = 6.6% is the axial plastic strain ($\varepsilon_{p,\ zz}$) as located on x-axis of Fig. 5.29. The total axial compressive strain on x-axis of Fig. 5.29 is 10.2% out of which 6.6% is axial plastic strain, therefore, the remaining 3.6% is the axial strain recovered.

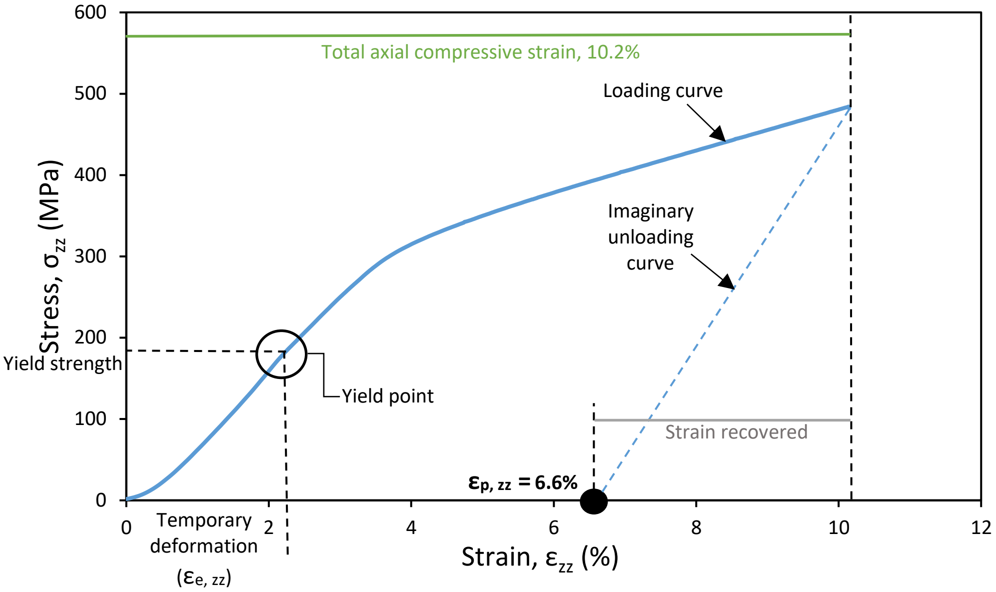

Fig. 5.29: Stress-strain behavior for uniaxial compression of second specimen of the investigated Fe-SMA at room temperature

The stress-strain diagram in elastic part for second specimen at room temperature is mentioned in Fig. 5.30. The modulus of elasticity, E_A evaluated from the slope of this curve is 7500 MPa.

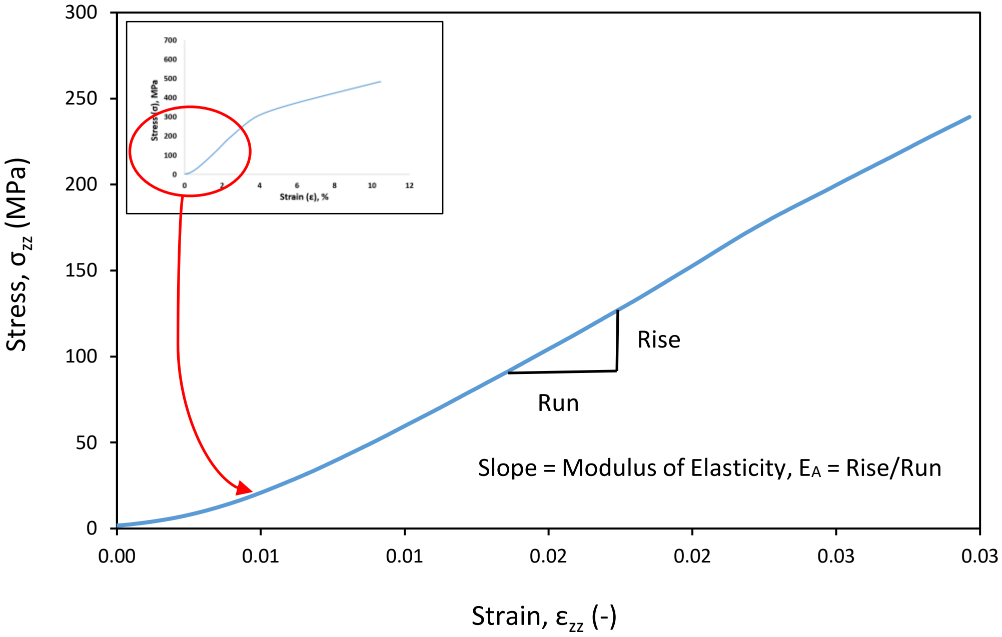

Fig. 5.30: Stress-strain behavior in elastic range for uniaxial compression of second specimen of the investigated Fe-SMA at room temperature

All the obtained results of uniaxial compression of second specimen at room temperature, are tabularized in Table 5.23.

Table 5.23
The investigated mechanical properties for Fe-SMA of interest at room temperature (second specimen)

Sr. #	Mechanical property	Value
1	Yield Strength, σ_y	180 MPa
2	Elastic strain, $\varepsilon_{e,\,zz}$	2.4%
3	Total axial compressive strain	10.2%

4	Modulus of elasticity, E_A	7500 MPa
5	Axial plastic strain, $\varepsilon_{p,\ zz}$	6.6%
6	Axial strain recovered	3.6%

In this subsection 5.4.1, there are two experiments at same conditions (room temperature). It seems these two experiments are not sufficient to achieve reliable results for Young's modulus as well as for other correlated material parameters because the results from both experiments are not exactly similar. It has been concluded that the said difference of results for the parameters like Young's modulus, E is 8000 MPa in first experiment whereas 7500 MPa in second experiment; is due to the different number of obtained experimental values from two experiments. The number of obtained experimental values from first experiment (specimen#1) are 240, however, from second experiment (specimen#2) are 350; which means the time of second experiment has been enhanced, consequently, the obtained mean values (results) differ. Statistically this is a slight difference which is not considerable, besides, if mean of only 240 experimental values for both experiments are taken, then, there remains a minor difference and the results of two experiments almost coincide (e.g. Young's modulus, E is 7484 MPa for first experiment and 7393 MPa for second experiment.

5.4.2 Microstructure after deformation

To analyze the effect of uniaxial compression on microstructure, the microstructure of the specimen deformed by uniaxial compression at room temperature has been examined. The martensite is brittle because its microstructure contains many needle-shaped features. The emergence of stress-induced hexagonal close-packed (HCP) ε-martensite is observed in microstructure of the investigated Fe-SMA after uniaxial compression deformation as shown by black needle-shaped features in Fig. 5.31. These needles show the reoriented de-twinned martensite, whereas the other remaining part of microstructure shows the twinned martensite.

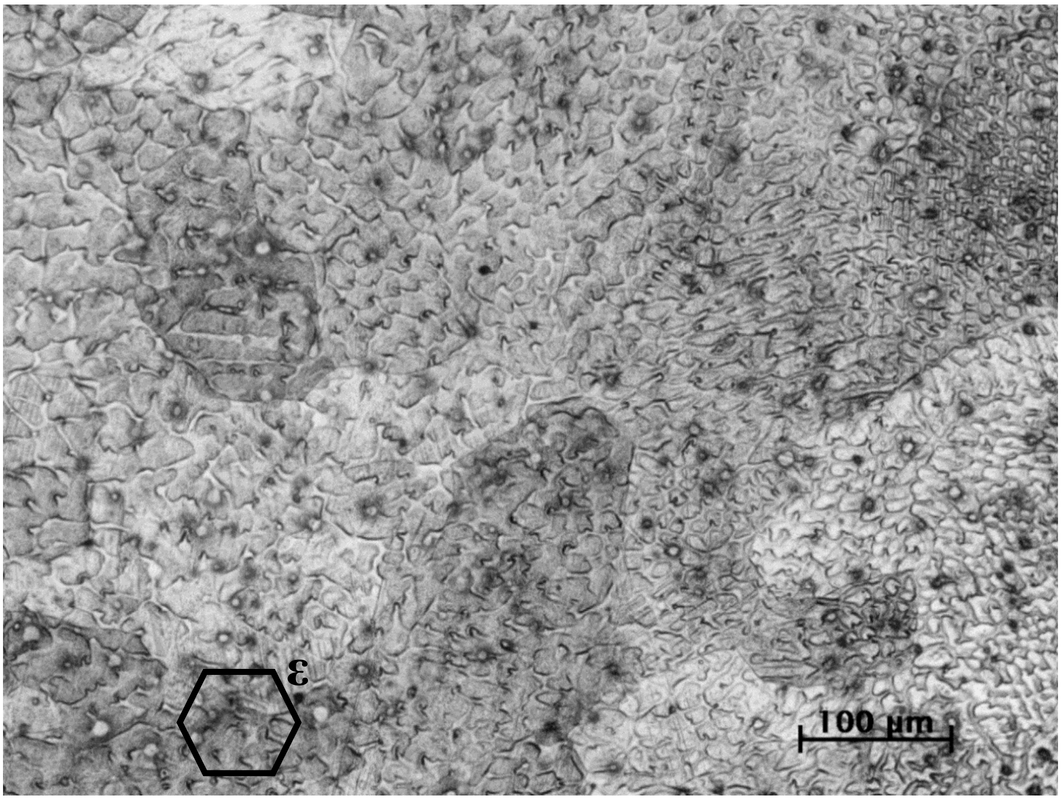

Fig. 5.31: Optical microscopic (OM) microstructure after deformation

5.4.3 Uniaxial compression at an elevated temperature of 200°C

The third specimen has been compressed by applying a compressive force and speed as that of first and second specimen, however, it is compressed at an elevated temperature of 200°C. The axial compressive displacement (ΔL_{zz}) for third specimen at different values of force (F_{zz}) is stated in Fig. 5.32 which shows a maximum axial compressive displacement of 1.17mm that means the initial undeformed length ($L_{initial}$) having a value of 6.2mm for third specimen reduces by an amount of 1.17mm after compression. That's why, 1.17/6.2*100 = 18.87% is the total axial compressive strain after compression as shown in Fig. 5.33. However, a part of displacement as well as a part of total axial compressive strain is recovered after removing the load as shown in Fig. 5.33.

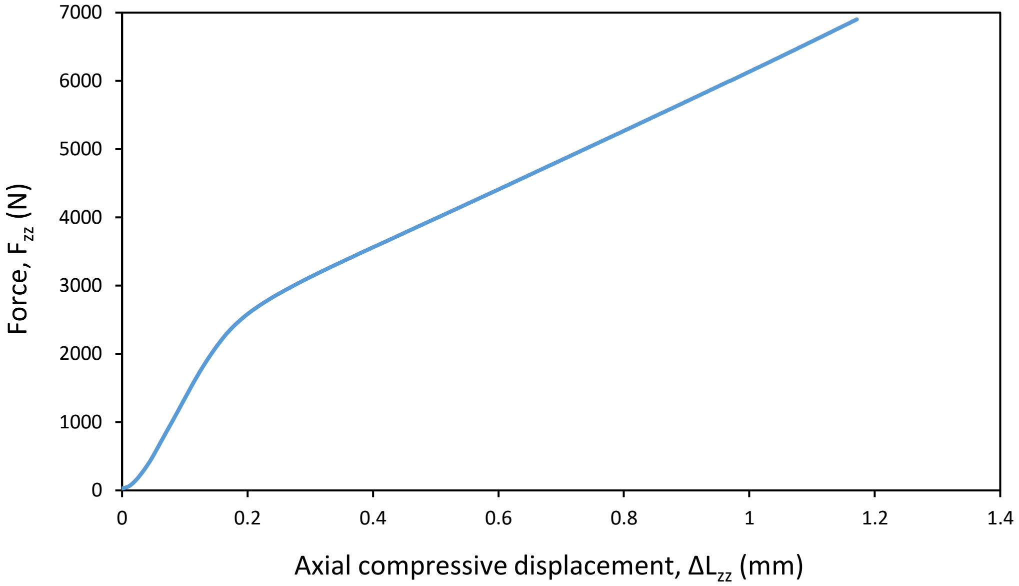

Fig. 5.32: Force-deformation behavior for uniaxial compression of third specimen of the investigated Fe-SMA at 200°C

Now, the stress and strain percentage have been calculated by the method discussed earlier. Then the stress-strain curve at an elevated temperature of 200°C is plotted in Fig. 5.33. The yield strength evaluated from Fig. 5.33 is 190 MPa and the range of elastic strain is about 3.2%. The total axial compressive strain after compression is 18.87% a part of which is recovered after removing the load as shown in Fig. 5.33. The value of initial length ($L_{initial}$) for third specimen before heating as well as before compression is 6.2mm, which is then put into the chamber of machine for experiment. After that, the chamber is closed. The compression of third specimen is started when a temperature of 200°C reaches inside the chamber. The final length (L_{final}) of the specimen after compression is 5.31mm. Now, axial plastic deformation, $\Delta L_{p,\ zz}$ under uniaxial compression at 200°C is;

Axial plastic deformation, $\Delta L_{p,\ zz} = L_{initial} - L_{final} = 6.2\text{mm} - 5.31\text{mm} = 0.89\text{mm}$

The axial plastic strain, $\varepsilon_{p,\ zz}$ of this specimen after compression is given by Eq. 5.5, then axial recovery strain can be calculated.

$$\varepsilon_{p,\ zz} = \frac{\Delta L_{p,\ zz}}{L_{initial}} = \frac{0.89}{6.2} = 0.1436 \tag{5.5}$$

In other words, the specimen with 6.2mm length is displaced to a value of 1.17mm (shown in Fig. 5.32) but the remaining length after deformation is 5.31mm (instead of 6.2mm – 1.17mm = 5.03mm) which is 85.64% of 6.2mm, consequently, the remaining 100 – 85.64 = 14.36% is the axial plastic strain ($\varepsilon_{p,\,zz}$) as located on x-axis of Fig. 5.33. The total axial compressive strain on x-axis of Fig. 5.33 is 18.87% out of which 14.36% is axial plastic strain, therefore, the remaining 4.51% is the axial strain recovered.

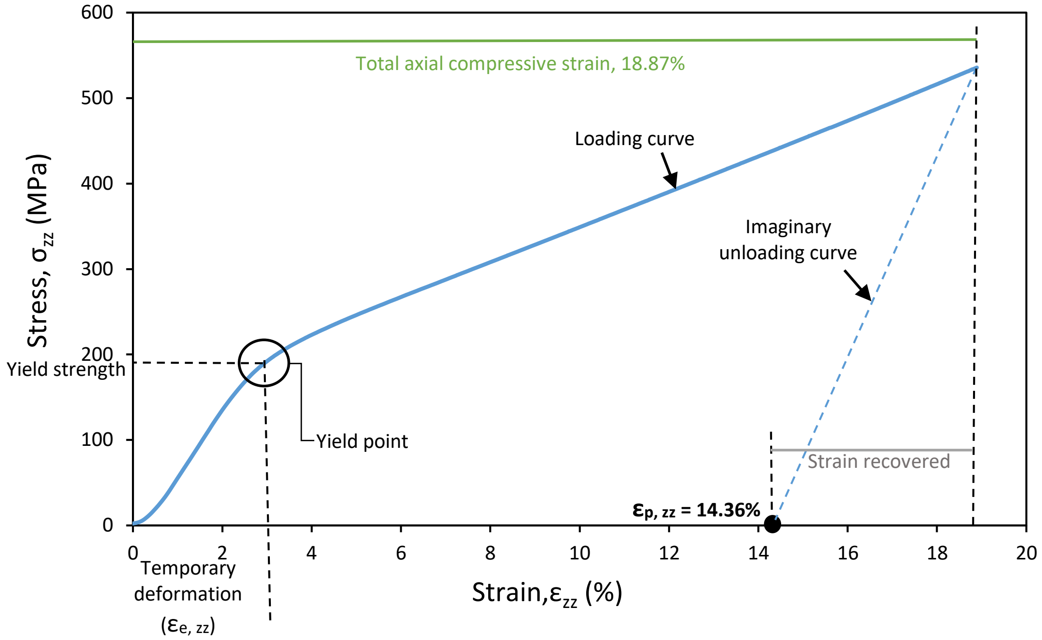

Fig. 5.33: Stress-strain behavior for uniaxial compression of third specimen of the investigated Fe-SMA at 200°C

The elastic part for uniaxial compression of third specimen at 200°C has been plotted in Fig. 5.34. The modulus of elasticity, E_A evaluated from the slope of the below-mentioned diagram is 6700 MPa.

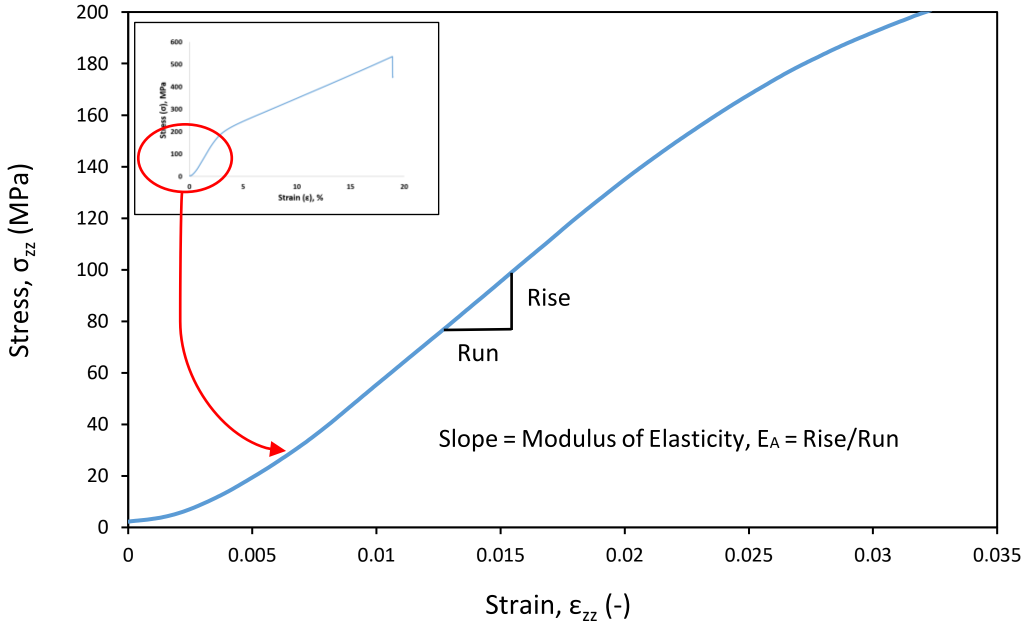

Fig. 5.34: Stress-strain behavior in elastic range for uniaxial compression of third specimen of the investigated Fe-SMA at 200°C

All the obtained results of uniaxial compression of third specimen at 200°C, are tabularized in Table 5.24.

Table 5.24
The investigated mechanical properties for Fe-SMA of interest at 200°C (third specimen)

Sr. #	Mechanical property	Value
1	Yield Strength, σ_y	190 MPa
2	Elastic strain, $\varepsilon_{e,\,zz}$	3.2%
3	Total axial compressive strain	18.87%
4	Modulus of elasticity, E_A	6700 MPa
5	Axial plastic strain, $\varepsilon_{p,\,zz}$	14.36%
6	Axial strain recovered	4.51%

5.4.4 Uniaxial compression at an elevated temperature of 400°C

The axial compressive displacement (ΔL_{zz}) of fourth specimen at different values of force (F_{zz}) at an elevated temperature of 400°C is plotted in Fig. 5.35 which shows a maximum axial compressive displacement of 1.1mm that means the initial undeformed length ($L_{initial}$) having a value of 6.33mm for fourth specimen reduces by an amount of 1.1mm after compression. That's why, 1.1/6.33*100 = 17.38% is the total axial compressive strain after compression as shown in Fig. 5.36. However, a part of displacement as well as a part of total axial compressive strain is recovered after removing the load as shown in Fig. 5.36.

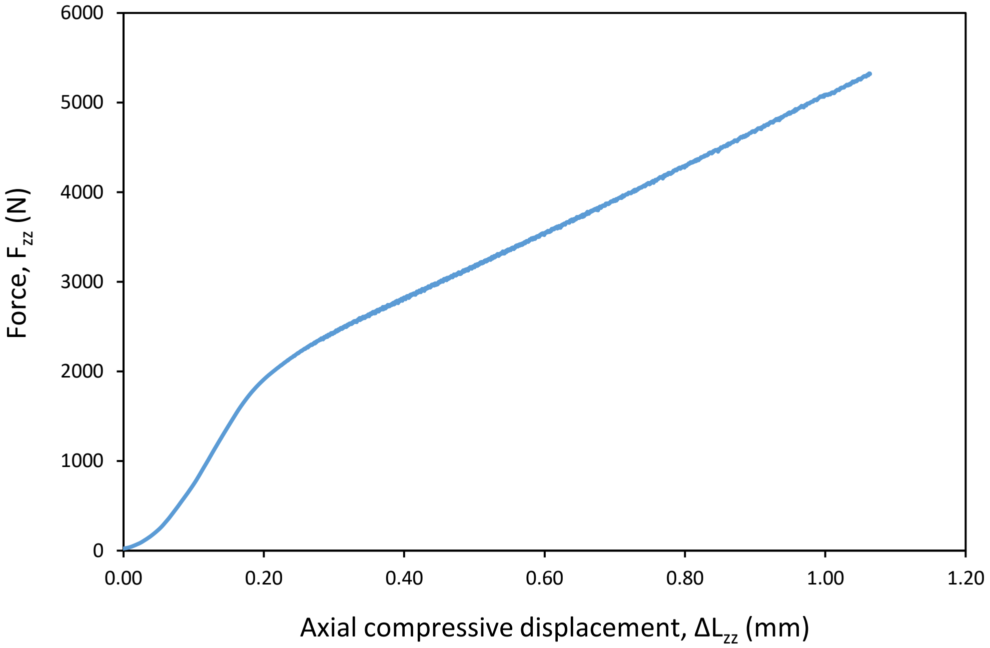

Fig. 5.35: Force-deformation behavior for uniaxial compression of fourth specimen of the investigated Fe-SMA at 400°C

The stress-strain diagram for fourth specimen at 400°C is plotted in Fig. 5.36. The yield strength evaluated from Fig. 5.36 is 145 MPa and the range of elastic strain is about 3.4%. The total axial compressive strain after compression is 17.38% a part of which is recovered after removing the load as shown in Fig. 5.36. The value of initial length ($L_{initial}$) for fourth specimen before heating as well as before compression is 6.33mm, which is then put into the chamber of machine for experiment. After that, the chamber is closed. The compression of fourth specimen is started when a temperature of 400°C reaches inside the chamber. The final length (L_{final}) of the specimen after compression is 5.41mm. Now, axial plastic deformation, $\Delta L_{p,\ zz}$ under uniaxial compression at 400°C is;

Axial plastic deformation, $\Delta L_{p,\ zz} = L_{initial} - L_{final}$ = 6.33mm - 5.41mm = 0.92mm

The axial plastic strain, $\varepsilon_{p,\ zz}$ of this specimen after compression is given by Eq. 5.6, then axial recovery strain can be calculated.

$$\varepsilon_{p,\ zz} = \frac{\Delta L_{p,\ zz}}{L_{initial}} = \frac{0.92}{6.33} = 0.1453 \tag{5.6}$$

In other words, the specimen with 6.33mm length is displaced to a value of 1.1mm (shown in Fig. 5.35) but the remaining length after deformation is 5.41mm (instead of 6.33mm – 1.1mm = 5.23mm) which is 85.47% of 6.33mm, consequently, the remaining 100 – 85.47 = 14.53% is the axial plastic strain ($\varepsilon_{p,\ zz}$) as located on x-axis of Fig. 5.36. The total axial compressive strain on x-axis of Fig. 5.36 is 17.38% out of which 14.53% is axial plastic strain, therefore, the remaining 2.85% is the axial strain recovered.

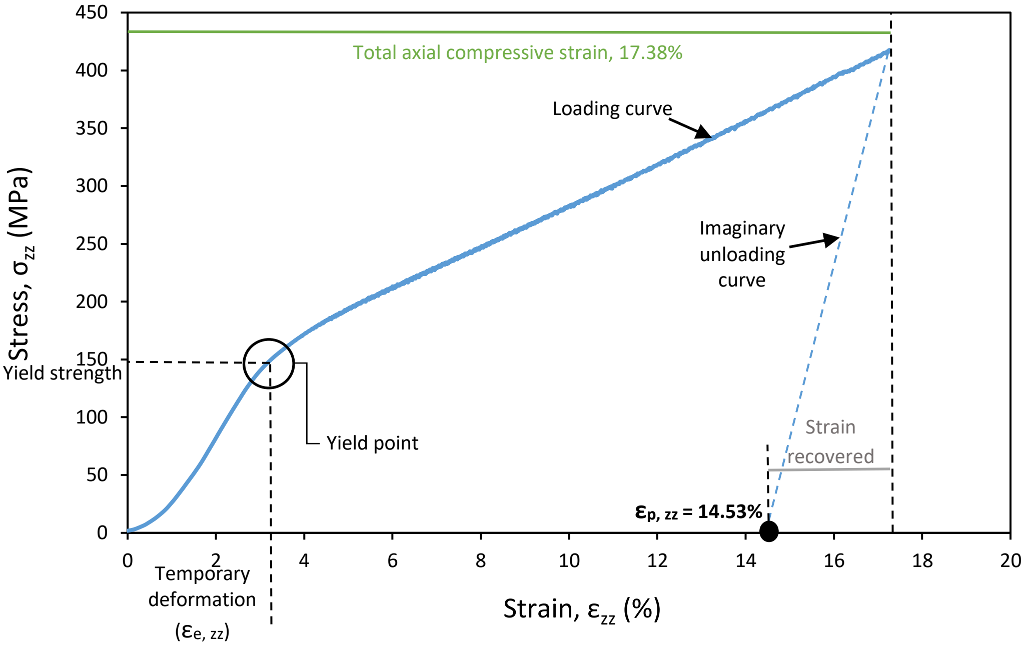

Fig. 5.36: Stress-strain behavior for uniaxial compression of fourth specimen of the investigated Fe-SMA at 400°C

The elastic part of the results of fourth specimen at 400°C has been plotted in Fig. 5.37 whose slope gives the value of modulus of elasticity, E_A as 4600 MPa.

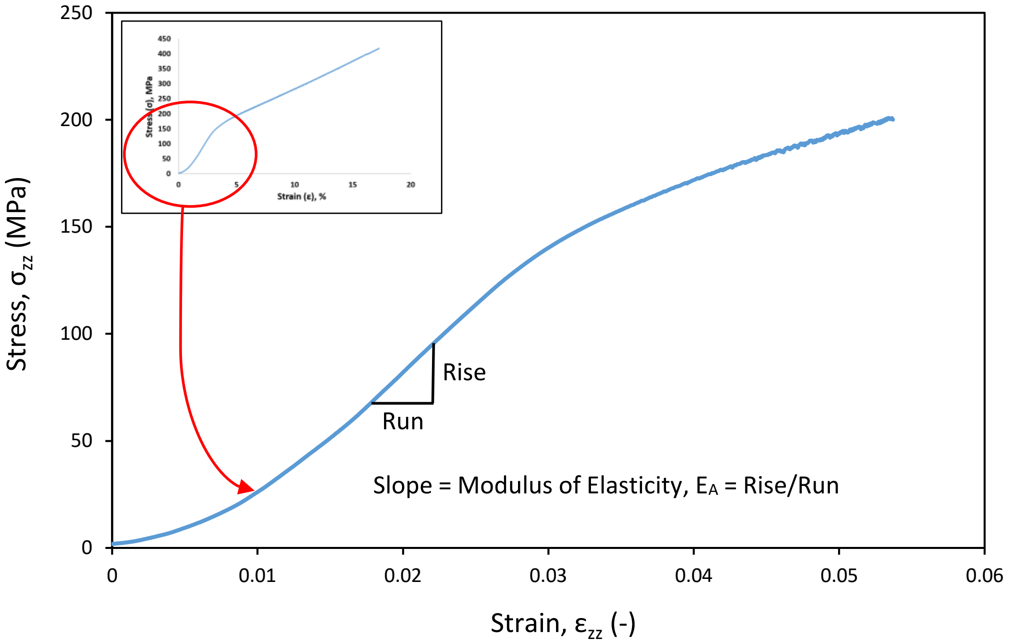

Fig. 5.37: Stress-strain behavior in elastic range for uniaxial compression of fourth specimen of the investigated Fe-SMA at 400°C

All the obtained results of uniaxial compression of fourth specimen at 400°C, are tabularized in Table 5.25.

Table 5.25
The investigated mechanical properties for Fe-SMA of interest at 400°C (fourth specimen)

Sr. #	**Mechanical property**	**Value**
1	Yield Strength, σ_y	145 MPa
2	Elastic strain, $\varepsilon_{e,\,zz}$	3.4%
3	Total axial compressive strain	17.38%
4	Modulus of elasticity, E_A	4600 MPa
5	Axial plastic strain, $\varepsilon_{p,\,zz}$	14.53%
6	Axial strain recovered	2.85%

5.4.5 The force-deformation behaviors at different temperatures

The results mentioned in Fig. 5.25, Fig. 5.28, Fig. 5.32, and Fig. 5.35 are combined in Fig. 5.38. It can be observed from Fig. 5.38 that value of the required force for phase transformation decreases by increasing the temperature.

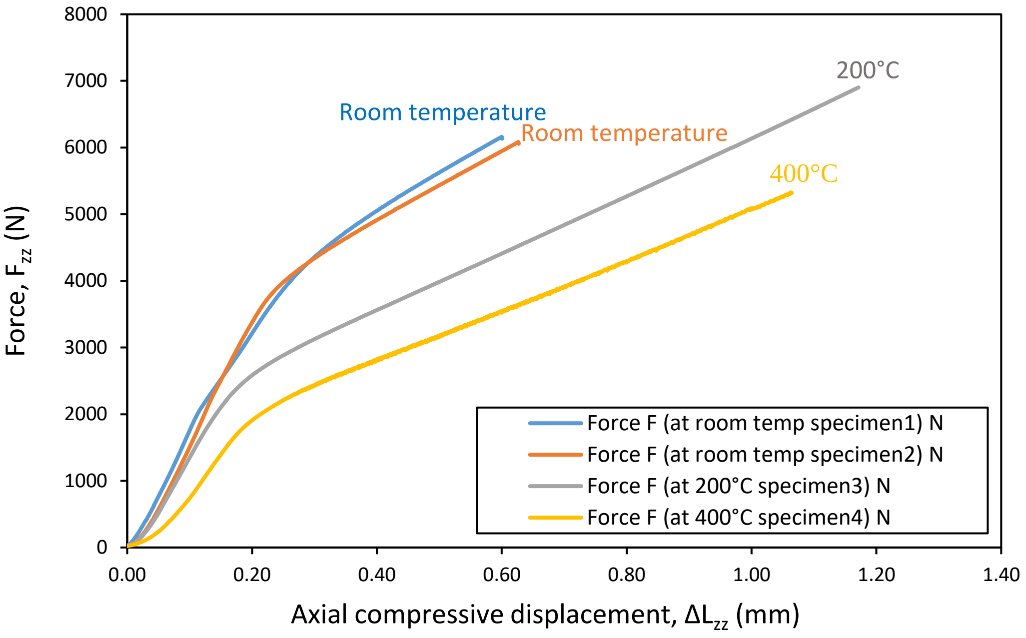

Fig. 5.38: Force-deformation behavior for uniaxial compression of four specimens of the investigated Fe-SMA at room temperature and elevated temperatures

5.4.6 Effect of temperature on the onset transformation stress

The results of stress-strain behavior mentioned in Fig. 5.26, Fig. 5.29, Fig. 5.33, and Fig. 5.36 are combined in the following Fig. 5.39 which shows the stress-strain responses for the investigated Fe-SMA, as a function of temperature. The results of four uniaxial compression tests are mentioned in Fig. 5.39 in order to see the effect of temperature on the onset transformation stress. The results illustrate that the transformation mechanism is temperature dependent. It can be observed that the plateau concerning the transformation onset stress (austenite to martensite transformation onset, σ_{AM}) decreases by increasing the temperature. In fact, bonding strength decreases by increasing the temperature. The vibration of atoms increases by increasing the temperature, consequently, atomic distance in crystal structure increases so atomic force decreases. As ductility increases commonly by increasing the temperature, therefore, a material fabricator wishes to deform a material at high temperature (hot working) to take the advantage of lower required stress as well as higher ductility.

It has also been observed by Fig. 5.26, Fig. 5.29, Fig. 5.33, and Fig. 5.36 (by Table 5.22 to Table 5.25 too) that elastic strain, $\varepsilon_{e,\,zz}$ as well as axial plastic strain, $\varepsilon_{p,\,zz}$ for investigated Fe-SMA increase by increasing the temperature from room temperature to 200°C, however, there is almost no increase from 200°C to 400°C.

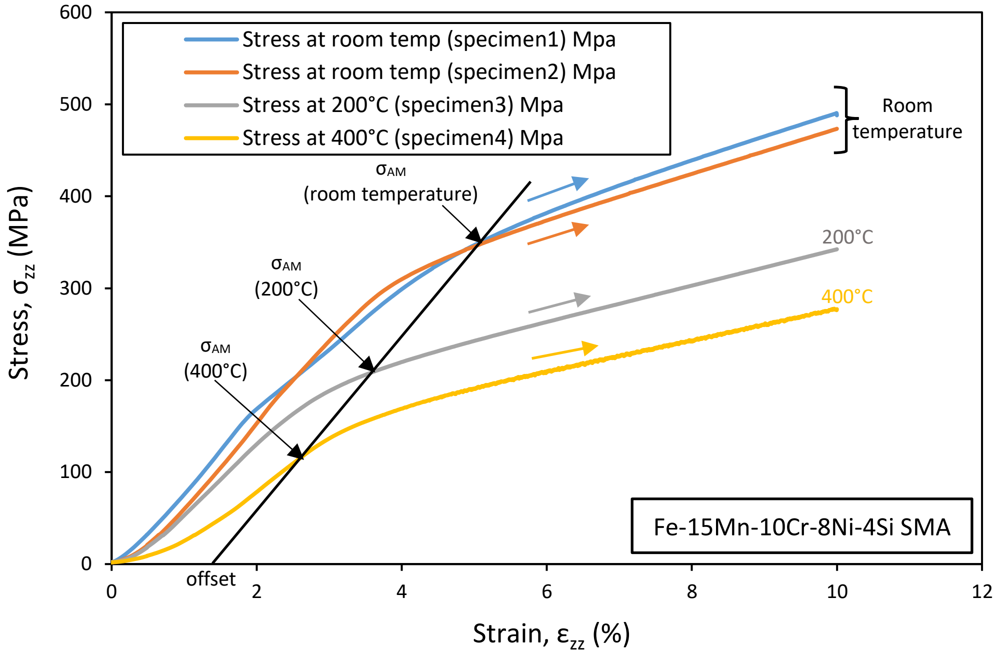

Fig. 5.39: Stress-strain curves for the investigated Fe-SMA at different temperatures under uniaxial compression tests

The σ_{AM}(20°C) is about 340 MPa, σ_{AM}(200°C) is about 190 MPa and σ_{AM}(400°C) is about 110 MPa as shown in Fig. 5.39. Now, (i) the difference of stress between 20°C and 200°C (200°C – 20°C = 180°C difference) is 340 - 190 = 150 MPa, therefore, the decrease rate of transformation onset stress between 20°C and 200°C is ≈80 MPa/100°C, (ii) the difference of stress between 200°C and 400°C (400°C – 200°C = 200°C difference) is 190 - 110 = 80 MPa, therefore, the decrease rate of transformation onset stress between 200°C and 400°C is ≈40 MPa/100°C, and (iii) the difference of stress between 20°C and 400°C (400°C – 20°C = 380°C) is 340 - 110 = 230 MPa, therefore, the decrease rate of transformation onset stress between 20°C and 400°C is ≈60 MPa/100°C which is the average value; as shown in Fig. 5.40.

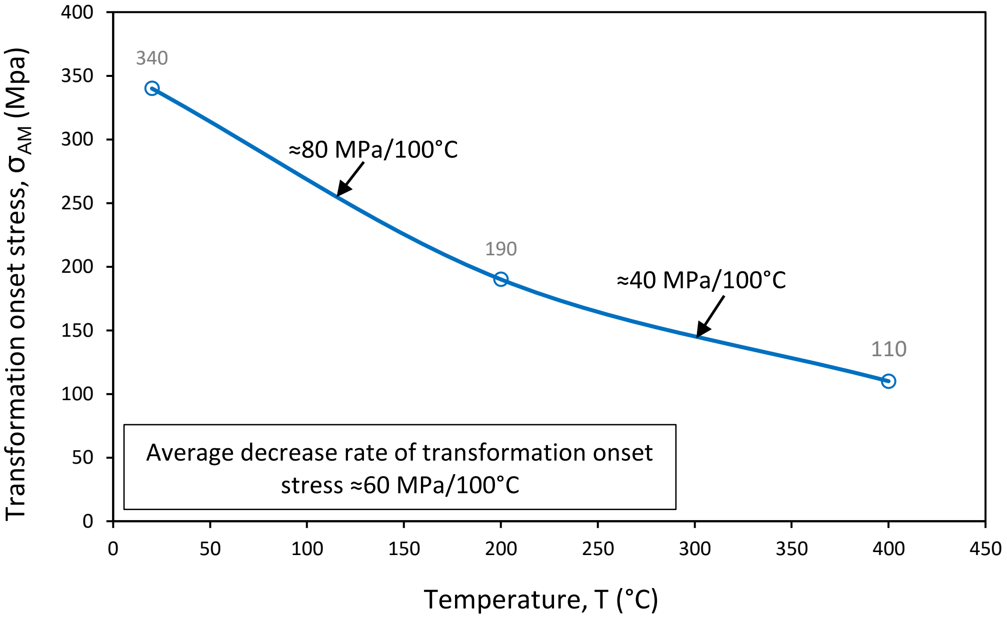

Fig. 5.40: Transformation onset stress-temperature diagram for the investigated Fe-SMA under uniaxial compression tests

5.4.7 Effect of temperature on modulus of elasticity of investigated Fe-SMA

The results related to stress-strain behavior in elastic range mentioned in Fig. 5.27, Fig. 5.30, Fig. 5.34, and Fig. 5.37 are combined in the following Fig. 5.41 which shows that modulus of elasticity, E_A decreases by increasing the temperature (with an average decrease rate of 900MPa/100°C as illustrated below). The XRD results have shown that ά-martensite (bcc) phase also exists at room temperature, however, there exists only γ-austenitic (fcc) phase at higher temperatures. Consequently, it can be concluded that the martensitic modulus of elasticity (E_M) is less than austenitic modulus of elasticity (E_A) i.e. $E_M < E_A$.

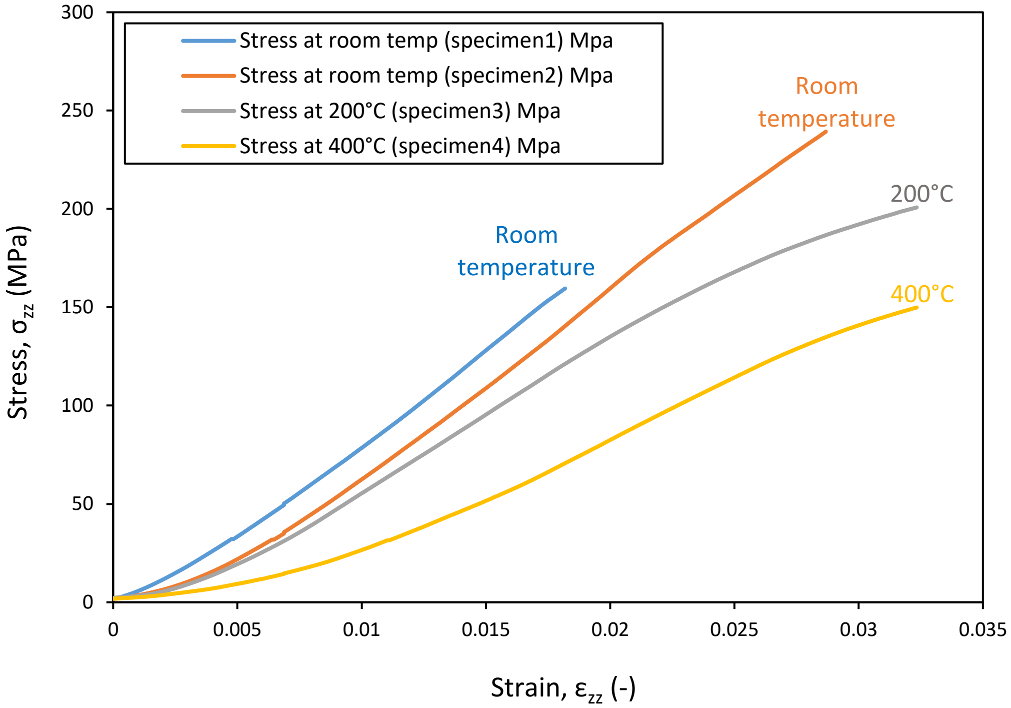

Fig. 5.41: Stress-strain behavior in elastic range of uniaxial compression for four specimens of the investigated Fe-SMA at different temperatures

In order to find out the decrease rate of modulus of elasticity, E_A with temperature, the below-mentioned Fig. 5.42 is drawn. It shows that the decrease rate during temperature difference of 180°C (20°C to 200°C) is 1300 MPa so decrease rate comes out as 720 MPa/100°C whereas the decrease rate during temperature difference of 200°C (200°C to 400°C) is 2100 MPa therefore decrease rate is 1050 MPa/100°C; as shown in Fig. 5.42. The overall decrease rate 20°C to 400°C comes out as ≈900 MPa/100°C.

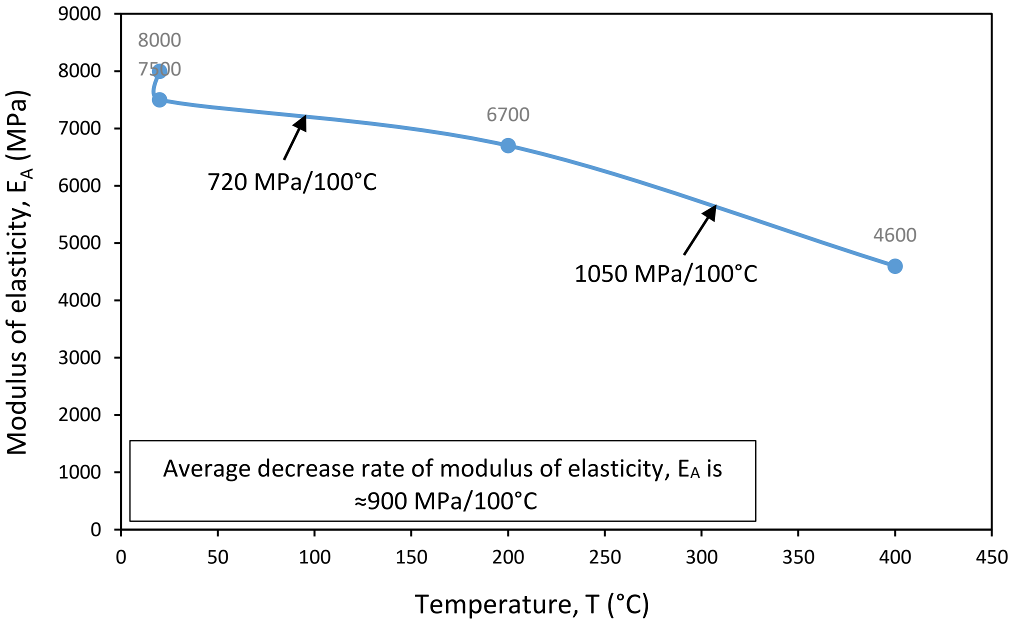

Fig. 5.42: Modulus of elasticity-temperature diagram for the investigated Fe-SMA under uniaxial compression tests

5.4.8 Effect of temperature on yield strength of investigated Fe-SMA

The yield strength usually decreases by increasing the temperature. In order to analyze the effect of temperature on yield strength, σ_y of the investigated Fe-SMA, the below-mentioned Fig. 5.43 is drawn. It has been observed that there is very slight increase of yield stress, σ_y from room temperature to 200°C, however, it decreases from 200°C to 400°C. The yield stress, σ_y decreases to 45 MPa during temperature difference of 200°C (200°C to 400°C) so decrease rate comes out as 22.5 MPa/100°C.

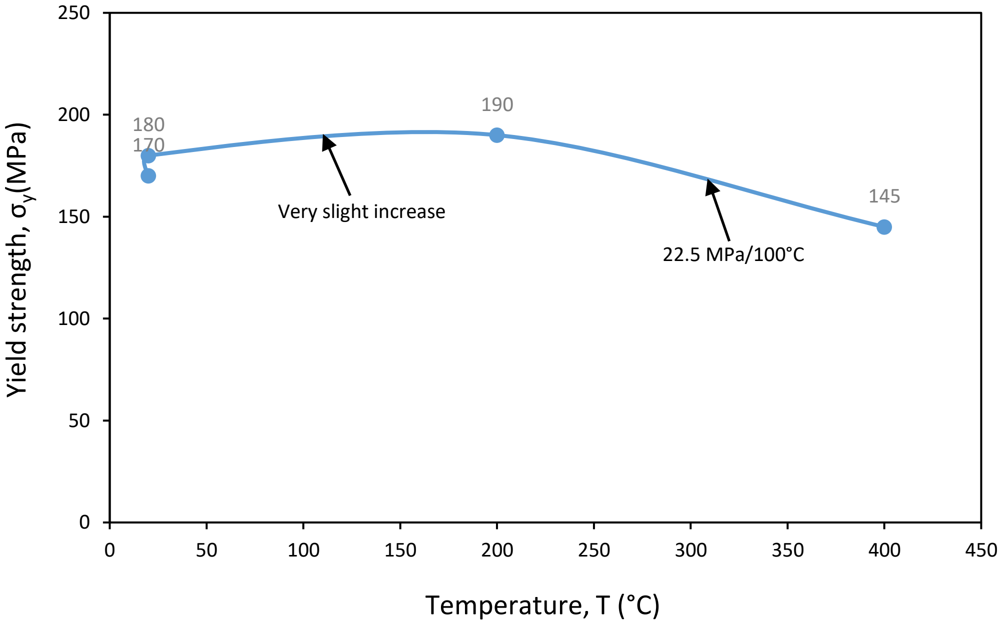

Fig. 5.43: Yield strength-temperature diagram for the investigated Fe-SMA under uniaxial compression tests

The ultimate compressive strength σ_{uts} is not possible to be calculated because the specimen is not broken.

5.5 Biaxial compression analysis at room temperature

In this section, a short explanation of the execution is given that biaxial compressive (2D) test is to load a (4.2mm x 4.2mm x 1mm) sample of investigated Fe-SMA in compression along two perpendicular directions (x- and y-axis as shown in Fig. 5.44). The main difficulty in this test is to apply the uniform load on each face of the sample with no friction between experimental setup and sample. Load is transferred from four plungers (shown in Fig. 5.45) of biaxial testing machine to four faces (shown in Fig. 5.44) of the sample.

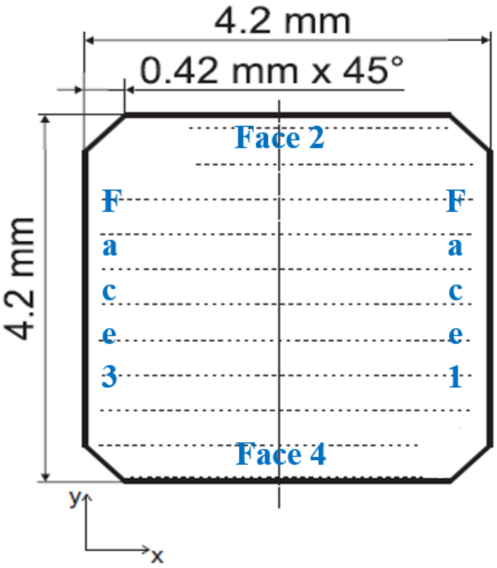

Fig. 5.44: Different faces of biaxial compression sample

Moreover, all the reported strains in these experiments are measured with strain gauges as shown in Fig. 5.45. All the four plungers move simultaneously with a speed of 1 mm/min (1.67×10^{-2} mm/s) during loading as well as unloading. The sample has been loaded equally in each direction as shown in Fig. 5.45, afterwards, four plungers along both axes (x- and y-axis) are driven back by unloading until the force reaches zero. At first, the forces and displacements on each face of the sample are measured during loading and unloading.

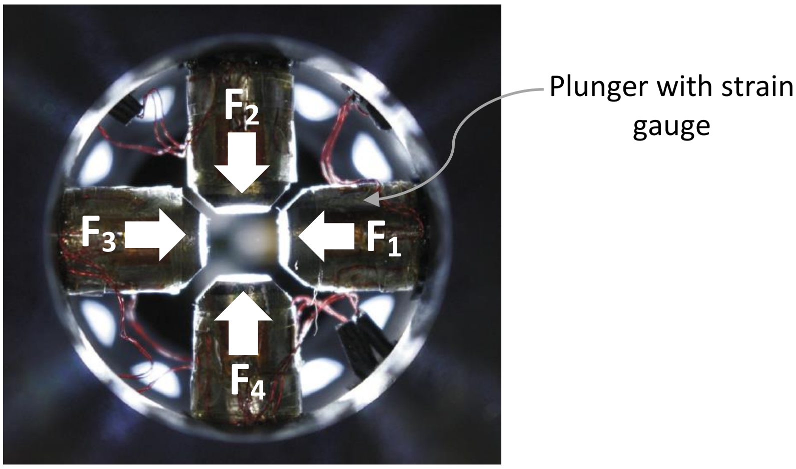

Fig. 5.45: Biaxial compression of the sample along two perpendicular directions [119]

All the experiments performed under section 5.5 are displacement controlled, therefore, there is a displacement of 0.07mm on each face of the sample with biaxial compression. The maximum displacement of each face of the sample after compression is 0.07mm which is 1.67% of 4.2mm. Therefore, the movement of opposite plungers went up to a maximum strain of 3.34% (strain along each axis) during loading because $\varepsilon = \Delta L/L*100$.

In this work of biaxial compression loading, the force components are denoted by F_1, F_2, F_3 and F_4 on face 1, face 2, face 3 and face 4 respectively, the displacements are denoted by S_1, S_2, S_3 and S_4 on face 1, face 2, face 3 and face 4 respectively, the stress components are denoted by σ_{xx} and σ_{yy} in x- and y-directions respectively, whereas the strain components are denoted by ε_{xx} and ε_{yy} in x- and y-directions respectively.

5.5.1 Force-deformation behavior of investigated Fe-SMA during biaxial compression at room temperature

As discussed earlier that biaxial experiments are displacement controlled, therefore, the compressive displacement, S_1 on face 1 (shown in Fig. 5.44) of the sample at different values of force, F_1 applied on the said face is shown in Fig. 5.46 which shows that during loading of face 1 the maximum displacement is reached to 0.07mm which remains 0.035mm when the sample expands on unloading. There is a compressive force corresponding to the displacement followed by unloading until the force reaches zero. Besides, it is not possible to go from point D to point A (coming back to original shape) because there is no force anymore, it has already become zero at point D due to no more contact of plungers with sample.

The peak/peaks before σ_s in Fig. 5.54 and Fig. 5.56 to Fig. 5.58 (which are stress-strain diagrams of face 1 to face 4 thus correspond to Fig. 5.46 to Fig. 5.49 respectively) might be due to the presence of ά-martensite phase (bcc) in the investigated Fe-SMA as shown in Fig. 5.46 to Fig. 5.49 too.

There are small acceptable lines in the microstructure of the investigated Fe-SMA shown in Fig. 5.55 which are due to grinding of the material. Unlike fine-grained microstructures, the coarse-grained microstructures have fewer, and larger discrete components. A coarse-grained description also concerns to large subcomponents. The investigated Fe-SMA has been produced by arc melting which is a type of casting. The microstructure of casted alloy is much coarser like that of the material used in this thesis. A homogeneous material means a material which has uniform microstructure, and uniform properties throughout. In the best case there should be homogeneous alloy comprising of same grains throughout without having subgrains. However, the microstructure of the investigated Fe-SMA shows that it is inhomogeneous because it is very coarse microstructure. There is not only the Christmas tree but also the grains in microstructure. Besides, there are also small subgrains inside the grains. This is possibly the reason of tilting the curves especially at point C as shown in Fig. 5.46 to Fig. 5.49.

However, the stress-strain diagrams shown in Fig. 5.54, Fig. 5.56, Fig. 5.57, Fig. 5.58, Fig. 5.59 are better for further elaboration of the below-mentioned force-deformation diagrams (Fig. 5.46 to Fig. 5.49).

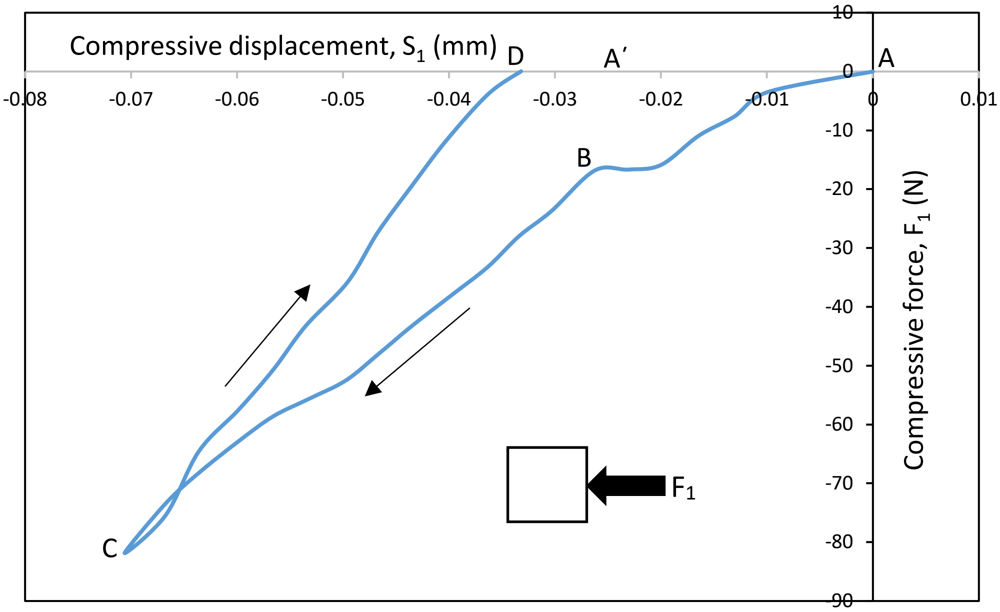

Fig. 5.46: Force-deformation behavior of face 1 of the sample during loading and unloading under equibiaxial compression at room temperature

The compressive displacement, S_2 on face 2 (shown in Fig. 5.44) of the sample at different values of force, F_2 applied on the said face is shown in Fig. 5.47 which shows that during loading of face 2 the maximum displacement is reached to 0.07mm which remains 0.028mm when the sample expands on unloading.

Besides, Fig. 5.46 to Fig. 5.49 show that the specimen comes into full contact with plunger when the point A′ (0.024mm) reaches. In other words, all the faces of specimen are finally loaded at point A′, therefore, further elaboration in the respective stress-strain diagrams is from A′ onwards.

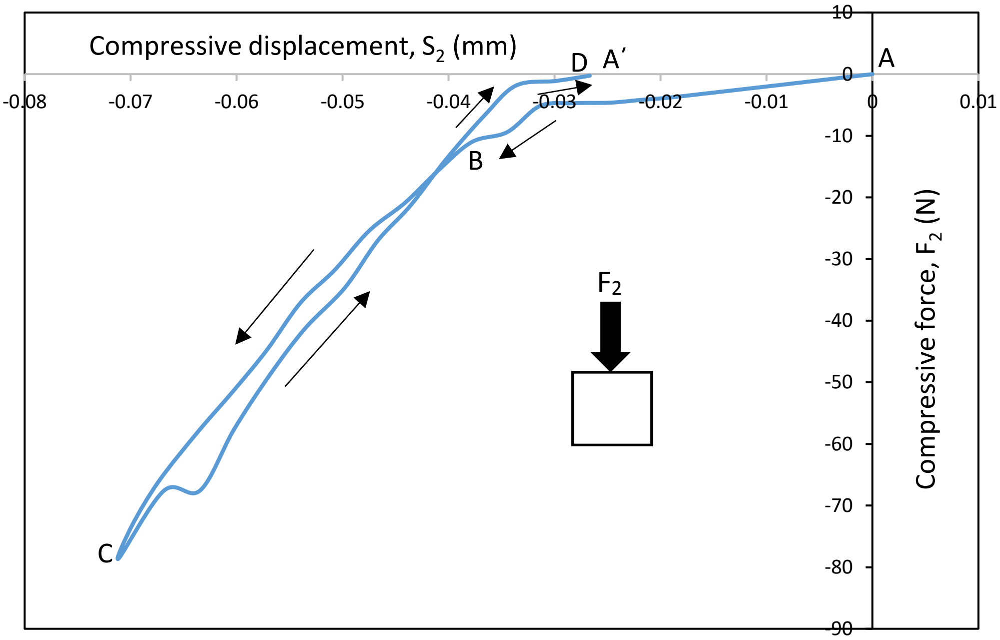

Fig. 5.47: Force-deformation behavior of face 2 of the sample during loading and unloading under equibiaxial compression at room temperature

The compressive displacement, S_3 on face 3 (shown in Fig. 5.44) of the sample at different values of force, F_3 applied on the said face is shown in Fig. 5.48 which shows that during loading of face 3 the maximum displacement is reached to 0.07mm which remains 0.028mm when the sample expands on unloading.

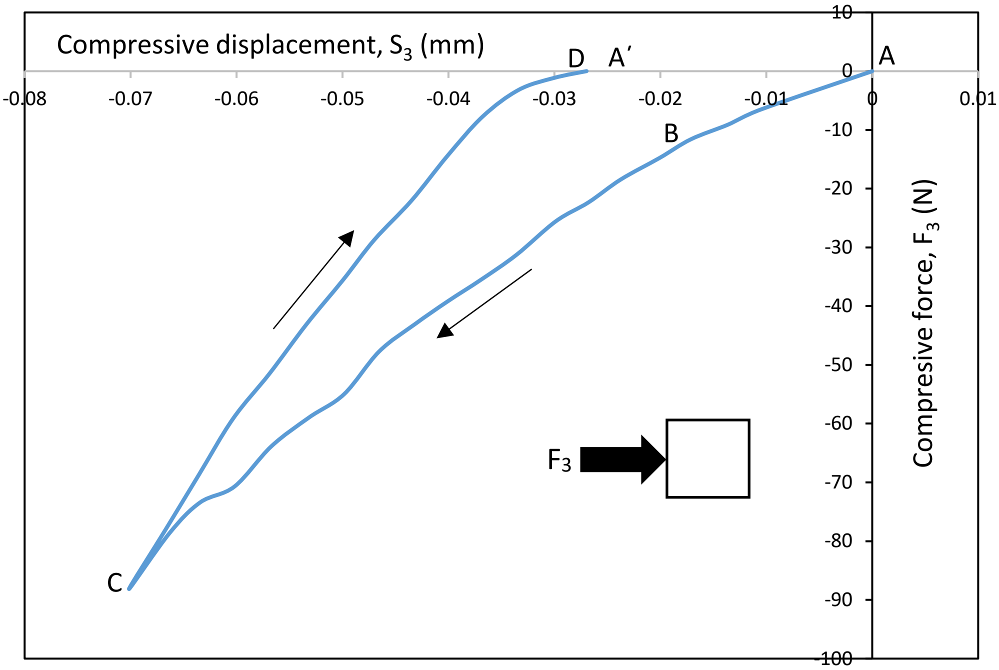

Fig. 5.48: Force-deformation behavior of face 3 of the sample during loading and unloading under equibiaxial compression at room temperature

The compressive displacement, S_4 on face 4 (shown in Fig. 5.44) of the sample at different values of force, F_4 applied on the said face is shown in Fig. 5.49 which shows that during loading of face 4 the maximum displacement is reached to 0.07mm which remains 0.035mm when the sample expands on unloading.

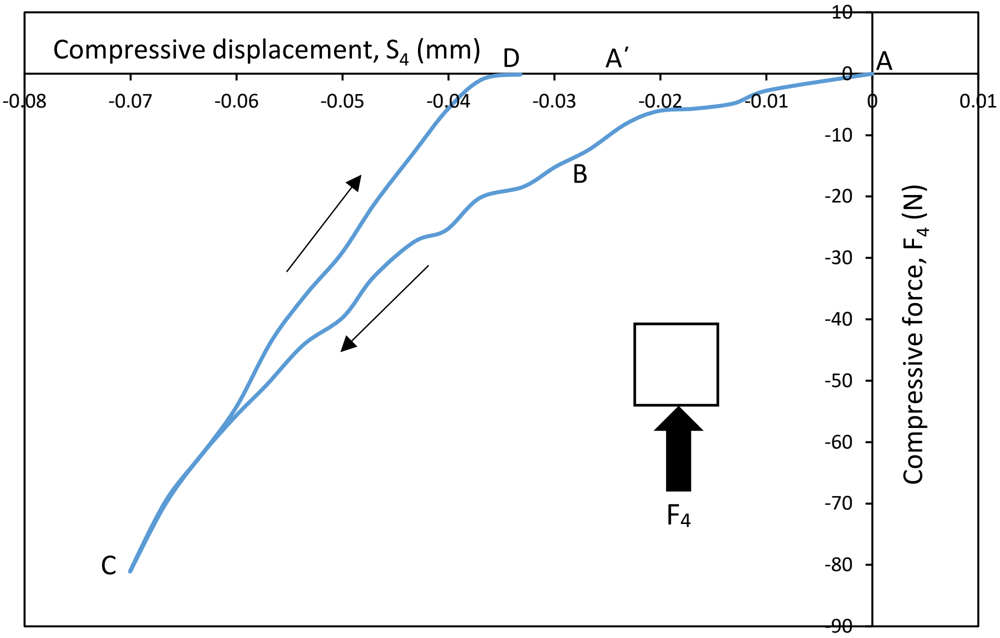

Fig. 5.49: Force-deformation behavior of face 4 of the sample during loading and unloading under equibiaxial compression at room temperature

5.5.2 Force-deformation-time behavior of investigated Fe-SMA during biaxial compression at room temperature

Fig. 5.50 to Fig. 5.53 show the force-deformation-time behavior during displacement-controlled loading and unloading of different faces of the sample under equibiaxial compression at room temperature. In fact, the orange curve shows the behavior between compressive force and time, whereas the blue curve shows the behavior between compressive displacement and time.

The sample is loaded at a loading speed of 1.67x10^{-2} mm/s by applying compressive force F_1 on face 1 (shown in Fig. 5.44) followed by unloading until the force reaches zero as shown by orange curve of Fig. 5.50. The compressive displacement, S_1 on face 1 reaches at a maximum value of 0.07mm by applying the force on that face, after that, unloading starts and the material expands; as shown by blue curve of Fig. 5.50. It also shows that the compressive force, F_1 becomes zero but the material does not reach to its initial state so far.

The microstructure of the investigated Fe-SMA shown in Fig. 5.55 is very complex. The SEM-EDS analysis shows that there are five elements in the alloy as well as some impurities like S and Se as shown in Fig. 5.10, however, there is no carbon. The material behavior depends on the distribution of these elements which causes waviness of the data shown in Fig. 5.50 to Fig. 5.53 because they become hurdle in the way of free dislocation motion.

As stress-strain-time response gives the complete picture of the mechanical behavior of the material, therefore, the stress-strain-time diagrams will be better for further interpretation of force-deformation-time behaviors.

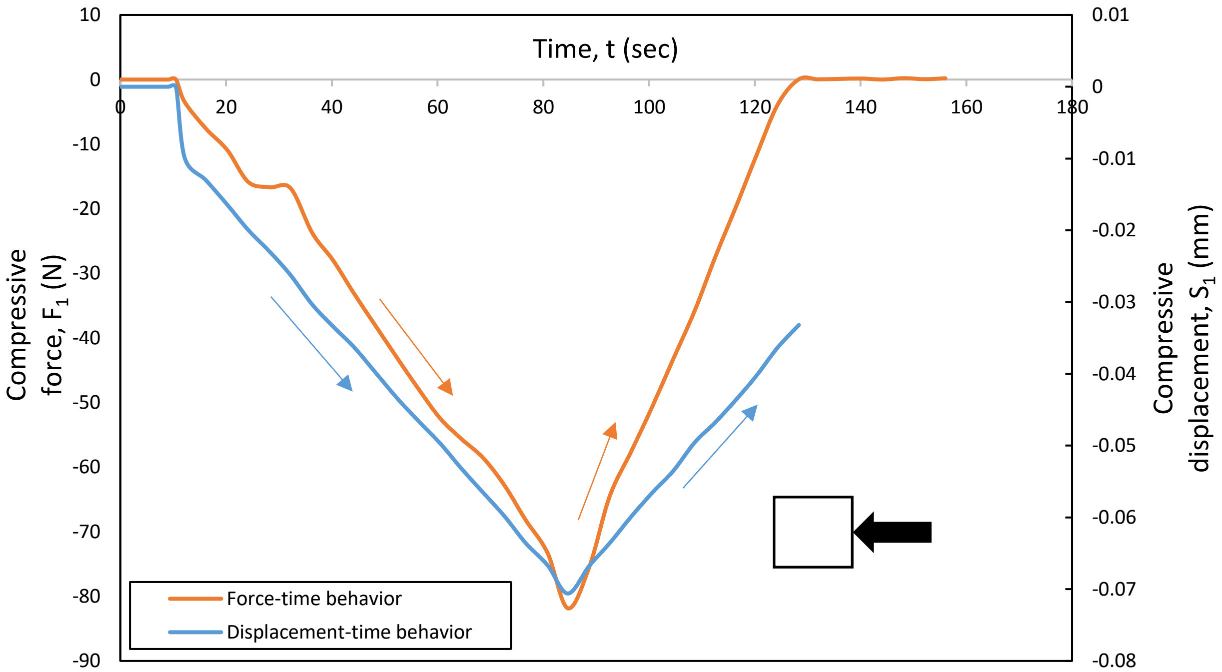

Fig. 5.50: Force-deformation-time behavior of face 1 of the sample during loading and unloading under equibiaxial compression at room temperature

The force-deformation-time diagram during displacement-controlled loading and unloading of face 2 of the sample is described in Fig. 5.51.

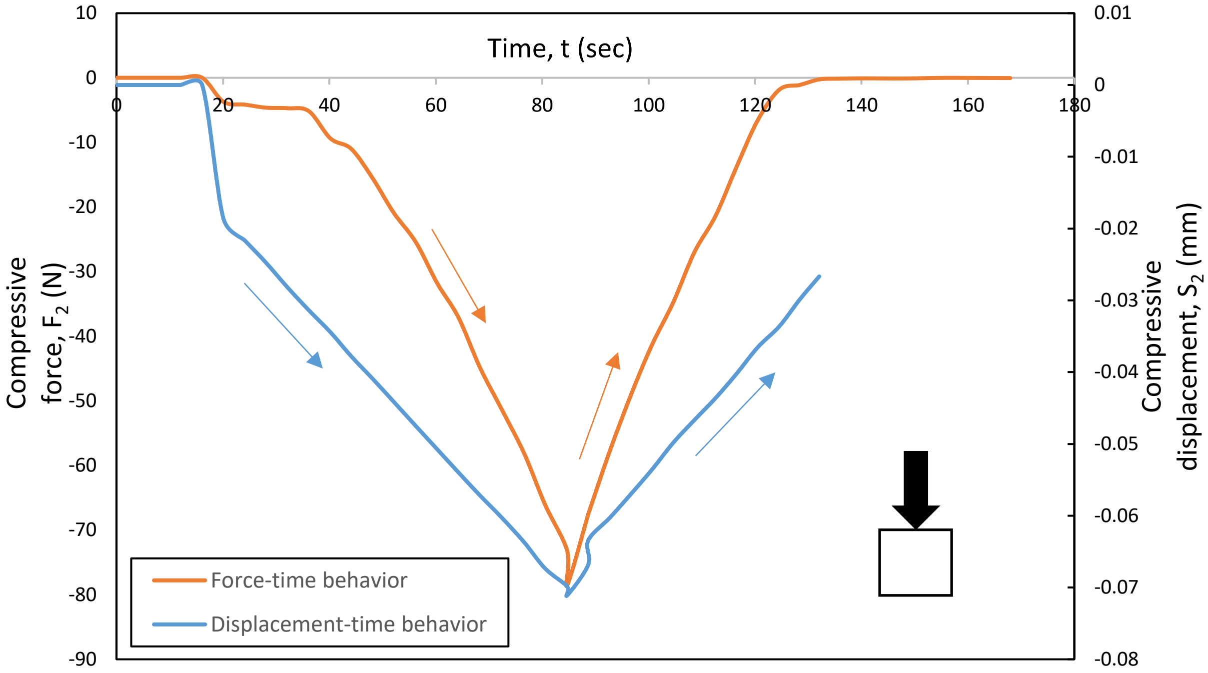

Fig. 5.51: Force-deformation-time behavior of face 2 of the sample during loading and unloading under equibiaxial compression at room temperature

The force-deformation-time diagram during displacement-controlled loading and unloading of face 3 of the sample is described in Fig. 5.52.

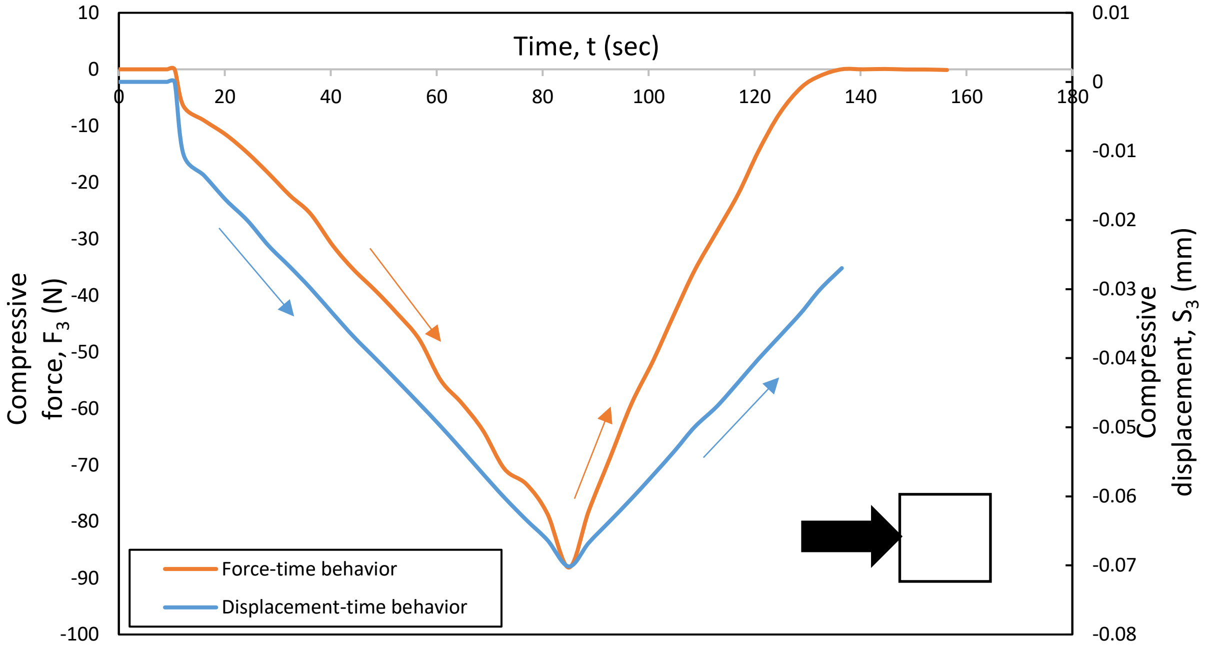

Fig. 5.52: Force-deformation-time behavior of face 3 of the sample during loading and unloading under equibiaxial compression at room temperature

The force-deformation-time diagram during displacement-controlled loading and unloading of face 4 of the sample is described in Fig. 5.53.

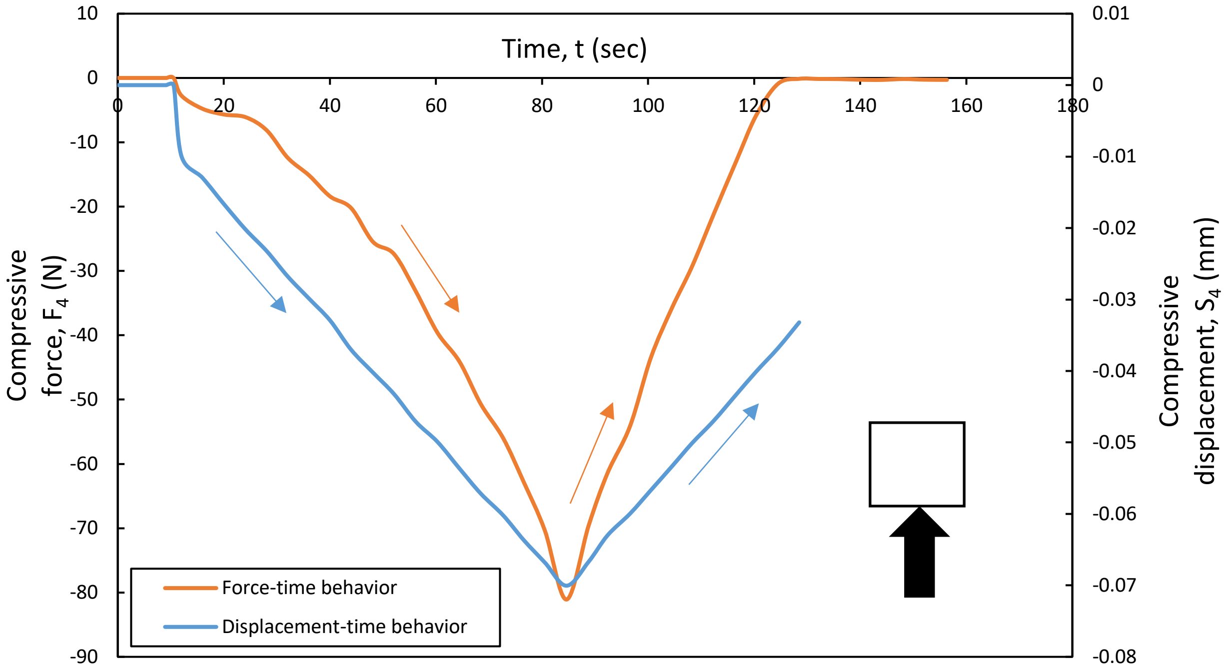

Fig. 5.53: Force-deformation-time behavior of face 4 of the sample during loading and unloading under equibiaxial compression at room temperature

5.5.3 Stress-strain behavior of investigated Fe-SMA during biaxial compression at room temperature

The nominal compressive stress plotted in Fig. 5.54, Fig. 5.56, Fig. 5.57, Fig. 5.58, and Fig. 5.59 has been calculated by means of σ = F/A, where F is the compressive force in N mentioned in Fig. 5.46 to Fig. 5.53 whereas A is the initial face area (3.36mm x 1mm) in mm^2 of square sheet sample. The unit of stress is therefore N/mm^2 (MPa).

Hence,

$$\sigma_{xx} = \frac{Fx}{A} \tag{5.11}$$

and

$$\sigma_{yy} = \frac{Fy}{A} \tag{5.12}$$

where

F_x	force along x-axis (like F_1 on face 1 and F_3 on face 3)
F_y	force along y-axis (like F_2 on face 2 and F_4 on face 4)
A	initial face area of the sample

The strain has been calculated by means of ε = ΔL/L*100, where ΔL is the compressive displacement mentioned in Fig. 5.46 to Fig. 5.53 whereas L is the total length (4.2mm) of square sheet sample.

The Fe-SMAs consist of three martensitic variants named according to the direction of their axis. If axis of a variant is parallel to x-axis, it is called variant type 1, similarly the axes of variant type 2 and variant type 3 are parallel to y-axis and z-axis, respectively. The variants reorient when force is applied until their axes become parallel to the stress direction, it is called as variant reorientation [120][121][122].

An inelastic deformation can be defined as if an object is stretched beyond its elastic limit and the object shrinks after removing the applied force however not return to its original size. The nominal stress-strain diagram for face 1 of the sample is plotted in Fig. 5.54. There is an elastic strain (A → B) until σ_s reaches. This σ_s shows the start of martensitic variants. It also shows the start of γ-austenite (fcc) to ε-martensite (hcp) transformation. There is an inelastic response (B → C) due to formation and reorientation of variants which continues until σ_f reaches. Most probably, at σ_f the formation and reorientation of martensitic variants in the direction of force is completed showing austenite to martensite transformation, the martensite comprises of three variants over here. After σ_f the material did not show any elastic response like that of Nitinol, it is probably due to stress concentration because of contact stresses applied by plungers that pressurize the sample. Consequently, there comes again an inelastic response during unloading (without prior elastic response like that of Nitinol) which is attributed to dispersal of variants.

It has been reported if Fe-SMAs are subjected to biaxial compression with proper amounts of stresses, these materials can show pseudoelastic response. This pseudoelasticity is originated from variant reorientation while it is due to phase transformation in an SMA [123].

However, there is some residual strain, ε^r left inside the investigated Fe-SMA at point D shown in Fig. 5.54, which expresses the plastic deformation and unavailability of superelasticity at these deformation conditions because the material possesses certain amount of plasticity (at point D) due to stress until 24 MPa on face 1 (Fig. 5.54), 23 MPa on face 2 (Fig. 5.56), 26 MPa on face 3 (Fig. 5.57), and 24 MPa on face 4 (Fig. 5.58); which are probably high enough.

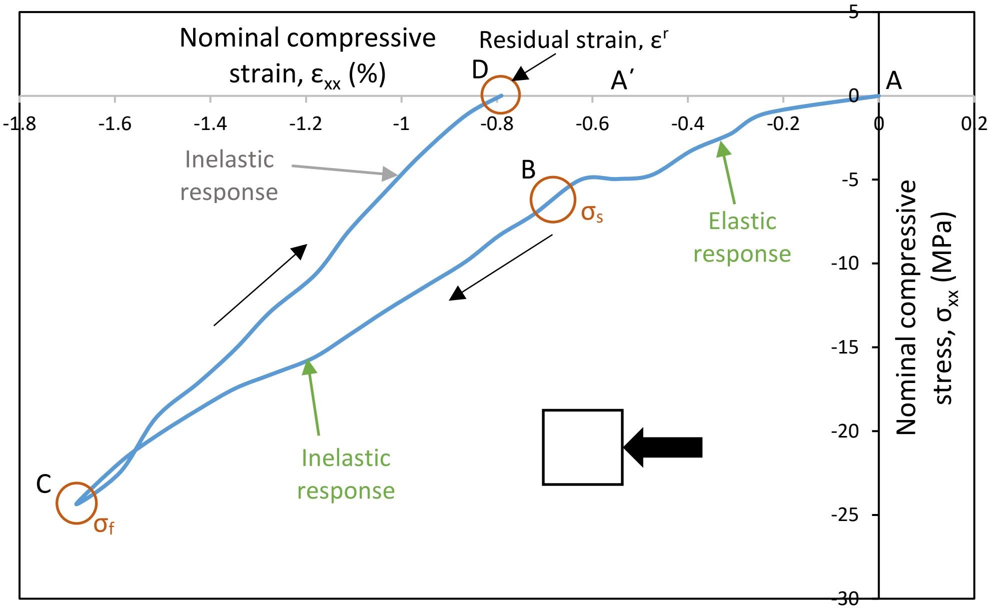

Fig. 5.54: Nominal stress-strain behavior of face 1 of the sample in (σ_{xx}–ε_{xx}) plane during loading and unloading under equibiaxial compression at room temperature

Along with Christmas tree structure, there are dark areas too describing two phases in the microstructure. These phases with different chemical compositions and different properties, behave differently. There can also be inhomogeneous redistributions of chemical composition inside the microstructure, causing inhomogeneous properties of the microstructure. It is possible that Christmas tree areas behave like superelastic material, but the phases in between cannot perform like this causing only TRIP (Transformation-Induced-Plasticity) effect producing residual strain. If phase distribution differs only 2 or 3% then it has no effect on behavior.

The biaxial compression behavior is sometimes different from uniaxial compression behavior. The yield point of investigated Fe-SMA in case of biaxial compression might be much lower thus the stresses here (24 MPa, 23 MPa, 26 MPa, and 24 MPa for face 1, face 2, face 3, and face 4 respectively) are far above the yield strength, consequently, no superelasticity at these deformation conditions is observed. In order to see the superelasticity the stress should have been much lower and there should have been an idea of the value of yield strength for investigated Fe-SMA prior to perform the biaxial test.

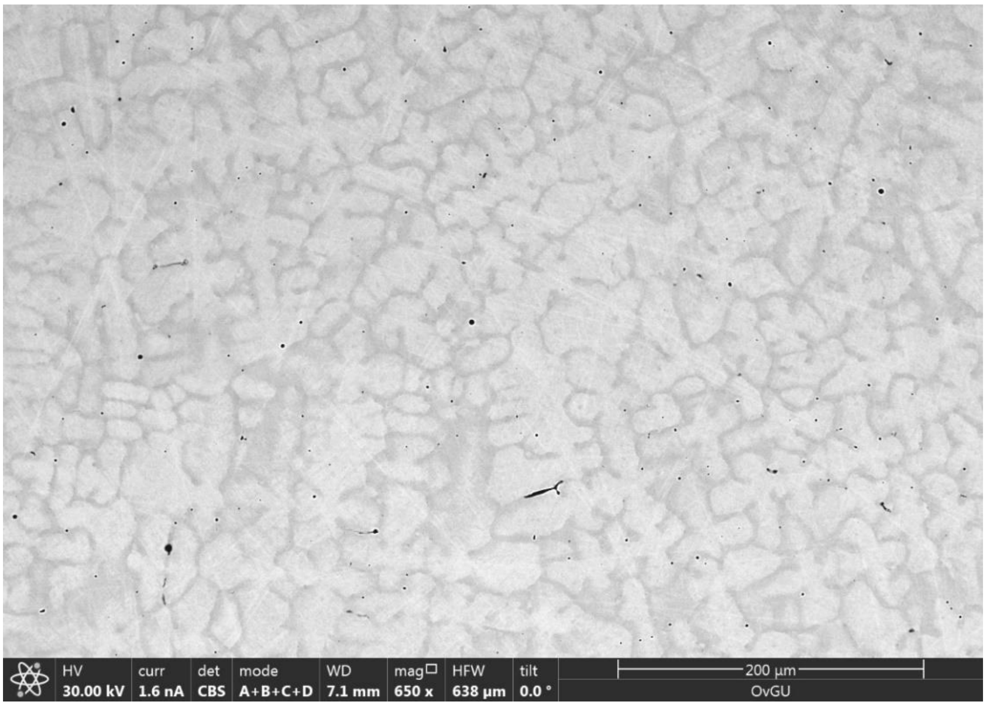

Fig. 5.55: SEM microstructure of the investigated Fe-SMA prior to biaxial compression deformation

A schematic stress-strain response for face 2 of the sample is plotted in Fig. 5.56 where the stress is applied vertically along y-axis. The response is quite different from that of other faces i.e. there is congested response over here. The mechanical behavior also depends upon the orientation of grains and their size. It is typical for casted alloys that there is no special orientation of the microstructure along both axes, therefore, the material properties are different in vertical direction than that of horizontal direction. By loading, the grains elongate along one of the two axes (x- and y-axis) and differ the mechanical properties along both axes due to change in grain size (grains are much longer along one of the two axes) as well as their orientation.

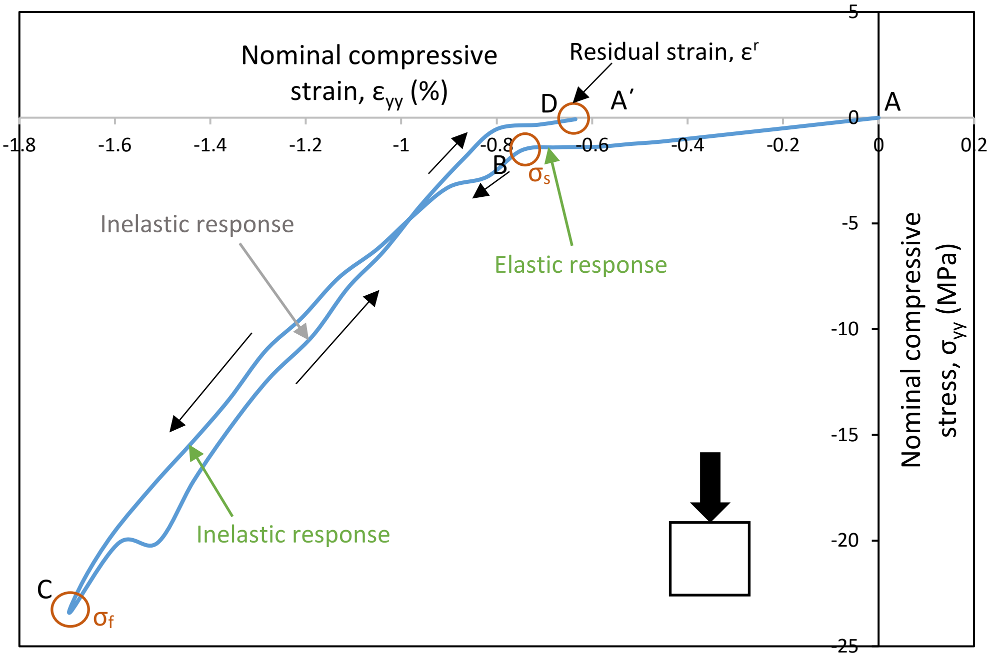

Fig. 5.56: Nominal stress-strain behavior of face 2 of the sample in (σ_{yy}–ε_{yy}) plane during loading and unloading under equibiaxial compression at room temperature

The nominal stress-strain diagram for face 3 of the sample is plotted in Fig. 5.57.

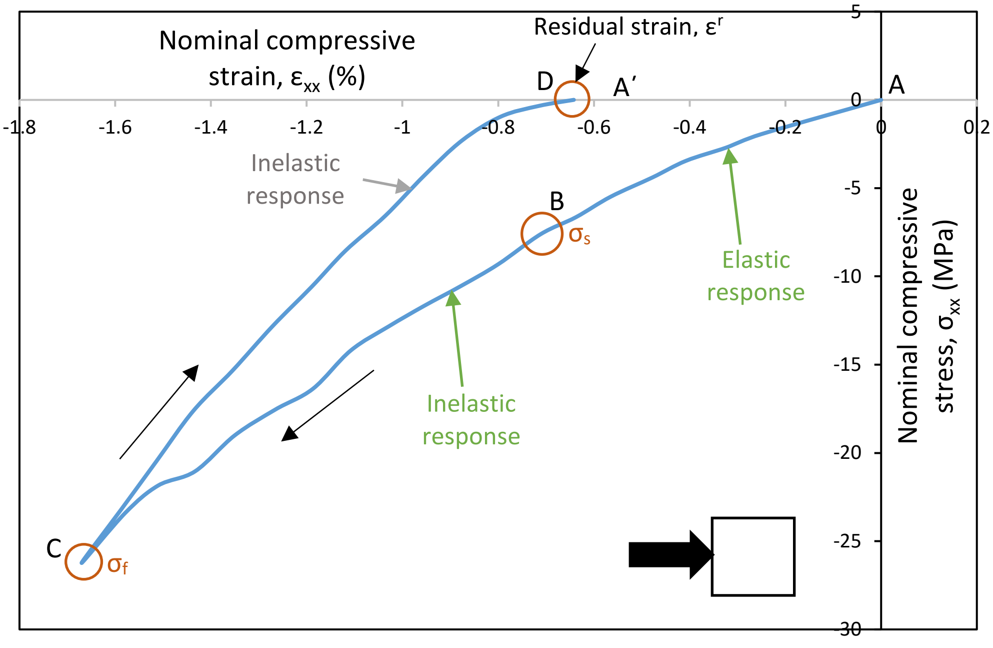

Fig. 5.57: Nominal stress-strain behavior of face 3 of the sample in (σ_{xx}–ε_{xx}) plane during loading and unloading under equibiaxial compression at room temperature

The nominal stress-strain diagram for face 4 of the sample is plotted in Fig. 5.58.

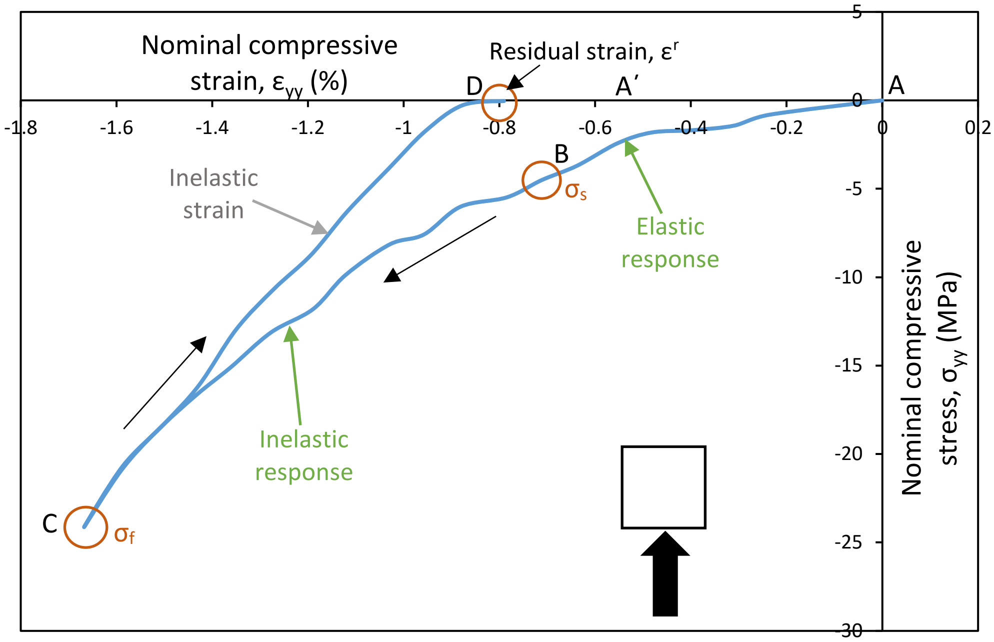

Fig. 5.58: Nominal stress-strain behavior of face 4 of the sample in (σ_{yy}–ε_{yy}) plane during loading and unloading under equibiaxial compression at room temperature

The results of Fig. 5.54, Fig. 5.56, Fig. 5.57, and Fig. 5.58 are combined in Fig. 5.59 which clearly differentiates the results along x-axis and y-axis. In Fig. 5.59 the solid lines show the stresses along x-axis (face 1 and face 3) whereas the dotted lines show the stresses along y-axis (face 2 and face 4). The comparison of these lines shows that solid lines and dotted lines are not overlapping, in other words, the mechanical behavior of the investigated Fe-SMA is not identical along two axes (i.e. x- and y-axis). Therefore, the investigated Fe-SMA shows the condition of asymmetry.

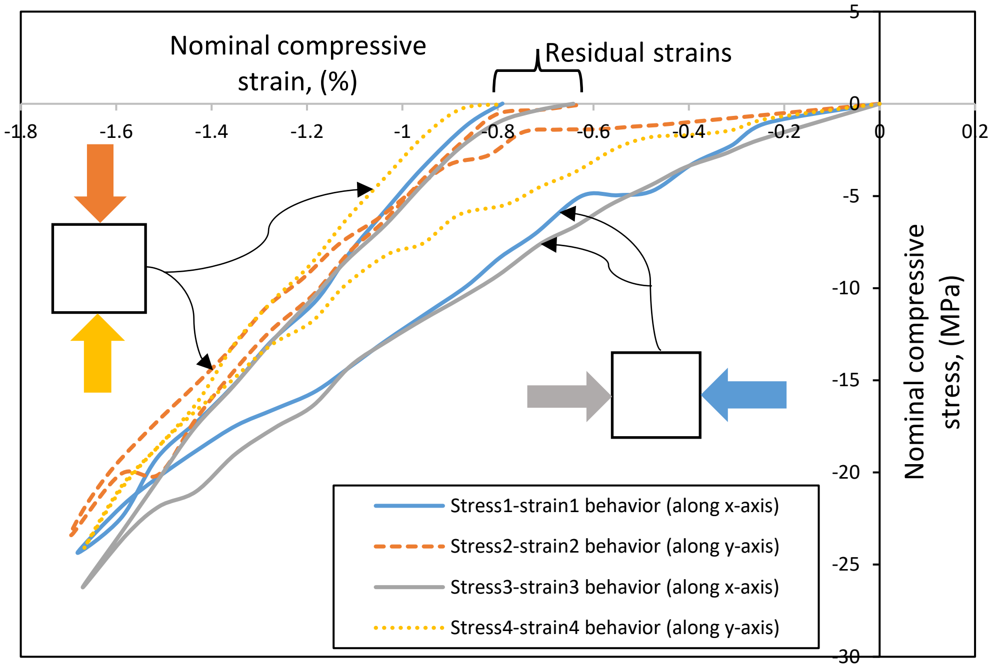

Fig. 5.59: Nominal stress-strain behavior of different faces of the sample in (σ_{yy}–ε_{yy}) plane during loading and unloading under equibiaxial compression at room temperature

5.5.4 Stress-strain-time behavior of investigated Fe-SMA during biaxial compression at room temperature

Fig. 5.60 to Fig. 5.63 show the stress-strain-time behavior of the investigated Fe-SMA during loading and unloading of different faces under equibiaxial compression at room temperature whereas Fig. 5.65 shows all in one. In fact, the orange curve in Fig. 5.60 to Fig. 5.63 shows the schematic stress-time response, whereas the blue curve in Fig. 5.60 to Fig. 5.63 shows the schematic strain-time response.

The stress-strain-time diagram for face 1 of the sample has been plotted in Fig. 5.60 which shows the nominal compressive stress, σ_{xx} increases due to loading followed by its decrease due to unloading until the stress reaches zero as shown by orange curve in Fig. 5.60, besides, the nominal compressive strain, ε_{xx} on the said face increases and reaches a maximum strain of 1.67% due to loading followed by its decrease due to expansion of material while unloading as shown by blue curve in Fig. 5.60.

It can be observed that σ_{xx} has become zero, however, the material does not reach to its initial state so far because all the oriented variants are no more oriented along x- and y-axis after unloading, consequently, there is residual strain describing plastic deformation.

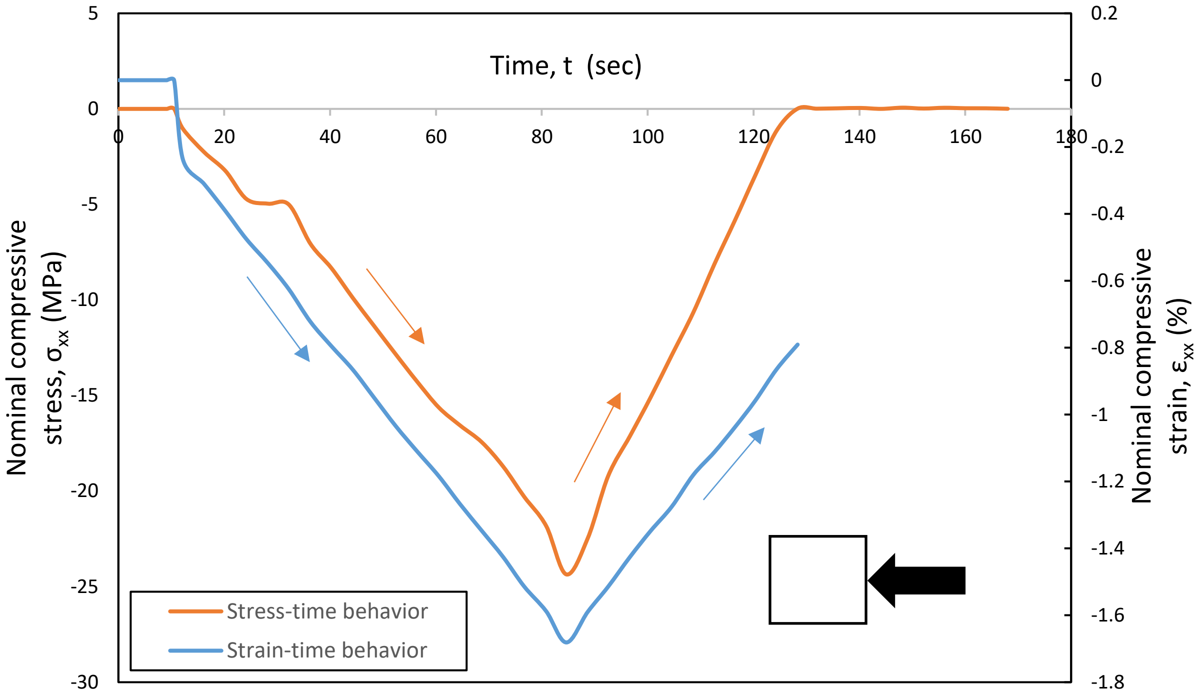

Fig. 5.60: Stress-strain-time behavior of face 1 of the sample during loading and unloading under equibiaxial compression at room temperature

The stress-strain-time diagram for face 2 of the sample has been plotted in Fig. 5.61.

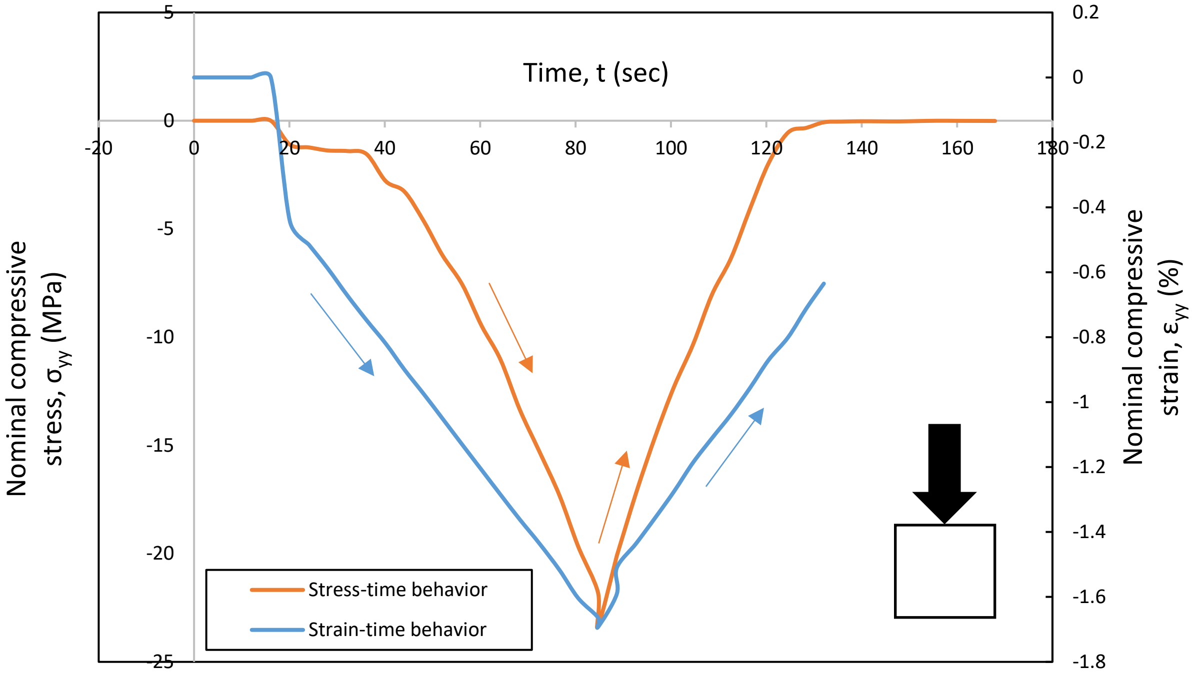

Fig. 5.61: Stress-strain-time behavior of face 2 of the sample during loading and unloading under equibiaxial compression at room temperature

The stress-strain-time diagram for face 3 of the sample has been plotted in Fig. 5.62.

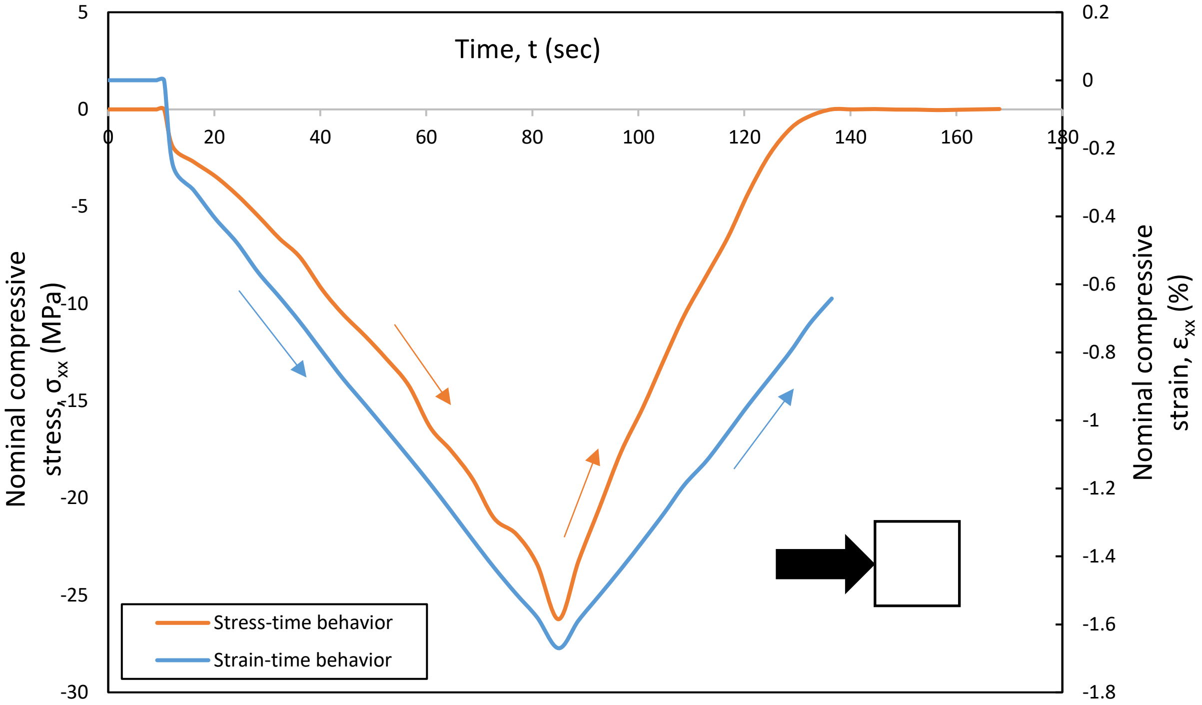

Fig. 5.62: Stress-strain-time behavior of face 3 of the sample during loading and unloading under equibiaxial compression at room temperature

The stress-strain-time diagram for face 4 of the sample has been plotted in Fig. 5.63.

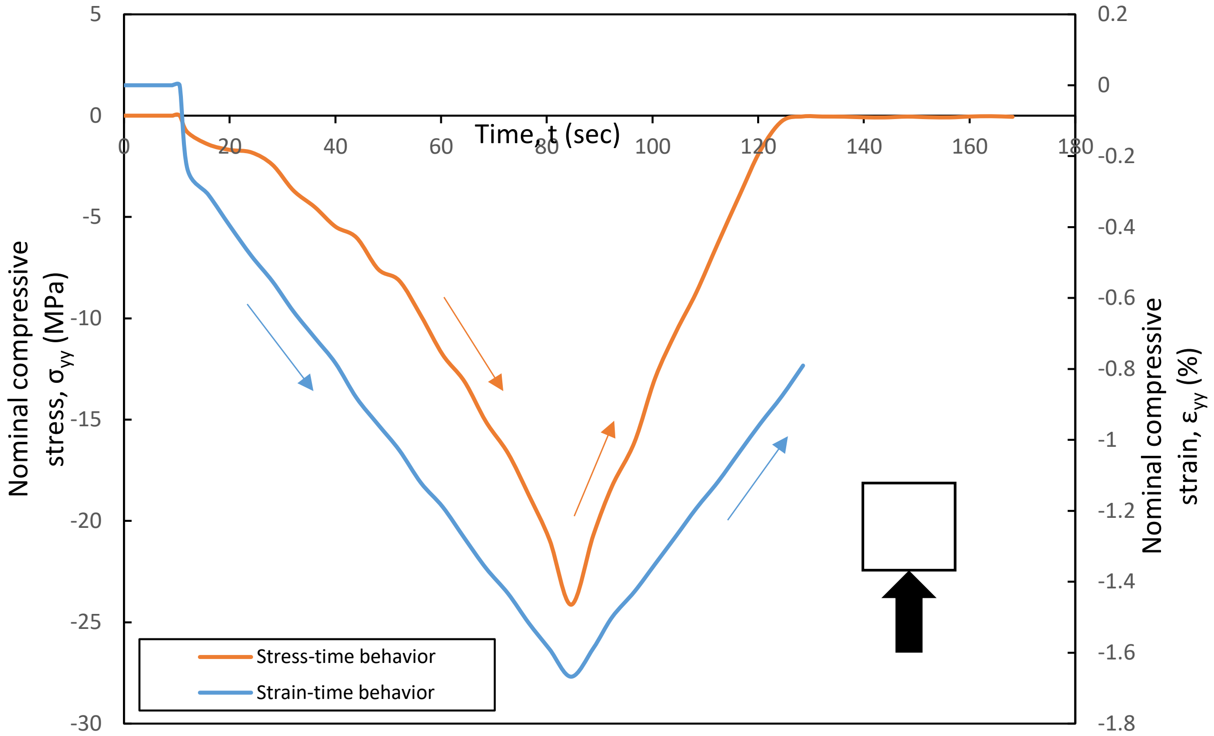

Fig. 5.63: Stress-strain-time behavior of face 4 of the sample during loading and unloading under equibiaxial compression at room temperature

The following Fig. 5.65 shows all the above-mentioned results of Fig. 5.60 to Fig. 5.63.

It can also be observed by Fig. 5.65 that the strain 1, strain 3 and strain 4 at face 1, face 3 and face 4 respectively are overlapping, however, the strain 2 at face 2 differs from all the other strains because mechanical behavior also depends upon the orientation of grains and their size. It is typical for casted alloys that there is no special orientation of the microstructure along both axes, therefore, the material properties are different in vertical direction than that of horizontal direction. By loading, the grains elongate along one of the two axes (x- and y-axis) and differ the mechanical properties along both axes due to change in grain size as well as their orientation.

Chen et al. performed biaxial (2D) compression experiments on $Ni_{50}Mn_{28.5}Ga_{21.5}$ shape memory alloy at room temperature and found the results as shown in the Fig. 5.64. It has been found that the selected material has ability to work at high stress levels (plateau stress > 12 MPa), which are much larger than the blocking stress (< 3 MPa) in 1D configuration. The findings indicate that the selected material can work at high stress levels as well as at multi-axial stresses [123].

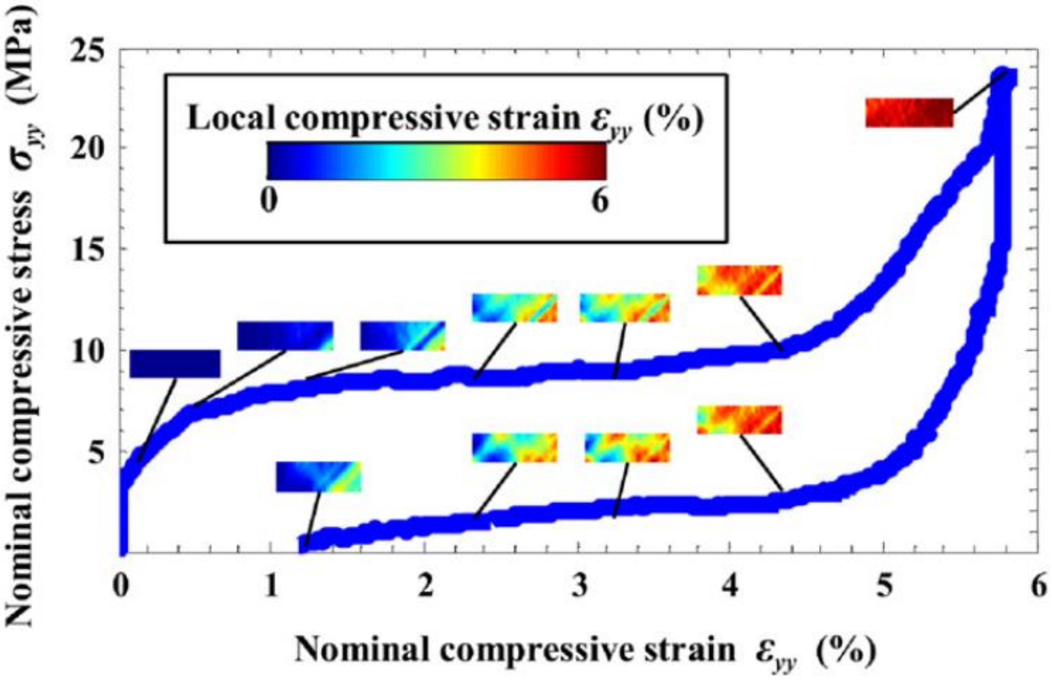

Fig. 5.64: Nominal stress-strain curve (σ_{yy}–ε_{yy}) of $Ni_{50}Mn_{28.5}Ga_{21.5}$ shape memory alloy during loading and unloading under biaxial compression at room temperature [123]

By observing Fig. 5.59 and Fig. 5.65, it can easily be concluded that the investigated Fe-SMA in this thesis has also the ability to work in applications having high stress levels as well as at multi-axial stresses.

The constant slope of the blue curve in Fig. 5.65 confirms that the load is applied displacement controlled.

There is a shift in stress response (gap on left side in Fig. 5.65) between solid thick curves and dotted thick curves which shows the mechanical behavior of the investigated Fe-SMA is not identical along the two axes (i.e. x- and y-axis), therefore, it shows the condition of asymmetry.

Moreover, the stress reaches zero by unloading but not the strain, it might be due to surface roughness and/or the opposite surfaces of sample are not parallel to each other.

Besides, there is a shift in stress response (gap on lower side in Fig. 5.65) between different stress curves. The surface of sample has some topography, and this topography is compressed during the test. Consequently, there is a shift in stress response on lower side of Fig. 5.65.

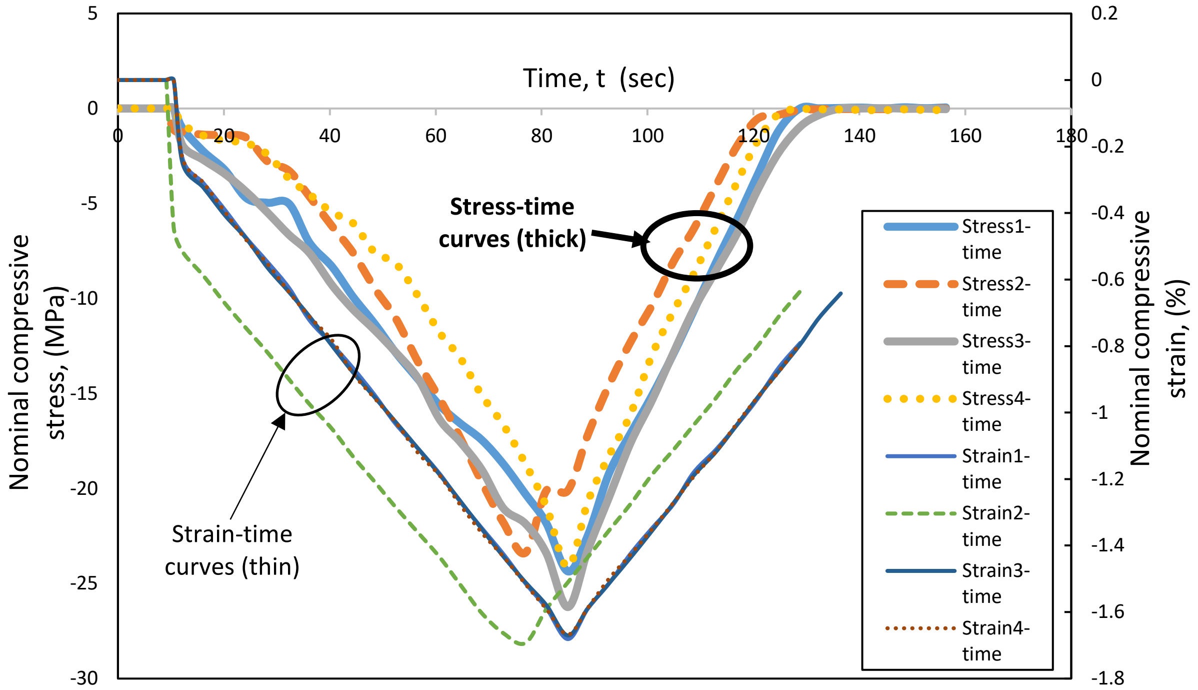

Fig. 5.65: Stress-strain-time behavior of different faces of the sample during loading and unloading of all faces under equibiaxial compression at room temperature

5.6 Hardness of the investigated Fe-SMA

The hardness test is possibly least expensive and simplest method for mechanically characterizing the material because it does not need a special geometry of the specimen as well as the testing equipment is inexpensive and quick. In this section, hardness of Fe-15Mn-10Cr-8Ni-4Si SMA is measured. Hardness is defined as the ability of a material to resist permanent indentation or deformation. In general, an indenter of known geometry and mechanical properties is pressed in the test material while measuring the hardness of material. As indenter is pressed in the material, therefore, hardness can also be viewed as the ability of material to resist compressive loads.

The indenter might be, (i) conical (Rockwell test HRB Rockwell B Hardness or HRC sometimes only RC showing Rockwell Hardness measured on C scale), (ii) pyramidal (Vickers test HV) or (iii) spherical (Brinell test BHN but now HBW. BHN have been used for many years, however, ASTM has changed the standard for Brinell test i.e. requiring the use of a carbide indention ball for all tests using a 3000 kg load and steel balls no longer allowed. ASTM has also changed the abbreviation for new standard from BHN to HBW). The hardness of Fe-15Mn-10Cr-8Ni-4Si SMA is found to be 85 HRB.

Chapter 6

Conclusions and Future Outlook

The present thesis deals with the current status of research and commercialization of Fe-SMAs. It has been clearly observed from an extensive literature study that there is almost small quantity of research available on such type of cheap and commercially available Fe-SMAs which have ability to be the counterpart of Nitinol. The thesis also dwells upon the future directions in which research should be targeted as well as the future prospects of converting the research into components for commercial use. This chapter summarizes the conclusions and future outlook drawn from this thesis.

6.1 Conclusions

Based upon the evaluation of a series of experiments (chapter 4) and their results (chapter 5), the following conclusions can be drawn for the investigated Fe-SMA produced by arc melting.

1. The transformation temperatures for the future FeMnSi-SMAs having different compositions can most probably be found out by means of keeping the DSC temperature range of -80°C to 400°C.
2. The martensite start temperature (M_s) and the martensite finish temperature (M_f) of FeMnSi-SMAs exist between the temperature range of -80°C to 135.85°C.
3. The austenite start temperature (A_s) and the austenite finish temperature (A_f) of FeMnSi-SMAs exist between the temperature range of 41°C to 400°C.
4. Most of the FeMnSi-SMAs have M_s above room temperature which is taken to be about 20°C to 25°C with an average of 23°C.
5. The investigated Fe-SMA has a potential for thermomechanical applications in terms of its thermal conductivity.
6. The thermal conductivity of investigated Fe-SMA increases by increasing the temperature over a range of 20°C to 400°C. Different values of thermal conductivity of the investigated Fe-SMA can be obtained from the curve in Fig. 5.23. It can be concluded that the range of thermal conductivity of the investigated Fe-SMA is in the range of a variety of conventional engineering alloys used in bearings and in the range of an alloy (60-Nitinol) used to make several tools. Table 5.18 shows thermal conductivities of numerous materials along with their applications in bearings, turbine blades, several pipe joints, rods, pipes, bolts, nuts, wires, studs, screws, allen keys, flange plates, seals, tools, and washers; these applications

also require the value of thermal conductivity in the range as that investigated for Fe-15Mn-10Cr-8Ni-4Si SMA.

7. The thermal diffusivity of the investigated Fe-SMA increases by increasing the temperature over a range of 20°C to 400°C. Different values of thermal diffusivity of the investigated Fe-SMA can be obtained from the curve in Fig. 5.20. In fact, the shape of the experimental curve in Fig. 5.20 shows that while heating from 25.8°C to 50.4°C, the thermal diffusivity of investigated Fe-SMA increases with a curve tending to be straight having less slope, afterward, the slope of the curve increases until it reaches the maximum temperature. The sensitivity of SMA seems to be an intrinsic disadvantage. Fig. 5.20 also shows that the investigated Fe-SMA is not very sensitive to temperature between M-A transformation range, also, there is no sudden decrease and increase of thermal diffusivity during M-A transformation contrary to that of Nitinol (Fig. 5.21).
8. Table 5.1 shows the important findings through DSC in the range of 20°C to 400°C with a heating rate of 10K/min. It has also been concluded from subsection 5.1.3 where the sample alloy has been analyzed with prior dipping into liquid nitrogen to make it fully martensite; (i) thermally induced phase transition of Fe-SMA occurs only once at 60.6°C and this transition does not repeat itself like the case with no prior nitrogen dip, (ii) only one endothermic peak is left showing $\varepsilon \rightarrow \gamma$ thermally induced phase transformation, and (iii) the second endothermic peak is vanished which was showing $\acute{\alpha} \rightarrow \gamma$ thermally induced phase transformation. In fact, the disadvantageous ά-martensite phase is vanished.
9. The value of austenite start temperature (A_s) of the investigated Fe-SMA is higher than that of human body which does not make it suitable to be used inside the human body. It can be made suitable for human body probably by annealing.
10. The density of investigated Fe-SMA decreases by increasing the temperature over a range of 20°C to 400°C. Different values of density of the investigated Fe-SMA can be obtained from the curve in Fig. 5.14.
11. The dilatation of investigated Fe-SMA increases by increasing the temperature over a range of 20°C to 400°C. Different values of dilatation for the investigated Fe-SMA can be obtained from the curve in Fig. 5.15.
12. The thermal expansion coefficient (CTE) of investigated Fe-SMA increases by increasing the temperature over a range of 20°C to 400°C. Different values of the thermal expansion coefficient for the investigated Fe-SMA can be obtained from the curve in Fig. 5.19.
13. The findings of this thesis and their comparison in Table 5.2, Table 5.10, and Table 5.19 show that the investigated Fe-SMA has a potential to be the counterpart of Nitinol.
14. Table 5.22 to Table 5.25 show the important findings through uniaxial compression at room temperature as well as at elevated temperatures. The emergence of stress-induced hexagonal close-packed (HCP) ε-martensite is observed in microstructure of the investigated Fe-SMA after uniaxial compression deformation.
15. Fig. 5.38 shows that value of the required force for phase transformation decreases by increasing the temperature. Fig. 5.39 illustrates that the transformation mechanism is temperature dependent. It can be observed that the plateau concerning the transformation onset stress (austenite to martensite transformation onset, σ_{AM}) decreases by increasing the temperature. The average rate of decrease of transformation onset stress between 20°C to 400°C is ≈60 MPa/100°C. It has also been observed by Fig. 5.26, Fig. 5.29, Fig. 5.33, and Fig. 5.36 (by Table 5.22 to Table 5.25 too) that elastic strain, $\varepsilon_{e,\,zz}$ as well as axial plastic strain, $\varepsilon_{p,\,zz}$ for investigated Fe-SMA increase by increasing the temperature from room temperature to 200°C, however, there is almost no increase from 200°C to 400°C.
16. The modulus of elasticity, E_A decreases by increasing the temperature from 20°C to 400°C with an average decrease rate of 900MPa/100°C. The martensitic modulus of elasticity (E_M) is less than austenitic modulus of elasticity (E_A) i.e. $E_M < E_A$.

17. There is almost no increase in the yield stress, σ_y from room temperature to 200°C, however, it decreases from 200°C to 400°C with a decrease rate of 22.5 MPa/100°C.
18. The displacement-controlled loading and unloading of the sample under equibiaxial compression (2D) at room temperature is performed. It has been concluded that the investigated Fe-SMA has ability to work in the applications having high stress levels as well as at multi-axial stresses.
19. There is some residual strain, ε^r left inside the investigated Fe-SMA which expresses the plastic deformation and unavailability of superelasticity at 26 MPa which is probably high enough. In order to see the superelasticity the stress should have been lower and there should have been an idea of the value of yield strength for investigated Fe-SMA prior to perform the biaxial test.
20. The mechanical behavior of the investigated Fe-SMA is not identical along two axes (i.e. x- and y-axis) which means it shows the condition of asymmetry along said axes.

6.2 Future outlook

For further considerations on this subject, a series of possible works can be done in future in order to obtain further useful features of such a valuable Fe-SMA. The following ones are some suggestions as a future outlook,

1. Using experimental results to reproduce the experimental curves by means of numerical computations.
2. The investigations of martensite start temperatures (M_s) and martensite finish temperatures (M_f) for Fe-15Mn-10Cr-8Ni-4Si SMA using DSC (built in with nitrogen cooling) or by electric resistivity.
3. Different heat treatment techniques in order to bring the austenite start temperature (A_s) to human body temperature like that of Nitinol which is currently being used in human body.
4. Keeping in view the importance of Fe-SMAs, it is recommended that the experimentations used in this thesis should be extended to other types of Fe-SMAs.
5. Fatigue analysis of Fe-SMAs should be performed at different temperature levels.
6. The rest investigations on Fe-15Mn-10Cr-8Ni-4Si SMA in order to make sure its use in the applications proposed in this thesis.
7. An extensive experimental study is necessary for understanding and modeling the mechanisms in other Fe-SMAs under biaxial loading or other complex loadings. Consequently, there will be a considerable development in the field of Fe-SMAs in order to explore their mechanical behavior and applications under complex loadings.

The author hopes that promptly growing development and research on Fe-SMAs will lead towards excellence and their application in many other fields in the coming near future.

Bibliography

[1] C. Czaderski, M. Shahverdi, R. Brönnimann, C. Leinenbach, and M. Motavalli, "Feasibility of iron-based shape memory alloy strips for prestressed strengthening of concrete structures," *Constr. Build. Mater.*, vol. 56, pp. 94–105, 2014.

[2] W. Huang and W. Toh, "Training two-way shape memory alloy by reheat treatment," *J. Mater. Sci. Lett.*, vol. 19, no. 17, pp. 1549–1550, 2000.

[3] R. A. Rahman, D. Juhre, and T. Halle, "Review of Types, Properties, and Importance of Ferrous Based Shape Memory Alloys," *Korean J. Mater. Res.*, vol. 28, no. 7, pp. 381–390, 2018.

[4] T. Sawaguchi *et al.*, "Designing Fe-Mn-Si alloys with improved low-cycle fatigue lives," *Scr. Mater.*, vol. 99, pp. 49–52, 2015.

[5] C. Lexcellent and F. Thiebaud, "Determination of the phase transformation zone at a crack tip in a shape memory alloy exhibiting asymmetry between tension and compression," *Scr. Mater.*, vol. 59, no. 3, pp. 321–323, 2008.

[6] I. Nikulin, T. Sawaguchi, A. Kushibe, Y. Inoue, H. Otsuka, and K. Tsuzaki, "Effect of strain amplitude on the low-cycle fatigue behavior of a new Fe–15Mn–10Cr–8Ni–4Si seismic damping alloy," *Int. J. Fatigue*, vol. 88, pp. 132–141, 2016.

[7] T. Sawaguchi, T. Maruyama, H. Otsuka, A. Kushibe, Y. Inoue, and K. Tsuzaki, "Design Concept and Applications of Fe–Mn–Si-Based Alloys—from Shape-Memory to Seismic Response Control," *Mater. Trans.*, vol. 57, no. 3, pp. 283–293, 2016.

[8] H. Otsuka, H. Yamada, T. Maruyama, H. Tanahashi, S. Matsuda, and M. Murakami, "Effects of alloying additions on Fe-Mn-Si shape memory alloys," *ISIJ Int.*, vol. 30, no. 8, pp. 674–679, 1990.

[9] I. Nikulin, T. Sawaguchi, K. Ogawa, and K. Tsuzaki, "Effect of γ to ε martensitic transformation on low-cycle fatigue behaviour and fatigue microstructure of Fe-15Mn-10Cr-8Ni-xSi austenitic alloys," *Acta Mater.*, vol. 105, pp. 207–218, 2016.

[10] A. Cladera, B. Weber, C. Leinenbach, C. Czaderski, M. Shahverdi, and M. Motavalli, "Iron-based shape memory alloys for civil engineering structures: An overview," *Constr. Build. Mater.*, vol. 63, pp. 281–293, 2014.

[11] L. Kang, D. Zhizhong, L. Yongchang, and Z. Lin, "A newly developed Fe-based shape memory alloy suitable for smart civil engineering," *Smart Mater. Struct.*, vol. 22, no. 4, p. 45002, 2013.

[12] a. Cladera, B. Weber, C. Leinenbach, C. Czaderski, M. Shahverdi, and M. Motavalli, “Iron-based shape memory alloys for civil engineering structures: An overview,” *Constr. Build. Mater.*, vol. 63, pp. 281–293, 2014.

[13] L. Kang, D. Zhizhong, L. Yongchang, and Z. Lin, “A newly developed Fe-based shape memory alloy suitable for smart civil engineering,” *Smart Mater. Struct.*, vol. 22, pp. 1–6, 2013.

[14] C. A. Della Rovere, J. H. Alano, J. Otubo, and S. E. Kuri, “Corrosion behavior of shape memory stainless steel in acid media,” *J. Alloys Compd.*, vol. 509, no. 17, pp. 5376–5380, 2011.

[15] C. A. Della Rovere, J. H. Alano, R. Silva, P. A. P. Nascente, J. Otubo, and S. E. Kuri, “Characterization of passive films on shape memory stainless steels,” *Corros. Sci.*, vol. 57, pp. 154–161, 2012.

[16] C. A. Della Rovere, J. H. Alano, R. Silva, P. A. P. Nascente, J. Otubo, and S. E. Kuri, “Influence of alloying elements on the corrosion properties of shape memory stainless steels,” *Mater. Chem. Phys.*, vol. 133, no. 2–3, pp. 668–673, 2012.

[17] R. A. Rahman, D. Juhre, and T. Halle, “Review of Applications of Ferrous Based Shape Memory Smart Materials in Engineering and in Biomedical Sciences,” *Pakistan J. Eng. Appl. Sci.*, vol. 24, pp. 32–49, 2019.

[18] R. D. James and M. Wuttig, “Magnetostriction of martensite,” *Philos. Mag. A Phys. Condens. Matter, Struct. Defects Mech. Prop.*, vol. 77, no. 5, pp. 1273–1299, 1998.

[19] R. Hayashi, S. J. Murray, M. Marioni, S. M. Allen, and R. C. O’Handley, “Magnetic and Mechanical Properties of FeNiCoTi Magnetic Shape Memory Alloys,” *Sensors and actuators*, vol. 81, pp. 219–223, 2000.

[20] K. Ishida, R. Kainuma, I. Ohnuma, T. Omori, and K. Ando, “FE-BASED SHAPE MEMORY ALLOY AND ITS PRODUCTION METHOD,” *United states Pat.*, vol. 2, no. 12, pp. 1–14, 2014.

[21] P. Huang, H. Peng, S. Wang, T. Zhou, and Y. Wen, “Relationship between martensitic reversibility and different nano-phases in a FeMnAlNi shape memory alloy,” *Mater. Charact.*, vol. 118, pp. 22–28, 2016.

[22] M. Vollmer *et al.*, “On the effect of gamma phase formation on the pseudoelastic performance of polycrystalline Fe-Mn-Al-Ni shape memory alloys,” *Scr. Mater.*, vol. 108, pp. 23–26, 2015.

[23] T. Duerig, a Pelton, and D. Stöckel, “An overview of nitinol medical applications,” *Mater. Sci. Eng. A*, vol. 273–275, pp. 149–160, 1999.

[24] W. Yan, C. H. Wang, X. P. Zhang, and Y. W. Mai, “Theoretical modelling of the effect of plasticity on reverse transformation in superelastic shape memory alloys,” *Mater. Sci. Eng. A*, vol. 354, no. 1–2, pp. 146–157, 2003.

[25] S. Daly, a. Miller, G. Ravichandran, and K. Bhattacharya, “An experimental investigation of crack initiation in thin sheets of nitinol,” *Acta Mater.*, vol. 55, no. 18, pp. 6322–6330, 2007.

[26] M. Shahverdi, J. Michels, C. Czaderski, and M. Motavalli, “Iron-based shape memory

alloy strips, part 1: characterization and material behavior," *Fourth Conf. Smart Monit. Assess. Rehabil. Civ. Struct. SMART 2017*, 2017.

[27] M. Shahverdi, C. Czaderski, and M. Motavalli, "Iron-based shape memory alloys for prestressed near-surface mounted strengthening of reinforced concrete beams," *Constr. Build. Mater.*, vol. 112, pp. 28–38, 2016.

[28] T. Sawaguchi *et al.*, "Development of prestressed concrete using Fe-Mn-Si-based shape memory alloys containing NbC," *Mater. Trans.*, vol. 47, no. 3, pp. 580–583, 2006.

[29] M. Shahverdi, C. Czaderski, P. Annen, and M. Motavalli, "Strengthening of RC beams by iron-based shape memory alloy bars embedded in a shotcrete layer," *Eng. Struct.*, vol. 117, pp. 263–273, 2016.

[30] I. M. P. Doyle, G. Dale, H. Choi, and B. City, "(12) United States Patent," vol. 2, no. 12, pp. 2–11, 2012.

[31] H. W. Song and S. M. Lu, "Repair of a deep-mine permanent access tunnel using bolt, mesh and shotcrete," *Tunn. Undergr. Sp. Technol.*, vol. 16, no. 3, pp. 235–240, 2001.

[32] A. D. G. Tsonos, "Performance enhancement of R/C building columns and beam-column joints through shotcrete jacketing," *Eng. Struct.*, vol. 32, no. 3, pp. 726–740, 2010.

[33] P. E. A. Reese, S. A. Kulchin, and F. City, "4,952,097," 1990.

[34] P. P. Data, "US Patent," 2005.

[35] A. Terzić, L. Andrić, and V. Mitić, "Mechanically activated coal ash as refractory bauxite shotcrete microfiller: Thermal interactions mechanism investigation," *Ceram. Int.*, vol. 40, no. 8 PART A, pp. 12055–12065, 2014.

[36] C. C. Li, "Rock support design based on the concept of pressure arch," *Int. J. Rock Mech. Min. Sci.*, vol. 43, no. 7, pp. 1083–1090, 2006.

[37] F. Hedayati Dezfuli and M. S. Alam, "Shape memory alloy wire-based smart natural rubber bearing," *Smart Mater. Struct.*, vol. 22, no. 4, p. 45013 (17pp), 2013.

[38] F. Hedayati Dezfuli and M. S. Alam, "Performance-based assessment and design of FRP-based high damping rubber bearing incorporated with shape memory alloy wires," *Eng. Struct.*, vol. 61, pp. 166–183, 2014.

[39] F. H. Dezfuli and M. S. Alam, "Seismic vulnerability assessment of a steel- girder highway bridge equipped with different SMA wire-based smart elastomeric isolators."

[40] S. Tiedao, S. Tiedao, and S. Tiedao, "Application Research on Fe-based SMA in the Anti-breaking of Screw Connection," pp. 1–5, 2015.

[41] O. Benafan, R. D. Noebe, and T. J. Halsmer, "Shape Memory Alloy Rock Splitters (SMARS)-A Non-Explosive Method for Fracturing Planetary Rocklike Materials and Minerals," no. July, 2015.

[42] A. V. Druker, A. Perotti, I. Esquivel, and J. Malarría, "A manufacturing process for shaft and pipe couplings of Fe-Mn-Si-Ni-Cr shape memory alloys," *Mater. Des.*, vol. 56, pp. 878–888, 2014.

[43] A. V. Druker, A. Perotti, I. Esquivel, and J. Malarría, “Design of Devices and Manufacturing of Fe-Mn-Si Shape Memory Alloy Couplings,” *Procedia Mater. Sci.*, vol. 8, pp. 878–885, 2015.

[44] A. V. Druker, I. Esquivel, A. Perotti, and J. Malarria, “Optimization of Fe-15Mn-5Si-9Cr-5Ni shape memory alloy for pipe and shaft couplings,” *J. Mater. Eng. Perform.*, vol. 23, no. 7, pp. 2732–2737, 2014.

[45] J. Liu, H. X. Zheng, M. X. Xia, Y. L. Huang, and J. G. Li, “Martensitic transformation and magnetic properties in Heusler CoNiGa magnetic shape memory alloys,” *Scr. Mater.*, vol. 52, no. 9, pp. 935–938, 2005.

[46] H. E. Karaca, I. Karaman, Y. I. Chumlyakov, D. C. Lagoudas, and X. Zhang, “Compressive response of a single crystalline CoNiAl shape memory alloy,” *Scr. Mater.*, vol. 51, no. 3, pp. 261–266, 2004.

[47] A. Francis, Y. Yang, S. Virtanen, and A. R. Boccaccini, “Iron and iron-based alloys for temporary cardiovascular applications,” *J. Mater. Sci. Mater. Med.*, vol. 26, no. 3, p. 138, 2015.

[48] M. Moravej and D. Mantovani, “Biodegradable metals for cardiovascular stent application: Interests and new opportunities,” *Int. J. Mol. Sci.*, vol. 12, no. 7, pp. 4250–4270, 2011.

[49] U. Allenstein, Y. Ma, A. Arabi-Hashemi, M. Zink, and S. G. Mayr, “Fe-Pd based ferromagnetic shape memory actuators for medical applications: Biocompatibility, effect of surface roughness and protein coatings,” *Acta Biomater.*, vol. 9, no. 3, pp. 5845–5853, 2013.

[50] Y. Chang, Wenn-Shao; Araki, “Use of shape-memory alloys in construction: a critical review,” *Proc. Inst. Civ. Eng. - Civ. Eng.*, vol. 169, no. 2, pp. 87–95, 2016.

[51] R. A. Shakoor and F. Ahmad Khalid, “Thermomechanical behavior of Fe-Mn-Si-Cr-Ni shape memory alloys modified with samarium,” *Mater. Sci. Eng. A*, vol. 499, no. 1–2, pp. 411–414, 2009.

[52] B. C. Maji, C. M. Das, M. Krishnan, and R. K. Ray, “The corrosion behaviour of Fe-15Mn-7Si-9Cr-5Ni shape memory alloy,” *Corros. Sci.*, vol. 48, no. 4, pp. 937–949, 2006.

[53] S. Farjami, K. Hiraga, and H. Kubo, “Crystallography and elastic energy analysis of VN precipitates in Fe-Mn-Si-Cr shape memory alloys,” *Acta Mater.*, vol. 53, no. 2, pp. 419–431, 2005.

[54] H. C. Lin, K. M. Lin, Y. S. Chen, and C. H. Yang, “Ion nitriding of Fe-30Mn-6Si-5Cr shape memory alloyII. Erosion characteristics,” *Surf. Coatings Technol.*, vol. 194, no. 1, pp. 74–81, 2005.

[55] H. Kubo, H. Otsuka, S. Farjami, and T. Maruyama, “Characteristics of Fe-Mn-Si-Cr shape memory alloys in centrifugal casting,” *Scr. Mater.*, vol. 55, no. 11, pp. 1059–1062, 2006.

[56] M. Mishra and A. Anish Ravindra, “A comparison of conventional and iron- based shape memory alloys and their potential in structural applications,” *Int. J. Struct. Civ. Engg. Res.*, vol. 3, no. 4, 2014.

[57] W. Huang, "On the selection of shape memory alloys for actuators," *Mater. Des.*, vol. 23, no. 1, pp. 11–19, 2002.

[58] C. Liang and C. A. Rogers, "Design of Shape Memory Alloy Springs with Applications in Vibration Control," *J. Intell. Mater. Syst. Struct.*, vol. 8, no. 4, pp. 314–322, 1997.

[59] E. Faran and D. Shilo, "Ferromagnetic Shape Memory Alloys-Challenges, Applications, and Experimental Characterization," *Exp. Tech.*, vol. 40, no. 3, pp. 1005–1031, 2016.

[60] K. Ullakko, "Magnetically controlled shape memory alloys: A new class of actuator materials," *J. Mater. Eng. Perform.*, vol. 5, no. 3, pp. 405–409, 1996.

[61] H. E. Karaca, A. S. Turabi, Y. I. Chumlyakov, I. Kireeva, H. Tobe, and B. Basaran, "Superelasticity of [001]-oriented Fe42.6-Ni27.9-Co17.2-Al9.9-Nb2.4 ferrous shape memory alloys," *Scr. Mater.*, vol. 120, pp. 54–57, 2016.

[62] M. Rohde and A. Schussler, "On the response-time behaviour of laser micromachined NiTi shape memory actuators," *Sensors Actuators, A Phys.*, vol. 61, pp. 463–468, 1997.

[63] W. Huang, "On the selection of shape memory alloys for actuators," *Mater. Des.*, vol. 23, no. 1, pp. 11–19, 2002.

[64] N. Stanford and D. P. Dunne, "Martensite/particle interactions and the shape memory effect in an Fe-Mn-Si-based alloy," *J. Mater. Sci.*, vol. 42, no. 12, pp. 4334–4343, 2007.

[65] N. Stanford and D. P. Dunne, "Effect of Si on the reversibility of stress-induced martensite in Fe–Mn–Si shape memory alloys," *Acta Mater.*, vol. 58, no. 20, pp. 6752–6762, 2010.

[66] H.-C. Lin, S.-K. Wu, Y.-T. Peng, T.-C. Cheng, and K.-M. Lin, "Pseudoelasticity of thermo-mechanically treated Fe–Mn–Si–Cr–Ta alloys," *J. Alloys Compd.*, vol. 577S, pp. S338–S343, 2013.

[67] C. Gurau, G. Gurau, L. G. Bujoreanu, and F. M. B. Fernandes, "A Comparative Study of Austenitic Structure in NiTi and Fe Based Shape Memory Alloys after Severe Plastic Deformation," *Mater. Today Proc.*, vol. 2, pp. S905–S908, 2015.

[68] B. C. Maji and M. Krishnan, "The effect of microstructure on the shape recovery of a Fe–Mn–Si–Cr–Ni stainless steel shape memory alloy," *Scr. Mater.*, vol. 48, no. 1, pp. 71–77, 2003.

[69] K. Tsuzaki, K. Fukuda, M. Koyama, and H. Matsunaga, "Hexagonal close-packed Martensite-related Fatigue Crack Growth under the Influence of Hydrogen: Example of Fe-15Mn-10Cr-8Ni-4Si Austenitic Alloy," *Scr. Mater.*, vol. 113, pp. 6–9, 2016.

[70] I. Nikulin, T. Sawaguchi, K. Ogawa, and K. Tsuzaki, "Effect of γ to ε martensitic transformation on low-cycle fatigue behaviour and fatigue microstructure of Fe-15Mn-10Cr-8Ni-xSi austenitic alloys," *Acta Mater.*, vol. 105, pp. 207–218, 2016.

[71] N. Van Caenegem, L. Duprez, K. Verbeken, D. Segers, and Y. Houbaert, "Stresses related to the shape memory effect in Fe-Mn-Si-based shape memory alloys," *Mater. Sci. Eng. A*, vol. 481–482, no. 1-2 C, pp. 183–189, 2008.

[72] M. Koyama, M. Murakami, K. Ogawa, T. Kikuchi, and S. Sawaguchi, "Shape memory characteristics of Fe-30Mn-5Si-1Al and Fe28Mn-5Si-1 AI-5Cr alloys," *SMST-2007* -

Proc. Int. Conf. Shape Mem. Superelastic Technol., no. July 2016, pp. 653–658, 2008.

[73] W. Khalil, A. Mikolajczak, C. Bouby, and T. Ben Zineb, “A constitutive model for Fe-based shape memory alloy considering martensitic transformation and plastic sliding coupling: Application to a finite element structural analysis,” *J. Intell. Mater. Syst. Struct.*, vol. 23, no. 10, pp. 1143–1160, 2012.

[74] A. Dogan and H. Arslan, “Effect of ball-milling conditions on microstructure during production of Fe-20Mn-6Si-9Cr shape memory alloy powders by mechanical alloying,” *J. Therm. Anal. Calorim.*, vol. 109, no. 2, pp. 933–938, 2012.

[75] B. C. Maji, M. Krishnan, M. Sujata, Gouthama, and R. K. Ray, “Effect of Co Addition on the Microstructure, Martensitic Transformation and Shape Memory Behavior of Fe-Mn-Si Alloys,” *Metall. Mater. Trans. A*, vol. 44, no. 1, pp. 172–185, 2013.

[76] M. S. Andrade, R. M. Osthues, and G. J. Arruda, “The influence of thermal cycling on the transition temperatures of a Fe-Mn-Si shape memory alloy,” *Mater. Sci. Eng. A*, vol. 273–275, pp. 512–516, Dec. 1999.

[77] H. C. Lin, S. K. Wu, Y. T. Peng, T. C. Cheng, and K. M. Lin, “Pseudoelasticity of thermo-mechanically treated Fe-Mn-Si-Cr-Ta alloys,” *J. Alloys Compd.*, vol. 577, no. SUPPL. 1, pp. S338–S343, 2013.

[78] B. C. Maji, M. Krishnan, Gouthama, and R. K. Ray, “Role of Si in improving the shape recovery of FeMnSiCrNi shape memory alloys,” *Metall. Mater. Trans. A*, vol. 42, no. 8, pp. 2153–2165, 2011.

[79] R. A. Rahman, D. Juhre, T. Halle, S. Mehmood, and W. Asghar, “Types , DSC Thermal Characterization of Fe-Mn-Si based Shape Memory Smart Materials and their Feasibility for Human Body in Terms of Austenitic Start Temperatures,” *J. Eng. Technol.*, vol. 8, no. 1, pp. 185–206, 2019.

[80] T. R. Meling and J. Ødegaard, “The effect of short-term temperature changes on superelastic nickel-titanium archwires activated in orthodontic bending,” *Am. J. Orthod. Dentofac. Orthop.*, vol. 119, no. 3, pp. 263–273, 2001.

[81] T. G. Bradley, W. A. Brantley, and B. M. Culbertson, “Differential scanning calorimetry (DSC) analyses of superelastic and nonsuperelastic nickel-titanium orthodontic wires,” *Am. J. Orthod. Dentofac. Orthop.*, vol. 109, no. 6, pp. 589–597, 1996.

[82] A. R. Pelton, G. H. Huang, P. Moine, and R. Sinclair, “Effects of thermal cycling on microstructure and properties in Nitinol,” *Mater. Sci. Eng. A*, vol. 532, pp. 130–138, 2012.

[83] H. Tobushi, Y. Shimeno, T. Hachisuka, and K. Tanaka, “Influence of strain rate on superelastic properties of TiNi shape memory alloy,” *Mech. Mater.*, vol. 30, no. 2, pp. 141–150, 1998.

[84] B. C. Maji, M. Krishnan, A. Verma, R. Basu, I. Samajdar, and R. K. Ray, “Effect of Pre-straining on the Shape Recovery of Fe-Mn-Si-Cr-Ni Shape Memory Alloys,” *Metall. Mater. Trans. A Phys. Metall. Mater. Sci.*, vol. 46, no. 2, pp. 639–655, 2014.

[85] Y. Guo, A. Klink, C. Fu, and J. Snyder, “Machinability and surface integrity of Nitinol shape memory alloy,” *CIRP Ann. - Manuf. Technol.*, vol. 62, no. 1, pp. 83–86, 2013.

[86] O. Grässel, L. Krüger, G. Frommeyer, and L. W. Meyer, “High strength Fe–Mn–(Al, Si) TRIP/TWIP steels development-properties-application,” *Int. J. Plast.*, vol. 16, no. 10, pp. 1391–1409, 2000.

[87] A. Sato, E. Chishima, K. Soma, and T. Mori, “Shape memory effect in γ⇄ϵ transformation in Fe-30Mn-1Si alloy single crystals,” *Acta Metall.*, vol. 30, no. 6, pp. 1177–1183, Jun. 1982.

[88] A. Sato, Y. Yamaji, and T. Mori, “Physical properties controlling shape memory effect in Fe-Mn-Si alloys,” *Acta Metall.*, vol. 34, no. 2, pp. 287–294, Feb. 1986.

[89] C. Rogueda, C. Lexcellent, and L. Bocher, “Experimental study of pseudoelastic behaviour of a CuZnAl polycrystalline shape memory alloy under tension-torsion proportional and non-proportional loading tests,” *Arch. Mech.*, vol. 48, pp. 1025–1045, 1996.

[90] B. Raniecki, S. Miyazaki, K. Tanaka, L. Dietrich, and C. Lexcellent, “Deformation behaviour of TiNi shape memory alloy undergoing R-phase reorientation in torsion-tension (compression) tests,” *Arch. Mech.*, vol. 51, no. 6, pp. 745–784, 1999.

[91] O. Bouaziz, S. Allain, C. P. Scott, P. Cugy, and D. Barbier, “High manganese austenitic twinning induced plasticity steels: A review of the microstructure properties relationships,” *Curr. Opin. Solid State Mater. Sci.*, vol. 15, no. 4, pp. 141–168, 2011.

[92] A. Cladera, B. Weber, C. Leinenbach, C. Czaderski, M. Shahverdi, and M. Motavalli, “Iron-based shape memory alloys for civil engineering structures: An overview,” *Constr. Build. Mater.*, vol. 63, pp. 281–293, 2014.

[93] T. Sawaguchi *et al.*, “Vibration mitigation by the reversible fcc/hcp martensitic transformation during cyclic tension-compression loading of an Fe-Mn-Si-based shape memory alloy,” *Scr. Mater.*, vol. 54, no. 11, pp. 1885–1890, 2006.

[94] T. Sawaguchi, L. G. Bujoreanu, T. Kikuchi, K. Ogawa, M. Koyama, and M. Murakami, “Mechanism of reversible transformation-induced plasticity of Fe-Mn-Si shape memory alloys,” *Scr. Mater.*, vol. 59, no. 8, pp. 826–829, 2008.

[95] S. Dadbakhsh, M. Speirs, J. P. Kruth, J. Schrooten, J. Luyten, and J. Van Humbeeck, “Effect of SLM parameters on transformation temperatures of shape memory nickel titanium parts,” *Adv. Eng. Mater.*, vol. 16, no. 9, pp. 1140–1146, 2014.

[96] E. Patoor, M. El Amrani, A. Eberhardt, and M. Berveiller, “Determination of the Origin for the Dissymmetry Observed between Tensile and Compression Tests on Shape Memory Alloys,” *Le J. Phys. IV*, vol. 05, no. C2, pp. C2-495-C2-500, 2007.

[97] E. Patoor, A. Eberhardt, and M. Berveiller, “Micromechanical Modelling of Superelasticity in Shape Memory Alloys,” *Le J. Phys. IV*, vol. 06, no. C1, pp. C1-277-C1-292, 2007.

[98] F. Marketz and F. D. Fischer, “Modelling the mechanical behavior of shape memory alloys under variant coalescence,” *Comput. Mater. Sci.*, vol. 5, no. 1–3, pp. 210–226, 2002.

[99] L. Orgéas and D. Favier, “Non-Symmetric Tension-Compression Behaviour of NiTi Alloy,” *J. Phys. IV*, vol. 05, no. C8, pp. C8-605-C8-610, 2014.

[100] L. Bocher, D. Jeune, P. Robinet, and P. Delobelle, “On the Utility of Complex Multiaxial Cyclic Loadings in Tension-Torsion-Internal and External Pressures to Improve the Formulation of the Constitutive Equations,” *Low Cycle Fatigue Elasto-Plastic Behav. Mater.*, pp. 223–228, 1998.

[101] J. G. M. van Mier, “Multiaxial behavior of concrete-test methods and results,” *Insa Toulouse*, vol. 1, pp. 75–85, 1984.

[102] J. Weiss and E. M. Schulson, “The failure of fresh-water granular ice under multiaxial compressive loading,” *Acta Metall. Mater.*, vol. 43, no. 6, pp. 2303–2315, 1995.

[103] C. Bouvet, S. Calloch, and C. Lexcellent, “Mechanical Behavior of a Cu-Al-Be Shape Memory Alloy Under Multiaxial Proportional and Nonproportional Loadings,” *J. Eng. Mater. Technol.*, vol. 124, no. 2, p. 112, 2002.

[104] C. Bouvet, S. Calloch, and C. Lexcellent, “Mechanical Behavior of a Cu-Al-Be Shape Memory Alloy Under Multiaxial Proportional and Nonproportional Loadings,” *J. Eng. Mater. Technol.*, vol. 124, no. 2, p. 112, 2002.

[105] C. Zanotti, P. Giuliani, G. Riva, A. Tuissi, and A. Chrysanthou, “Thermal diffusivity of Ni-Ti SMAs,” *J. Alloys Compd.*, vol. 473, no. 1–2, pp. 231–237, 2009.

[106] M. Khairul Alam and M. S. Anghelescu, “Analysis of deformation and residual stresses in composites processed on a carbon foam tooling,” *J. Compos. Mater.*, vol. 43, no. 19, pp. 2057–2070, 2009.

[107] R. A. Rahman, D. Juhre, and T. Halle, “Comparison of Biaxial Loading of Ferrous Based (Fe-based) Shape Memory Smart Materials with Linear and Non-linear Materials,” *Curr. Smart Mater.*, vol. 3, no. 2, pp. 1–9, 2018.

[108] M. K. Stanford, “Thermophysical Properties of 60-NITINOL for Mechanical Component Applications:NASA,” no. December 2012, pp. 1–6, 2012.

[109] B. Zillmann *et al.*, “In-plane biaxial compression and tension testing of thin sheet materials,” *Int. J. Solids Struct.*, vol. 66, pp. 111–120, 2014.

[110] R. Pfeifer, D. Herzog, M. Hustedt, and S. Barcikowski, “Pulsed Nd:YAG laser cutting of NiTi shape memory alloys - Influence of process parameters,” *J. Mater. Process. Technol.*, vol. 210, no. 14, pp. 1918–1925, 2010.

[111] E. A. Giroux, M. Maglione, A. Gueldry, and J. L. Mantoux, “Electromagnetic heating of a shape memory alloy translator,” *J. Phys. D. Appl. Phys.*, vol. 29, no. 3, pp. 923–928, 1996.

[112] J.-H. Jun and C.-S. Choi, “Variation of stacking fault energy with austenite grain size and its effect on the MS temperature of γ→ε martensitic transformation in Fe–Mn alloy,” *Mater. Sci. Eng. A*, vol. 257, no. 2, pp. 353–356, Dec. 1998.

[113] S. Sadeghpour, A. Kermanpur, and A. Najafizadeh, “Investigation of the effect of grain size on the strain-induced martensitic transformation in a high-Mn stainless steel using nanoindentation,” *Mater. Sci. Eng. A*, vol. 612, pp. 214–216, Aug. 2014.

[114] N. Van Caenegem, L. Duprez, K. Verbeken, D. Segers, and Y. Houbaert, “Stresses related to the shape memory effect in Fe–Mn–Si-based shape memory alloys,” *Mater. Sci. Eng. A*, vol. 481, pp. 183–189, 2008.

[115] J. Otubo, F. C. Nascimento, P. R. Mei, L. P. Cardoso, and M. J. Kaufman, “Influence of Austenite Grain Size on Mechanical Properties of Stainless SMA,” *Mater. Sci.*, vol. 43, no. 5, pp. 916–919, 2002.

[116] R. A. Rahman, D. Juhre, and T. Halle, “EXPERIMENTAL CHARACTERIZATION OF PHASE TRANSFORMATION OF FE-15MN-10CR-8NI-4SI (WT. %) IRON-BASED SHAPE MEMORY FUNCTIONAL MATERIALS USING DILATOMETRY,” *Int. J. Adv. Mech. Civ. Eng.*, vol. 5, no. 6, pp. 10–13, 2018.

[117] D. S. Ford and S. R. White, “Thermomechanical behavior of 55Ni45Ti nitinol,” *Acta Mater.*, vol. 44, no. 6, pp. 2295–2307, 1996.

[118] J. D. Petty, J. N. Huckins, and A. David, “(12) Patent Application Publication (10) Pub . No .: US 2002/0187020 A1,” vol. 1, no. 19, 2002.

[119] B. Zillmann *et al.*, “In-plane biaxial compression and tension testing of thin sheet materials,” *Int. J. Solids Struct.*, vol. 66, pp. 111–120, 2015.

[120] Bjoern Kiefer, “A phenomenological constitutive model for magnetic shape memory alloys,” 2006.

[121] N. N. Sarawate, “CHARACTERIZATION AND MODELING OF THE FERROMAGNETIC SHAPE MEMORY ALLOY Ni-Mn-Ga FOR SENSING AND ACTUATION,” 2008.

[122] D. C. Lagoudas, *Shape Memory Alloys: Modeling and Engineering Applications*. 2008.

[123] X. Chen, Y. He, and Z. Moumni, “Twin boundary motion in NiMnGa single crystals under biaxial compression,” *Mater. Lett.*, vol. 90, pp. 72–75, 2013.

List of publications

There are following research articles during the PhD studies.

1. M. A. Nasir, Z. Khan, I. Farooqi, S. Nauman, S. Anas, S. Khalil, A. Pasha, M. Shah, H. Qaiser, and R. Ata "Transverse shear behavior of a nomex core for sandwich panels" Journal of mechanics of composite materials (Springer), IF 0.451, Vol. 50, No. 6 (2015) Page 733-738
2. Mehmood S, Sultan A, Anwar W, Butt Z, Javed K, and Rehman RA. “A symbiosis modeling approach of global supply chain of an SME using mixed integer programming (MIP) and system dynamics (SD)” Journal of quality and technology management, Vol. 14, No. 2 (2017) Page 1-19
3. Rana Atta ur Rahman, Daniel Juhre and Usama Khan, "Experimental characterization for initiation of crack during fatigue analysis of mineralized aluminium alloy under both thermal and mechanical loading on rotating & bending machine" Current smart materials, Vol. 3, No. 1 (2018), Page 68-72
4. RAHMAN Rana Atta ur, JUHRE Daniel, HALLE Thorsten, MEHMOOD Shahid, and ASGHAR Waqas, "Types, DSC Thermal Characterization of Fe-Mn-Si based Shape Memory Smart Materials and their Feasibility for Human Body in Terms of Austenitic Start Temperatures" Journal of engineering technology, IF 0.69, Vol. 8, No. 1 (Jan-2019) Page 185-206
5. Rana Atta Ur Rahman, Daniel Juhre, and Thorsten Halle, "Review of types, properties and importance of ferrous based shape memory alloys" Korean journal of materials research, IF 0.1, Vol. 28, No. 7 (2018) Page 381-388
6. S. Mehmood, N.A. Anjum, W. Anwar, R.A. Rahman, K. Javed, and S. Badshah, “A review of the effect of electric discharge machining on the surface integrity of metallic parts” The Nucleus, Vol. 55, No. 1 (2018) Page 38-46
7. Rahman RA "Fatigue Crack Initiation in AA3004 At Elevated Temperature Using Rotating and Bending Fatigue Testing Machine", Modern Approaches on Material Science, Vol. 1, No. 2 (2019) Page 39-42
8. R. A. Rahman, Daniel Juhre, and Thorsten Halle, "Review of applications of ferrous based shape memory smart materials in engineering and in biomedical sciences", Pakistan Journal of Engineering and Applied Sciences, Vol. 24 (Jan-2019) Page 32-49
9. R. A. Rahman, Daniel Juhre, and Thorsten Halle, "Experimental characterization of phase transformation of Fe-15Mn-10Cr-8Ni-4Si (wt. %) iron-based shape memory functional materials using dilatometry" International Journal of Advances in Mechanical and Civil Engineering (IJAMCE), IF 3.66, Vol. 5, No. 6 (Nov-2018) Page 10-13

10. Rana Atta ur Rahman, Daniel Juhre, and Thorsten Halle, "Comparison of biaxial loading of ferrous based (Fe- based) shape memory smart materials with linear and non-linear materials" Current smart materials, Vol. 3, No. 2 (2018) Page 90-98

Further achievements

The following are some other achievements during PhD in addition to the above-mentioned research publications.

1. Certificate of an oral presentation at International Conference on Biomedical Technology 2015, Hannover, Germany.
2. Certificate of a poster presentation at Meeting of European SIAM Chapters 2017, Prague, Czech Republic.
3. Certificate of an oral MPI shotgun presentation at PhD SummerNet 2017, Max Planck Institute, Magdeburg, Germany.
4. Certificate of an oral presentation at International Conference on Mining, Material, and Metallurgical Engineering (ICMMME) 2018, Madrid, Spain.
5. Oral presentation in one-day seminar at the Institute of Rubber Technology 2015, Hannover, Germany.
6. Participation certificate German language and learned about B1 level.
7. Membership certificate of Magdeburger Verein für Technische Mechanik e.V. (MATEM), IFME, OvGU, Magdeburg, Germany.
8. Membership certificate of Society of Industrial and Applied Mathematics (SIAM), United States.